Horizontal fracture-fault network characterization of pavement imagery of the Whitby Mudstone

Q.D. Boersma
Department of Earth Sciences, Utrecht University, The Netherlands

A Msc Thesis

First Supervisor: Prof. dr. M.R. Drury (Utrecht University)
Second Supervisor: dr. N.J. Hardebol (TU Delft)
Third Supervisor: dr. M.E. Houben (Utrecht University)

Universiteit Utrecht

TU Delft Delft University of Technology

Abstract

Natural fractures play an important role in the hydrocarbon production from tight reservoirs. The need for fracture network pathways by fraccing matters particularly for shale gas prospects, due to their nano to micro darcies matrix permeabilities. The study of natural fractures from outcrops helps to better understand network connectivity and possibility of reactivating pre-existing planes of weakness, induced by hydraulic stimulation. Microseismicity also show that natural fractures are reactivated during fraccing in tight gas reservoirs and influence the success of the stimulation. An accurate understanding of natural fracture networks can help in predicting the development of fracture networks. In this research we analyze an outcrop analogue, the Whitby Mustone Formation (WMF), in terms of its horizontal fracture network. The WMF is the time equivalent of the Posidonia Shale Formation (PSF), which on itself is the main shale gas prospect in the Dutch subsurface.

The fracture network of the WMF is characterized by a system of steep dipping joints with two dominant directions with N-S and E-W strike. The network was digitized from bird-view imagery of the pavement with a spatial extent of ~100 m at sub-cm resolution. The imagery is interpreted in terms of orientation and length distributions, intensity and fractal dimensions. Samples from the field were analyzed for rock strength and sample mineralogy.

The results indicate that the fracture networks differ per bed. Observed differences are for example; the geometry of the fracture network, its cumulative length distribution, the fracture intensity, the fracture length vs its orientation and the fractal dimension. All these parameters greatly influence fracture network connectivity, the probability that longer fractures exist within the pavement and whether the network is more prone to clustering or scattering. Apart from the differences, the networks display a fairly similar orthogonal arrangement with dominant large (> 5-10 m) N-S striking fractures and smaller E-W striking cross-joints (< 2-3 m). A nested network arrangement is indicated by some smaller-scale N-S fractures abutting against the E-W striking ones. Furthermore, abutment relations provide some constraints on relative time. Timing indications with respect to burial-exhumation are difficult to establish. Some joints are cemented and measurable from the high-resolution imagery. The vein measurements helped establishing a first order relation between the fracture aperture with respect to their length and confirm that longer fractures have a wider aperture.

The above stated parameters and results all prove to be very valuable information which can help predict the geometries of the different fracture networks present within the PSF. It is important to understand the possible mechanisms which can cause these differences in fracture network characteristics. Bulk lithological variations between beds are minor, beds are mainly consisting of clay minerals. Furthermore, some quartz and pyrite is present in all samples and TOC is present in variable amounts. However, the occurrence of concretions up to 0.5m in size and differences in layer thickness correlates makes notable variations in distinct network arrangement. Therefore it appears that the presence of these concretions and variations in layer thickness alters the overall strength of the rock, hence the fracture network geometry.

Table of contents

List of figures

List of Tables

1. Introduction

Conventional gas production in The Netherlands has reached its peak and production rates are now even declining. Currently the Groningen gas field is responsible for up to 63% of the Dutch gas production, however current projections suggest that this gas field will only be productive for the following 15 to 20 years (EBN. 2014). Therefore new prospects for gas production in The Netherlands are needed in order to stay self-sustaining (EBN. 2014). One alternative to the conventional gas fields in The Netherlands are the shale gas fields, which are: The Posidonia Shale formation (PSF) and the Namurian Epen Formation (Including the Geverink laaglandpakket) (Zijp 2012). The focus of this report will lie on the Posidonia Shale Formation. Shale formations have very low porosity, matrix permeability (smaller than 100 millidarcy) and tend to be very anisotropic, due to aligned clay particles. New drilling techniques and hydraulic fracturing made hydrocarbon production out of such unconventional reservoirs possible. However, only limited subsurface (five usable drill cores) data and no outcrop data of the PSF are present in The Netherlands (Zijp 2013). Still, well,- and mudlogs of old wells suggest that gas is present in the PSF. To acquire more data on the PSF, the Whitby Mudstone Formation (WMF) (Whitby, UK) is used. The WMF is the lateral equivalent of the PSF in Northen Europe (Ghadeer et al. 2012). Both formations are deposited during the Lower Jurassic (Toarcian), roughly under the same anoxic sedimentary conditions. Recent studies done on the WMF currently include; fracture mechanics (Msc thesis T. Ravenstein TUDelft 2014), microstructures (Houben et al. EAGE Abstract 2014), fracture intensity and total organic carbon analysis (Ten Veen et al. EAGE Abstract 2014). However more outcrop data can be acquired from the WMF.

The usage of outcropping analogue formations and their fracture network geometries, in order to infer subsurface reservoir behavior is already widely described in the literature (Oddling et al. 1999, Gale et al. 2007, Gale et al. 2014, Imber et al. 2014 & Aydin 2014). Natural fracture planes may act as zones of weakness for subsurface reservoirs (Gale et al. 2007, Gale et al 2014). Therefore planes may reopen when being exposed to hydraulic fracturing (Gale et al. 2014). However using outcropping mudstone formations as an analogue for shale gas prospects is a relative new topic. This report uses field imagery and computer models to acquire and digitalize the observed horizontal fracture network. The acquired data is then processed using statistical tools already discussed in the literature (Bonnet et al. 2001, Oddling et al. 1999, Bour et al. 2003, Vermilye and Sholtz 1995). Together with lab work, conceptual, - and computer models discussed in the literature (Bai & Pollard 2001, Bai et al. 2002) are used to infer possible mechanisms which could have created the observed fracture geometry. Matrix mineralogy and organic carbon content of each layer is researched in the lab, in order to infer the possible potential of the WMF. All the produced data can then be used to better understand the observed fracture networks in terms of fracture length, fracture aperture and fracture orientation relations. Considering all the assumptions made, the following research question can be formulated: Is it possible to use the acquired outcrop data from the WMF, in order to make predictions of the subsurface behavior of the PSF in terms of fracture mechanics and fracture network geometry, when being induced to hydraulic fracturing?

2.1. Geological setting of the Cleveland Basin

The Cleveland basin in Jurassic times was part of a system of shallow epeiric seas and small basins, which were linked to the north sea basin via the Sole Pit basin (half graben structure) (Powell 2010). The Cleveland basin was bound by the North Sea high to the NE, to the W by the Pennine High, to the S by the East Midlands shelf and to the north lay the Market Weighton High (MWH) (Powell 2010). The MWH was a relatively stable unfolded block over which subsidence and sedimentations rates were reduced (Powell 2010). The Mid North Sea High underwent tilting to SE during the middle Jurassic, probably due to doming associated with active volcanism in the Central North Sea Basin (Powell 2010 and references therein).

The Cleveland basin was affected by a number of extensional faults and probable strike slip fault complexes. Some of these faults were active during Early and Middle Jurassic sedimentation (Mempes et al. 1996, Powell 2010). The eastern margin of the basin is bounded by North trending structures such as the Peak Through fault and the Peak fault. To the south the basin is cut off by graben structures. The Peak Through was active in Early Jurassic times and therefore preserves a thicker sequence of Lower Jurassic rocks compared to the surrounding areas (Mempes et al. 1996, Powell et al. 2010). Due to gentle folding of the Cleveland basin, the upper part of the Lias group was partly eroded. Some of the major bounding faults are known to have been active during the Cimmerian orogeny (Middle to late Jurassic), especially the east west trending faults, which show extension during the Oxfordian (Late Jurassic) (Powell 2010 and references therein). Fission track analysis suggests that the middle Jurassic sediments were buried to a depth of about 2.0 to 3.0km (Powell 2010 and references therein), prior to inversion (N-S direction) during the latest Cretaceous and Neogene. Kemp, Merriman and Bouch 2010 used clay mineral assemblages (Illite/Smectite) to infer the maximum burial depth of the lower Jurassic Lias group in the Cleveland Basin. The results showed a maximum burial depth of 4.0km. Using porosity data from outcrops and well logs from the Chalk Group (late Cretaceous) (Mempes et al. 1996) calculated that at least 2.5km of late Cretaceous and Neogene exhumation occurred during the inversion phase. The inversion also resulted in the formation of east-west trending anticline observed in the field (Lockton anticline, Goathland syncline and Robin Hood's Bay Dome), which now results in the outcrop pattern of Jurassic rocks along the Yorkshire Coast (Powell 2010).

2.2. Lower Jurassic Rocks (Lias Group)

The Lias Group in the Cleveland Basin is divided into five formations, here described in ascending order. The Redcar Mudstone (283 m thick) forms the thickest part of the group and mainly consists of siliciclastic clay and silt sediments interbedded with carbonate rich shell beds, concretion beds and middle to fine grained siliciclastic beds. The Redcar mudstone formation is overlain by the Staithes sandstone formation (c. 30 m thick). This formation consists of grey, yellow weathering, fine to middle grained sandstones and siltstones. The Staithes sandstone formation is overlain by the Cleveland ironstone formation (c. 28m thick). This formation consists of grey mudstone and sandy mudstone interbedded with the Ironstone. The Ironstone formation is overlain by the Whitby mudstone formation, which forms the Upper Lias formation. The Whitby Mudstone (c. 105m thick) consists mainly of grey to dark grey mudstones and siltstones with abundant shelly fossils. Uplift and erosion prior to the deposition of the Dogger formation resulted in that the full succession is only preserved in the syndepositional Peak Through (Powell et al. 2010). The full succession consists of the Grey Shale Member (c. 13.5m thick), which is a silty mudstone with some concretions. The Grey Shale contains up to 3.5% organic carbon, averaging around 1.2% (Ghadeer et al. 2012). This member is overlain by the Mulgrave Shale Member (Jet Rock) (c. 8.0m to 31.0m thick) which

indicates a change to more anoxic conditions. This formation is comprised of bituminous, dark grey mudstones with abundant ammonites and thick bands of calcareous concretions (Ghadeer et al. 2012). Up to 5.0µm pyrite framboids are revealed by microstructural analysis (Ghadeer et al. 2012). Total organic carbon content (up to 16%) in this formation is relatively high (Ghadeer et al. 2012 and references therein). The Alum Shale Member (c. 37m thick), overlies the Mulgrave Shale Member. This formation is generally less fossil rich and is comprised of grey silty mudstones with concretion bands. The Dogger formation forms the lower part of the Middle Jurassic Succession and rest unconformably on top of the Alum Shale Member, the Dogger Fm is mainly comprised out of sandstone (Powell 2010).

2.3. Pavement Geology

The pavements present in the area of interest are resembling different units present within the WMF. These are in stratigraphic order (old to young); the Grey Shale member, the Concretion unit, Bed 32 and the Cannonball unit (see Figure 1). The pavements are only cropping out at low tide. Figure 1 shows an orthophoto of the area of interest. This photo is used to create a first order geological map of the outcropping pavements. Due to the slight dip of the bedding, different layers crop out in the area of interest, which are all analysed in terms of its fracture network. In this part of the report the different units are described in terms of its appearance.

The top of the Grey Shale member is basically a grey mudstone containing no concretions and only a few ammonite fossils. The thickness of this layer is not known since it is the top of the Grey Shale member. As the name would suggest the Concretion Unit is a grey mudstone containing fossils and concretions which can have diameters up to 30.0cm long. The unit itself is approximately 0.5m thick. On top of the concretion unit lies Bed 32, which is a dark grey mudstone containing some fossils but no concretions. The layer is approximately 1.5m thick. The cannonball unit is the last unit which crops out in the Port Mulgrave area and is a grey mudstone layer containing up to 0.5 meter concretions. Some ammonite fossils are also observed. The layer is approximately 0.75 meter thick.

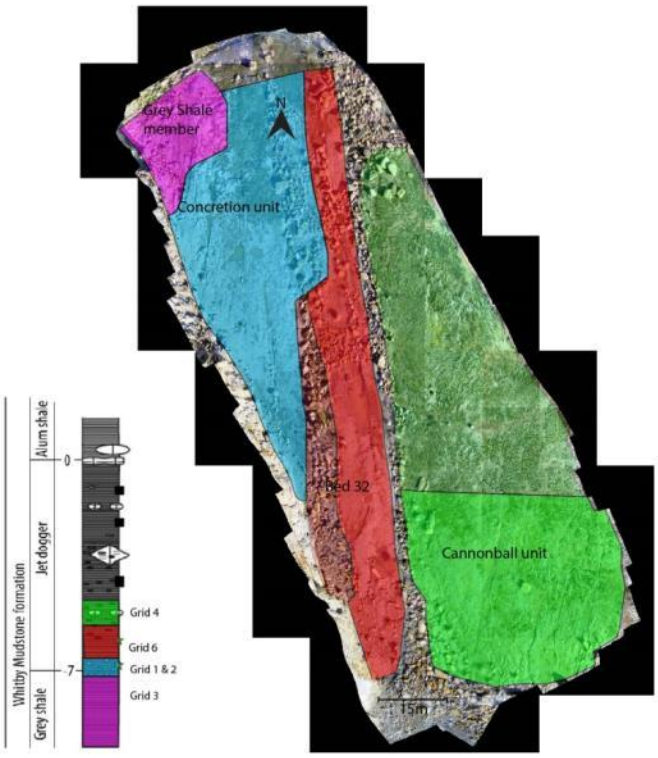

Figure 1 : This figure shows a geological map of the area of interest (Port Mulgrave). Due to the slightly dipping bedding of the WMF, different units crop out at low tide. The slightly more transparent colours indicate areas were rock determination was impossible and are therefore interpreted from the outcrop photo itself.

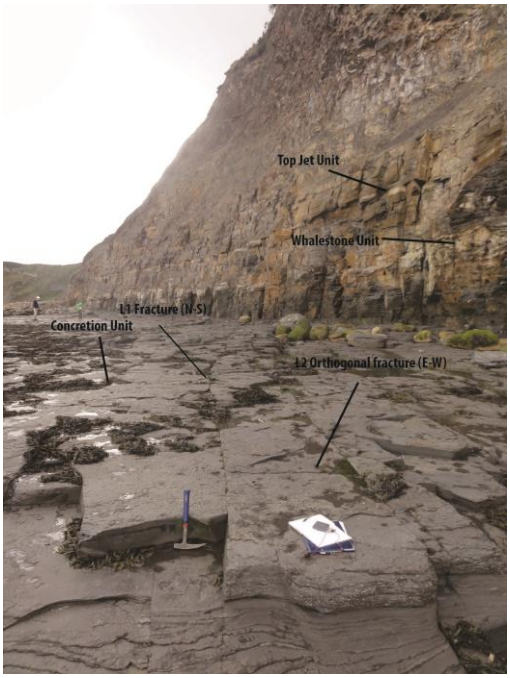

Figure 2: Showing the relation between the cliff (stratigraphic column) and one of the four pavements. This photo also shows that fractures which are present within the pavement are also present within the cliff. Direction of view is roughly to the south.

2.4. Fractures within the Whitby Mudstone

As described above, the point of this fieldwork was to measure and analyse the horizontal fracture networks present within the Jet Rock at Port Mulgrave. During this fieldwork two distinct fracture sets were observed. Hence the L1 N-S striking fracture set and the L2 E-W striking fracture set. These fracture sets appear to be sub-vertical mode I opening cracks and some N-S striking fractures even show calcite infill of the fractures. Therefore these fractures appear to have been created by an extensional regime. Imber et al. 2014 observed that the majority of the normal faults in the Port Mulgrave area strike roughly NNW-SSE, dipping (26º to 64º) to the east or west. Imber et al. 2014 also observed a second fault set striking WNW-ESE. Due to the normal character of these faults, these faults probably developed when the vertical stress was $\sigma 1$. Therefore most likely during basin subsidence (Imber et al. 2014). Figure 3 shows field measurements done on a NNW-SSE striking normal fault within the Staithes Sandstone Fm at an outcrop near Staithes. Faults observed at the Port Mulgrave area indicate that faulting postdates the deposition of the Lias group (Imber et al. 2014). Imber et al. 2014 also indicated that these NNW-SSE striking faults and the NNW-SSE striking fractures are related and are probably created during the same extensional regime. The character of the WNW-ESE striking faults and the WNW-ESE (E-W L2 fractures) also implies that these structures are related and also created under the same regional stress regime. Field observations suggest that the NNW-SSW fractures developed first within a stress field characterized by ENE-WSW minimum horizontal stress. The subsequent creation of the WNW-ESE striking L2 fractures may have occurred due to a counter clockwise rotation of the minimum horizontal stress direction, hence a regional stress change (Imber et al. 2014). These L2 fractures could also have been created by a change in local stress, which implies that both fracture systems developed at the same time. The development of the first fracture network (L1) results in a subsequent change in the local stresses in between the created fractures. This change in the local stress field may therefore result in the formation of the second fracture system, hence the L2 orthogonal fracture set (Bai et al. 2002).

Bedding parallel fractures were also observed at the Port Mulgrave area (Imber et al. 2014). These fractures can only develop within a stress field where the pore fluid pressure > vertical stress. Large increases in pore fluid pressure can be caused by a release of fluid from the rock, hence the transition from kerogen to hydrocarbon (Imber et al. 2014). Slow burial rates (20m Myr^{-1}) (Imber et al. 2014) suggest that overpressure could not have been created by normal burial processes. Therefore these fractures were created within the Oil window and therefore at depth. Cutting and branching relationships with the sub-vertical fractures suggest that both the bedding parallel fractures and the sub-vertical fractures developed simultaneously (Imber et al 2014). This indicates that the sub-vertical (L1 &L2) fractures were also created at depth (Imber et al 2014).

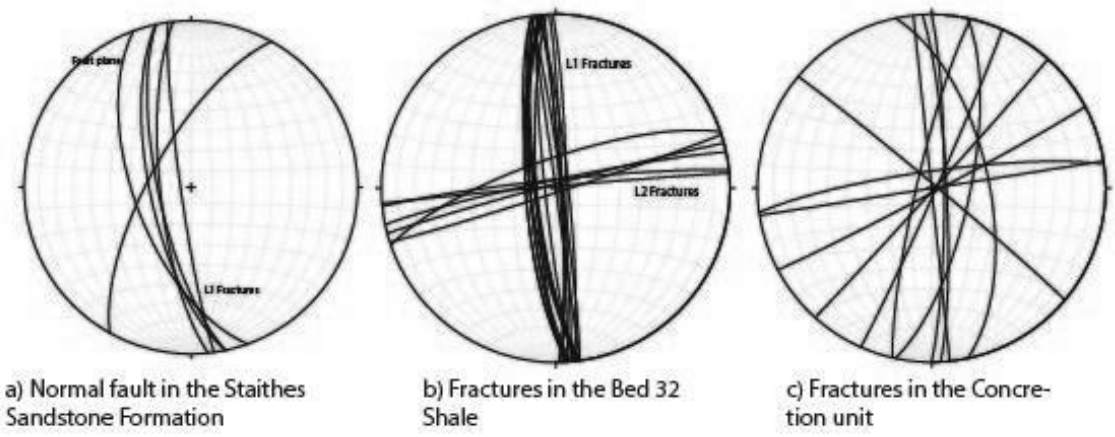

Figure 3: Showing different field measurements. a) Showing a normal fault in the Sandstone Fm, which contains steep dipping L1 fractures. b) Showing field measurements of L1 and L2 fractures within the Bed 32 Shale layer. c) Showing fractures (L1 and L2) in the Concretion unit.

3. Methods

In this part of the report the methods used for the data acquisition, sampling biases, data processing and processing biases will be explained.

3.1. Data acquisition

The data acquisition was done on the slightly SE dipping (05˚ to 08˚) pavements of the Whitby mudstone, outcropping in Port Mulgrave. Several different members of the Whitby mudstone fm are present as pavements in this area. To acquire the data from these pavements, a grid was placed on each pavement, varying in size. These grids act as guidelines for relative distances between photos, but also as line of movement for the photo acquisition. GPS data, measured in UTM, were acquired on several points of the grid in order to further refine the relative distances. Photos were made using a camera positioned at circa 3.0m above the ground, using a camera mount. To create enough overlap between the photos, the camera mount was moved at a constant speed in the y-direction, taking 10 pictures per 5.0m. A new line of photos was started circa 1.25m (in x-direction) next to the old one. Drone imagery was used to acquire the overview photos of the pavements in the Port Mulgrave area.

The resulting photos, GPS data and relative distances between specific points in the grid where used to create a 3D pavement model for each imaged observation domain. This model was created using a program called AgiSoft. The pavement models are shown in Appendix 5. Field measurements and GPS data were used to make the model more accurate. The high quantity of overlap of the photos resulted in a relative high resolution (cm scale), but also in some flaws.

Analysis of the created models was done using ArcMap. This was done by digitalizing the observed fractures and turning them into vectors which have both a length (Magnitude) and an orientation (Direction), hence creating a shapefile of the fracture network (see Appendix 5). Important to know is that if a fracture is cut off or dies out , the digitalized vector also stops. Therefore the mapping of so called fracture zones as individual vectors is not done in this report. The acquired fracture network or shapefile can now be processed using several methods which will be described below.

The above described data acquisition method does results in some sampling biases which may alter the processed results: 1) Fractures digitalized using these methods are largely dependent on the observation domain size, hence large fractures can be misinterpreted in terms of its

length. 2) Resolution of the model differs, because the camera mount was operated manually, hence smaller fractures may underrepresented in the data set. 3) Debris and rubble on the pavement results in incomplete fracture shapefiles, which may alter the results.

3.2. Data processing

The fracture shapefiles acquired from the field are processed with respect to their length and orientation, fracture intensity (P21 (1/m)), representative elementary area (REA), fractal dimension (D), cumulative length distribution (N(l, L), fracture spacing and correlation between the fracture aperture and the total fracture length. In this part of the report these methods are described in more detail.

3.2.1 Fracture orientation vs fracture length

The fracture orientation (strike) with respect to its length is processed using Digifract_V127 (Hardebol & Bertotti 2013). This computer analysis uses QGIS (OSGEO4W) and python scripting as a basis in order to process the acquired shapefiles. Digifract_V127 made it possible to derive the dominant fracture orientations within a certain length range. The results acquired by the model are plotted in rose diagrams and are described in the results part of the report.

3.2.2 Representative elementary area (REA) and fracture intensity (P21)

In order to calculate the average fracture intensity and the REA, Digifract_V127 is used, using the same acquired shapefiles. The model uses a python script which produces circles with a radius that keeps increasing until it reaches an uniform fracture intensity within the produced circle and therefore within the entire observation domain. The area of the circle now becomes the representative elementary area and the acquired P21 becomes the average fracture intensity of the domain.

3.2.3 Fractal dimension (D)

The fractal dimension of the different shapefiles is calculated using the boxcounting method which is described in formula 1:

$$D = \lim_{R\to\infty} \ln N(R)/\ln(R) \qquad (1)$$

Where N = number of boxes where a fracture set is present, R = number of boxes per unit length, formula from (Bonnet et al. 2001). In order to derive the fractal dimension of the acquired shapefiles, Matlab is used. The matlab model derives the local fractal dimension for each box size and then integrates it in order to derive the average fractal dimension.

3.2.4 Cumulative length distribution

This distribution is based on fracture statistics already described and discussed in the literature (Oddling et al. 1999, Bonnet et al. 2001, Bour and Davy 1997 & 1998, Bour et al. 2002 and Davy et al. 2010). The distribution described the number of fractures present within a data set which are smaller than the biggest fracture measured within the observation domain. In the literature the correct formula or law to describe these plots is still heavily debated, but the most prominent ones are the power law and the exponential law.
The distribution laws derived are often only best fit plots and can never truly mimic the observed data set. However the dataset itself is often strongly influenced by the biases described earlier in this report. Due to these biases (resolution and domain size), both smaller

fractures and larger fractures are underrepresented in the derived dataset. However this exact phenomenon is still a point of debate in the literature (Bonnet et al. 2001).

3.2.5 Fracture aperture vs fracture length

Vermilye and Scholz (1994) described that there was correlation between fracture aperture and fracture length. They issued a correlation formula that was dependent on the type of fracture network observed. For a single fracture system they issued that this relation was linear according to the following relationship: $A = 10^{-b} l$, where A is the fracture aperture in mm, b is a constant where 2 < b < 4 and l is the fracture length in mm. For a multifractured system they issued that the correlation was a square root function: $A = 10^{-b} l^{\frac{1}{2}}$, where again with 2 < b < 4.

3.3. Bulk rock chemistry and SEM analysis

The bulk chemistry of the acquired samples is determined by making thin sections of the samples. Samples were acquired from the concretion unit, the Bed 32 shale unit and the cannonball unit. The thin sections where carbon coated in preparation for Scanning Electron Microscope (SEM) analysis. The microscope used was a JEOL JCM600. The Microscope was operated at 15 kV and Backscattered electron (BSE) imaging has been used in combination with energy-dispersive spectrometry (EDX). Mineral and grain identification was done using the imaging and using the elemental results from the EDX. The results from this EDX analysis can be found in appendix 1.1. Photos of the samples were made in so called 'scan lines' perpendicular to the bedding. These scan lines were then used in combination with the EDX data to determine the overall mineralogy of the samples. This was done using grey scale filtering (white and black pixels) in combination with hand determination using ArcMap. Such a scan line (segmented and un-segmented) can be found in appendix 1.2. The interpreted scan lines were exported from ArcMap, and were transferred into binary models using Matlab. Segmented minerals get pixel values of 1, whereas the rest gets pixel values of 0. This has been done for: Sheet silicates, Quartz, Organic Carbon, Calcite, Pyrite, Matrix. These models were then analysed using Excel 2010, which results in a mineral percentage perpendicular to the bedding. The acquired results can be found in appendix 1.2. The average grain size was of certain mineral types (quartz, sheetsilicates and calcite) was determined using area calculations in ArcMap.

3.4. Rock strength determination and sample preparation

The field samples were also used in order to determine the Rock strength, sample density and the sample porosity. Due to the sample fragility and water-phobic nature, the normal core sampling technique could not be used. Therefore the samples were cut into rectangular blocks with the long axis being perpendicular to the bedding. Core cylinders were made manually using a polishing machine. Therefore some deviations in the cylindrical shape did occur (Ravenstein, 2014; Lie-a-fat, 2014). The acquired cylinders have a minimal diameter of 3.0cm. Porosity and density measurement were done on the samples using a Ultrapycnometer (TUDelft). This apparatus uses Helium as a fluid. The fluid is driven into the sample in pulses. This process measures the total volume of the solids within the sample chamber. So the results from the ultrapycnometer test gives the volume of the rock matrix (V_m). The mass of the sample can easily be acquired and therefore the matrix density (ρ_m) of the rock can easily be calculated using the following formula:

$$\rho_m = \frac{M_m}{V_m} \qquad (2)$$

The porosity of the samples can now be estimated using the volume formula of a cylinder $V = \pi r^2 h$. In order to decrease the inaccuracy of the measurements both the height and diameter of the samples were measured several times and averaged. The result from these measurements was an average total volume V_t, where $V_t = V_m + V_{pores}$. Using above described measurements (V_t & V_m) the porosity of the connected pore system (φ) can be determined using the following formula:

$$\varphi = \frac{\text{Vpores}}{\text{Vt}} = \frac{Vt - Vm}{Vt} \qquad (3)$$

The rock strength of the different samples is determined using unconfined pressure test at the TU Delft (see appendix 2). Before the samples were deformed in this machine the sample dimensions were accurately measured using the above described methods. In order to place the samples in the uniaxial deformation apparatus (unconfined), aluminium cylinders with a height of 4.0cm had to be placed on top of the shale samples. Since the height of all the shale samples was unsufficient (Ravenstein, 2014). For each test the amount of strain was expressed in volts and the vertical strain rate of the apparatus was 40mV/min This strain rate was applied by pumping oil beneath the lower plate, hence lifting it upwards. In order to determine the amount of strain within the shale samples, the amount of vertical strain within the aluminium sample had to be determined and subtracted first. This was done using excel and some previously defined sample parameters as found by Ravenstein 2014. The total vertical strain was measured using two Linear Variable Differential Transformers (LVDT's). The vertical compression was measured per 0.001 mm also measuring the stress within the sample at that moment. After subtracting the total strain within the Al sample the amount of strain within the sample could be determined according to following formula:

$$\varepsilon_{vertical} = \Delta L / L \qquad (4)$$

Here L represent the sample length (height) and ΔL represent the total change in sample length at certain applied force. In order to measure the amount of horizontal strain within the sample an extensometer was used. This apparatus uses a chain which is put tightly around the sample. Therefore it could measure the total expansion of the sample. The total horizontal strain could now be calculated using the following formula:

$$\varepsilon_{horizontal} = \Delta d / d \qquad (5)$$

Where d is the sample diameter and Δd is the change in sample diameter. Knowing the above described data and plotting it in graphs the following sample constants can be determined or calculated:

$$C_{yield}$$

$$E = \sigma / \varepsilon_{vertical} \qquad (6)$$

$$v = -\varepsilon_{horizontal} / \varepsilon_{vertical} \qquad (7)$$

Where C_{yield} is the yield strength and is determined using the resulting graphs which are shown in section 4.8, E is the Young's modulus of the sample, σ is the applied stress (MPa) and v is the Poisson's ratio of the sample. All the results from these test are shown and illustrated in section 4.8.

4. Results

In this part of the report the results will be presented and described. This will be done by describing the data per method and then subdividing the data per observation domain. The data will be presented in the following order:

1) Part 4.1 will describe the geometry of the different domains in terms of the fracture network itself.
2) Part 4.2 will focus on observations of the fracture orientation vs. the fracture length and how you can distribute the data set.
3) In part 4.3, the calculations and results of the Representative Elementary Area (REA) are presented and described.
4) This is followed by a description of the calculations and results of the fractal dimension of the different domains.
5) Part 4.5 will describe the cumulative length plots of the different fracture networks. The presented data will then be used to empirically and statistically derive relations on how the fracture network behaves.
6) Part 4.6 will describe the method used to acquire a relation of fracture aperture vs. fracture length using measured field data of calcite veins.
7) In part 4.7 the mineralogy of the different layers will be analyzed and described in terms of matrix mineralogy and the mineralogy of the larger grains.
8) Part 4.8 will describe the geomechanics and rock characteristics of each sample. Data like matrix porosity, Young's modulus and poisson's ratio will be presented.

4.1. Fracture network geometry

The position of the digitalized fracture networks is illustrated in figure 4, this figure shows the geometry of the different observation domains. The geometries of the these networks show differences as well as similarities. All fracture networks show a dominant N-S orientation. Figure 5 shows that smaller fractures fill in the places in between the N-S orientated fractures. All the fracture networks show an orthogonal geometry however some branching effects are also observed. Figure 4, also shows that some large (up to 60m long) N-S striking fracture zones can be determined. These fractures zones are made of several individual fractures connected together and are the largest structures observed in the area of interest. However this part of the report will focus on the geometry of the fracture networks within the different observation domains.

Figure 4: Showing the overview map of Port Mulgrave and different N-S striking fracture zones which have a length > 10m. These zones are interpreted using Birdseye view drone imagery. These zones are not individual fractures but are made up out of several larger N-S striking fractures. Indicated in black are the different observation domains.

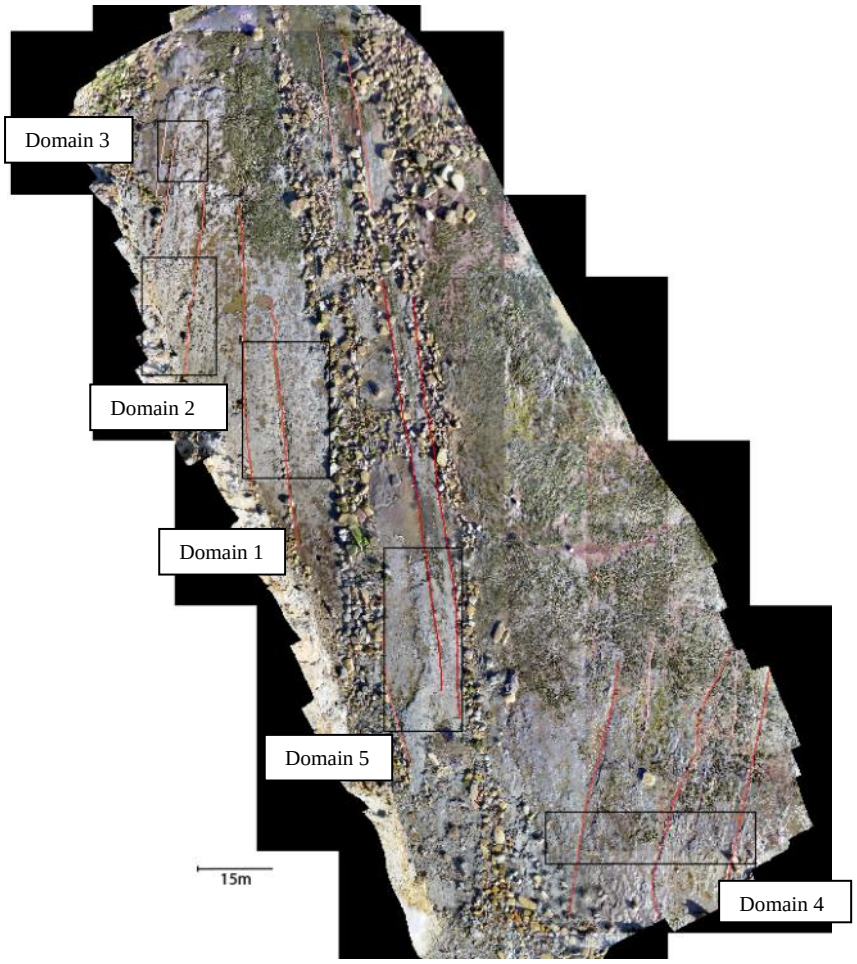

The fracture network observation domain 1 (Figure 5a) shows a network within the "concretion unit". First order analysis indicates that the larger fractures, length > 1.5m, are more prone to have a N/S orientated strike. Smaller cross joints (joints in between larger fractures; Bai et al. 2002) are also observed (see figure 5). A first order observation about this fracture network is the fact that individual N-S striking fractures barely reach lengths greater than 5.0m within the observation area. These N-S striking fractures are often cut off by a smaller fracture or it branches out into several smaller fractures. The larger N-S striking fractures do create N-S striking fracture zones. These fracture zones can reach lengths which exceeds the observation area. Both these effects result in the dense fracture network of smaller fractures going into several directions, however the main direction for the larger fractures is N-S, the main direction for the smaller cross joints is E-W.

The fracture network in observation domain 2 (Figure 5b) also shows a fracture network positioned within the "concretion unit". Again the larger fractures within the system are mainly striking in a N-S direction. Smaller E-W striking fractures are also observed within this observation area. Again fracture lengths greater than 5.0 m are barely observed. Again the larger N-S striking fractures do create N-S striking fracture zones which exceed the observation area, hence reaching lengths greater than 15.0m. Therefore the branching and cut off effects again result in a very dense fracture network which mainly consists of smaller fractures. Small cross joints which fill in the spaces in between the larger fractures are also observed, indicating that an orthogonal component is also present within this fracture network.

The fracture network in observation domain 3 (Figure 5c) shows a network positioned at the top of the grey shale formation. Again this fracture network exhibits fractures with a dominant N-S trending strike. A clear difference between this fracture network and the fracture networks described above is the fact that the branching effect is much less dominant, so that single fractures larger than 5.0m are more dominant in this network. Again orthogonal cross joints fill in the spaces in between the larger fractures. These cross joints are both N-S as well as E-W orientated. Therefore based on the geometry, this fracture network appears to be an orthogonal fracture network.

Observation area 4 (Figure 5d) shows the digitalized fracture network positioned in the "cannonball unit". Just like fracture network 1 and 2 this fracture network appears to be affected by branching effects. However the largest (NNE-SSW) striking fractures zones observed in this observation domain are not influenced at all. These fractures appear to create NNE-SSW striking fracture zones which exceed the length of the observation area, and tend to be longer than 20.0 meter. In between the larger fractures the geometry of the fractures appear to be fairly similar to those of observation area 1 and 2, showing both branching of fractures and the presence of cross joints. Only the density of the fracture network appears to smaller. The smaller cross joints which fill in the spaces in between the larger fractures show a dominant E-W strike. These fractures are therefore orthogonal to dominant NNE-SSW strike of the larger fractures and fracture zones.

Observation area 5 (figure 5e) shows the fracture network positioned in the "Bed 32 shale unit". This fracture system is somewhat different from the networks developed in the other units. This system shows large N-S striking fractures with E-W striking cross joint in between. However these cross joints appear to have cross joints of their own which again strike in a N-S orientation (See figure 5e). Hence this network shows a purely orthogonal fracture network with its typical ladder like geometry (Bai et al. 2002, Rawnsley et al. 1992). Due to the lack of branching effect the density of the fracture network appears to be much less dense.

Figure 5: Showing the digitalized fracture networks from the different observation areas. Scale is shown by UTM coordinate grid measurements over which the number are on the meter scale. Blue coordinates represent N-S movement, black coordinates represent movement in an east west direction.

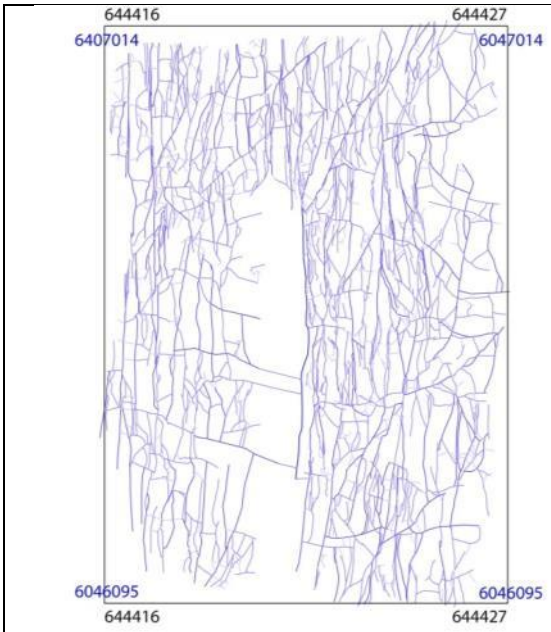
644416
644427
6407014
6047014
6046095
6046095
644416
644427

a)

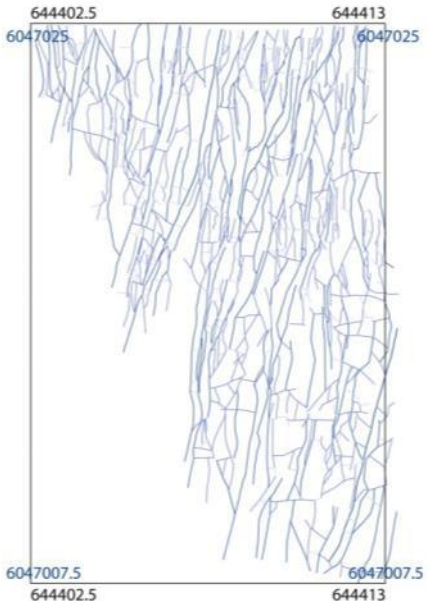
644402.5
644413
6047025
6047025
6047007.5
6047007.5
644402.5
644413

b)

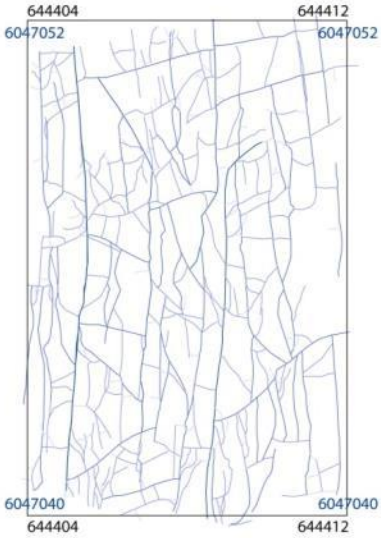
644404
644412
6047052
6047052
6047040
6047040
644404
644412

c)

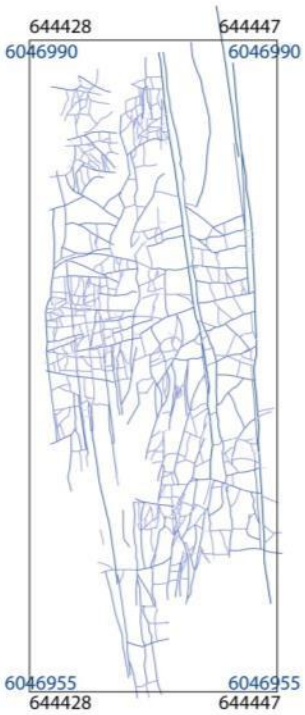
644428
644447
6046990
6046990
6046955
6046955
644428
644447

e)

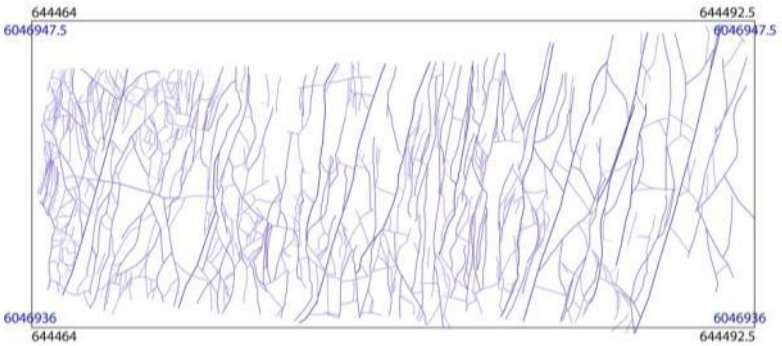
644464
644492.5
6046947.5
6046947.5
6046936
6046936
644464
644492.5

d)

4.2. Fracture length vs. Fracture orientation

The geometries and fracture networks described above are now analyzed by orientation plots as a function of its fracture length scale. Rose diagrams are presented (Figure 6) of the different domains, which are described together due to cross comparison in the datasets. However specific differences will be stated and will therefore be described per observation domain.

The general observation which was also observed while looking at geometry of the fracture networks, is that the longer fractures ($l > 2.0$m) generally strike N-S. Therefore these fractures can be subdivided from the smaller fractures by calling them L1. These L1 fractures either create a large N-S striking fracture or are present within a larger N-S striking fracture zone/network. The rose diagrams also illustrate (see Figures 6 a till e) that at the smaller ranges ($l < 0.4$m), the fractures show a peak in the E-W strike. However, depending on the fracture network, the smaller fractures also show a 0-360 degree spread in strike, which is probably a result of the branching effects. These smaller fractures can be subdivided from the larger fractures by calling them the L2 fractures. The rose diagrams (Figure 6) also indicate that the peak in strike of the smaller L2 fractures is dependent on the peak strike of the larger L1 fractures. Hence the peak strike of the L2 fractures appears to be always orthogonal to the dominant strike of the L1 fractures. For example; the rose diagrams from observation area 4 (see Figure 6e) show that the NNE-SSW striking L1 fractures and the peak in strike of the L2 fractures is WNW-ESE. The same observation is made in the other observation areas (see Figures 6a till e). Therefore the peak strike of the L2 fractures describes the orthogonal component of the observed fracture network.

The rose diagrams also show differences in the units which do contain concretions and formations which do not. Hence networks present within unit with concretions still show that the L2 fractures have a peak in strike which is roughly E-W, however these figures also show a lot scatter in the strike L2 fractures as was described above (see figures 6a, 6b & 6d). This spread of the L2 fractures was already observed in the geometry of the fracture networks which was described above (see Figure 5). The fracture networks observed within units which do not contain any concretions (Figure 6c & Figure 6e) show somewhat different rose diagrams with respect to the smaller L2 fractures. For example; fracture domain 3 (Figure 6c) shows that a conjugate set with respect to the N-S striking L1 fractures becomes dominant, for fractures where $l < 1.6$m and still being present for fractures where $l < 0.4$m. The rose diagrams of fracture network 5 (Figure 6e) perfectly illustrate an orthogonal fracture set. This Figure indicates that E-W striking fractures are already present for $l < 6.3$m. However another important observation concerning the fracture network in domain 5 is that N-S strike never loses its dominance, even not for the fractures where $l < 0.4$m. The smallest N-S striking L2 fractures are fractures which are orthogonal to the E-W striking fractures, which have a $l > 0.4$m. This was also already observed in geometry of the fracture network (see Figure 5). Overall these rose diagrams which are plotted as a function of the length scale can help in illustrating the dominance of the different effects (branching and/or orthogonal fracturing) concerning the observed fracture networks. The diagrams indicate that the fracture networks in observation domains 1, 2 and 4 have a system which are effected by both branching and orthogonal fractures and that the fracture networks from observation areas 3 and 5 show a system which is mainly effected by orthogonal fractures.

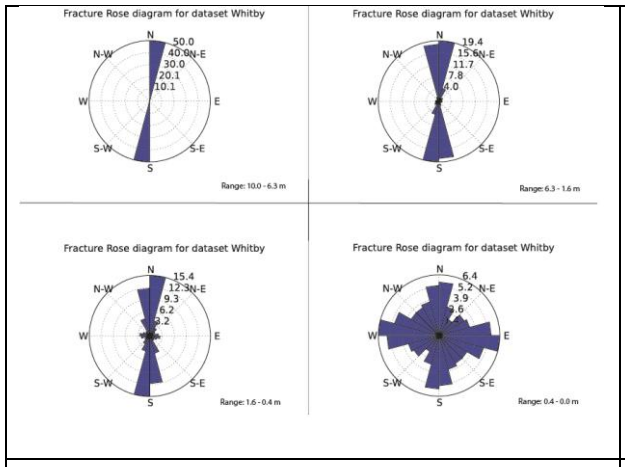

a)

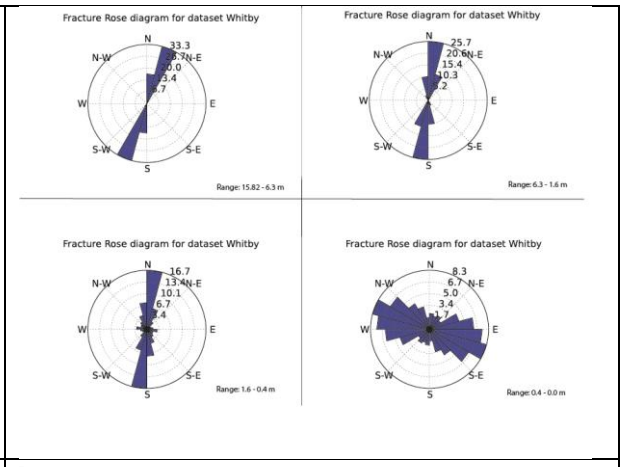

b)

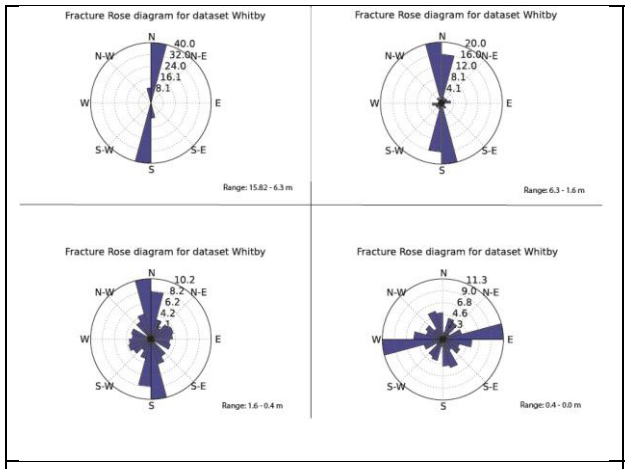

c)

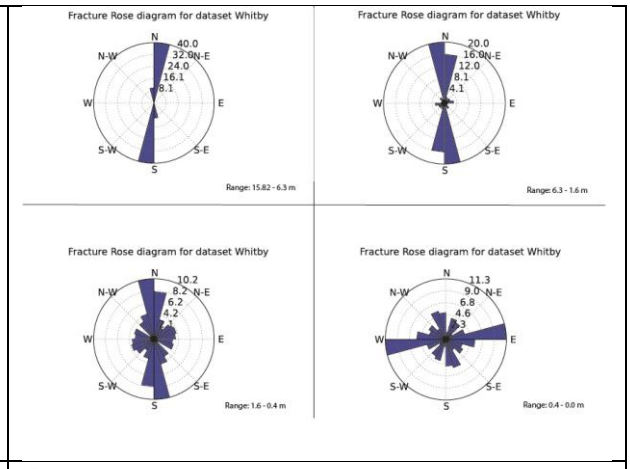

d)

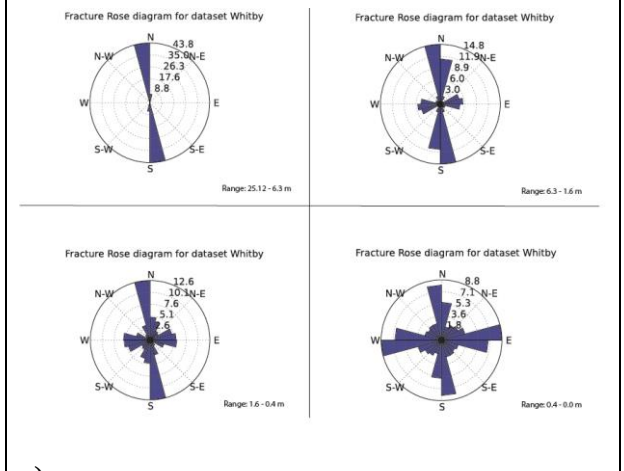

e)

Figure 6: Showing the different rose diagrams of the observation domains researched. Where a) represent observation domain 1, b) represent observation domain 2 and so on. Ranges of the rose diagrams are: Max length - 6.3m, 6.3m – 1.6m, 1.6m – 0.4m and 0.4m – 0.0m. Starting top left.

4.3. Representative Elementary Area (REA) and Fracture intensity (P21)

DigiFract scripting (Hardebol & Bertotti 2013) has been used to determine the REA and P21 of each observation domain. Both these properties are plotted and modelled against each other to accurately determine the average fracture intensity for a certain REA. P21 can be calculated using the following formula (after Mauldon & Delschowitz 2000):

$$P21[\frac{1}{m}] = \frac{Length\ of\ fracture\ traces\ [m]}{Area\ of\ exposure\ [m^2]} \quad (8)$$

Therefore the REA indicates the smallest area over which the fracture intensity (P21 [1/m]) remains constant. Figure 7 shows the plots which will help in determining both these properties.

The analysis from DigiFract works as follows; you start with small circle, which may therefore contain a high P21 or a very low P21 (as can be seen in Figure 7). Step by step (steps of 0.25m) you will enlarge the radius of the circle, hence the area of exposure, until you derive a constant P21 for each circle plotted on the domain. When reached, you will now have the average fracture intensity and the REA.

However the analysis has two major sampling biases; which are the accuracy or quality of the acquired data and the presence of sea water, sea weed and boulders in the observation area. These biases create areas where it is impossible to see and determine fractures while it is possible that they are present. This therefore results in gaps in the data set and may therefore result in a lower P21.

The calculated P21 and REA do confirm the result presented in part one of the results section. Again this figure shows that Domain 1 and 2 are relatively intensely fractured and that the other observation areas are relatively less intensely fractured. The overall results are plotted in Table 1. Apart from the differences in fracture intensity, another relation can be observed. This is relation between P21 and the corresponding REA, which becomes smaller the higher P21 becomes.

Domain #	**Unit**	**P21 [1/m]**	**REA (window size [m])**
Domain 1	Concretion unit	6.05 +- 0.02 (1/m)	3.25 m
Domain 2	Concretion unit	5.75 +- 0.05 (1/m)	4.0 m
Domain 3	Top Grey shale fm	4.0 +- 0.05 (1/m)	4.0 m
Domain 4	Cannonball unit	3.0 +- 0.25 (1/m)	5.25 m
Domain 5	Bed 32 shale unit	3.25 +- 0.25 (1/m)	5.5 m

Table 1: Showing the results of the P21/REA analysis described above.

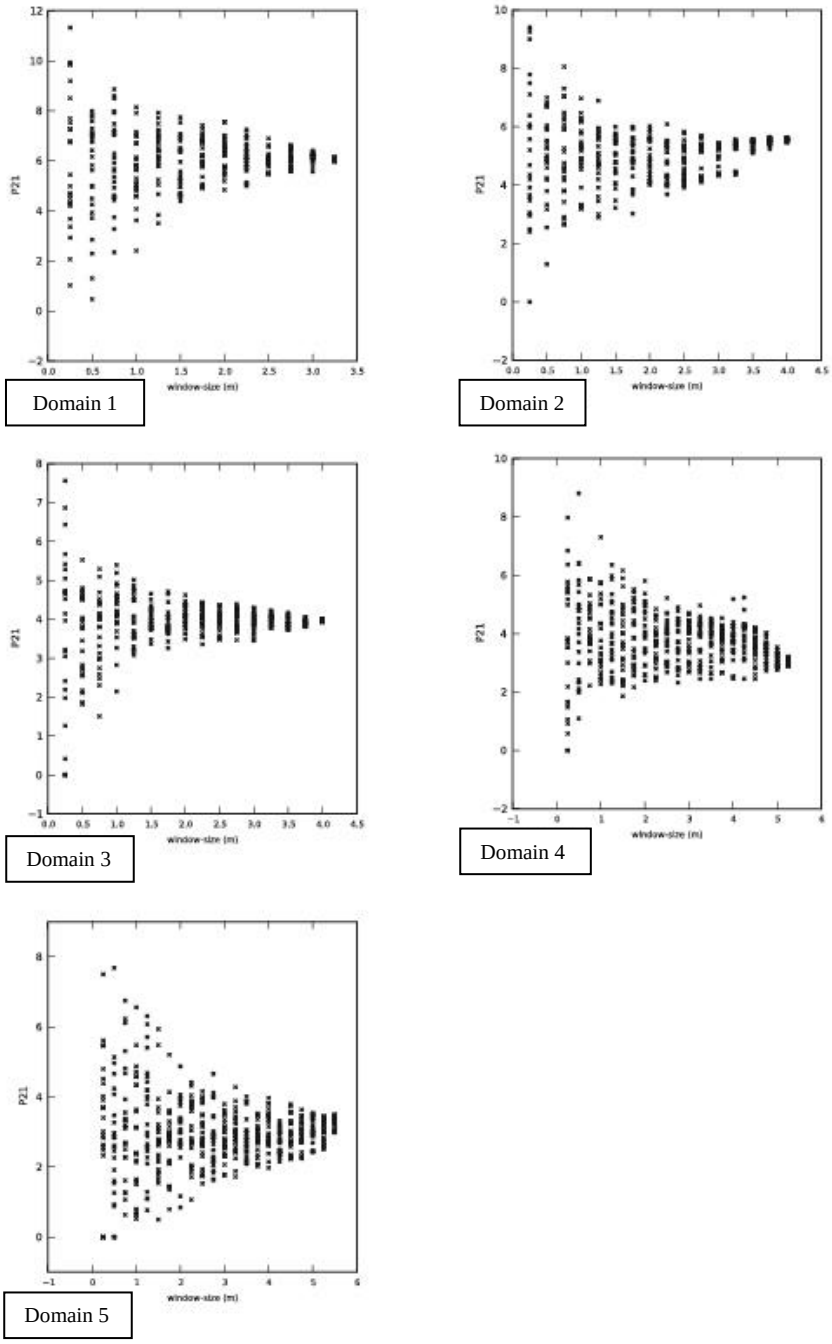

Figure 7: Showing the P21 and REA calculations for each observation domain. Where observation domain 1 is represented by a) observation domain 2 by b) and so on.

4.4. Fractal dimension of the observed fracture networks

The fractal dimension of each observation domain was calculated using the boxcount method, which is accurately described by Bonnet et al. 2001. The fractal dimension was derived using a boxcount matlab method (copyright and all right reserved to Frederic Moisy 2008) and the following formula:

$$D = \lim_{R\to\infty} \ln N(R)/\ln(R) \quad (9)$$

Where D = the fractal dimension, R = the size of the boxes (unit size) and N(R) are the number of boxes needed to fill the set (Formula from bonnet et al. 2001). The results of the matlab modelling are plotted in Figure 8 a till c and appendix 3. The model assumes that the network used behaves in a fractal manner, according to the following formula (Power law):

$$N(R) = N0 * R^{-D} \qquad (10)$$

So that the number of boxes needed to fill the set is dependent on both R and D. Using the above stated assumption, the model operates according to the following steps:

1) A small high resolution piece (square) is chosen from the fracture network. Line width of the selected fractures is set to 2 using ArcMap, if not the matlab analysis will not include all the selected fractures. This figure is then analysed by matlab, which creates a binary model having values 0 or 1 (see Figure 8a and appendix 3).
2) Then the method calculates the N(R) term and plots it for each used box size (R).

Figures 8b and appendix 3. These Figures illustrate how the power law function of the fracture networks (blue lines) starts to deviate from the power law function of a space filling object (red lines). The power law function of the space filling object (red line) has a D of magnitude 2.0. The power law function of the observed fracture networks (blue lines) has a D which is less than 2.0, because its starts to deviate away from the red line as the box size (R) starts to decrease. Therefore the fractal dimension of the fracture networks has to be less than 2.0, making the network not entirely space filling.

3) This method is now used to calculate the local fractal dimension for each given box, these results are plotted in Figure 8c and appendix 3. The method now uses these figures in combination with formula 10 in order to calculate the average fractal dimension of each domain. The results of these calculations are summarized in table 2.

Domain #	Formation	Fractal dimension D	uncertainty
Domain 1	Concretion unit	1.7495	+/- 0.16796
Domain 2	Concretion unit	1.7112	+/- 0.18276
Domain 3	Top Grey Shale fm	1.6094	+/- 0.25874
Domain 4	Cannonball unit	1.6784	+/- 0.19767
Domain 5	Bed 32 Shale unit	1.6382	+/- 0.24000

Table 2: Showing the results from the fractal dimension analysis

Overall table 2 and appendix 3 indicate that all fracture networks show a fractal dimension of ranging between 1.6 and 1.75. Therefore the fracture networks indicate non space filling behaviour. 2D computational models done by Bonnet et al. 2001 showed that the fractal dimension determines the degree of clustering in the system, hence the degree of space filling. The 2D models kept all factors except for the fractal dimension constant. Results showed that synthetic models which had a high fractal dimension (D = 1.9) had a less clustered system than models which had fractal dimension of 1.5. Twiss and Moores 2007 also indicated that a lower fractal dimension results in a more clustering system. Therefore the results indicate that the digitized fracture networks differ in degree of clustering. The results from domain 2 till 5 are shown in appendix 3.

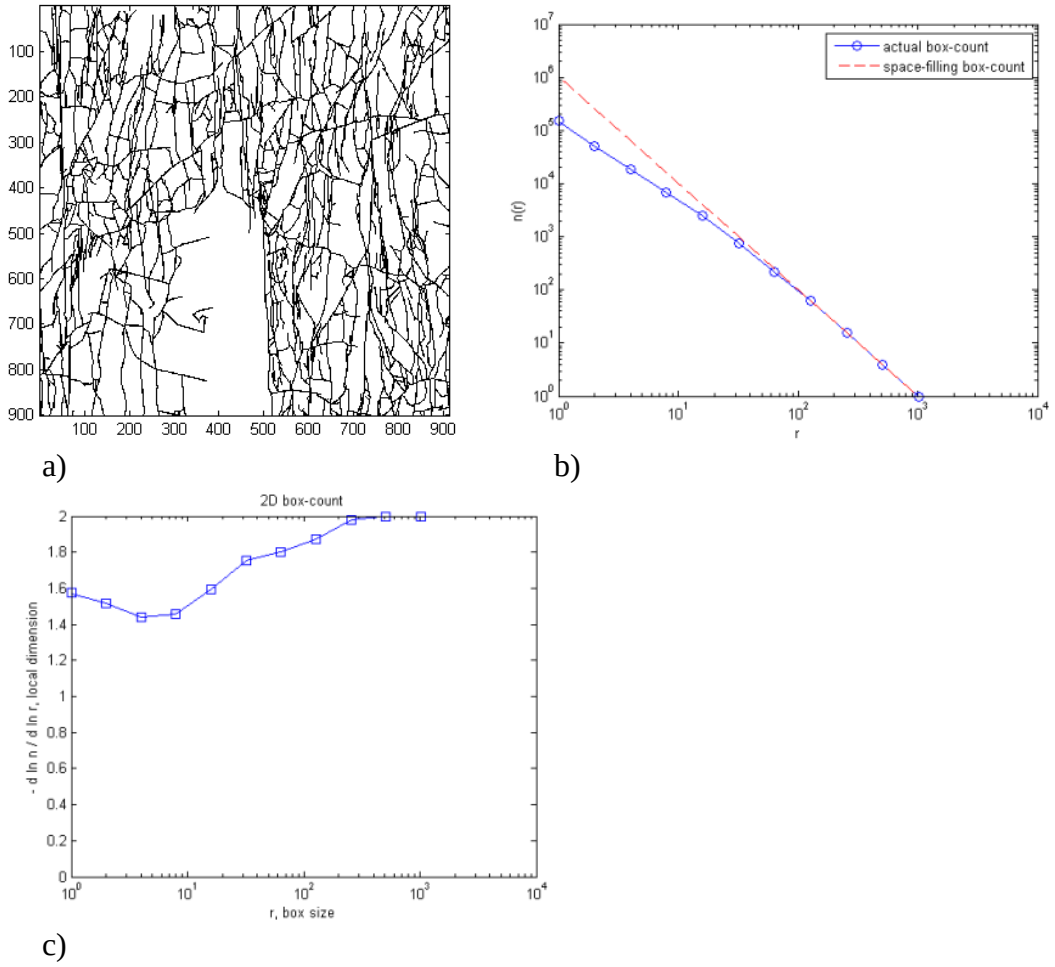

Figure 8 (a, b & c): Showing the fracture network of domain 1. This is network is digitalized in a binary systems which is shown in figure a, where black is 1 and white is 0. The N(R) vs. R log scale plots are shown in figure b, where the plotted network is illustrated by the blue line and a space filling object is illustrated by the red line. Figure c shows the local fractal dimension (d = ln N(R)/ln R) which is then used to calculate the average fractal dimension.

4.5. Cumulative length distribution of the different fracture networks

In order to better understand the way that fracture systems behave in terms of its cumulative length distribution a lot of research is done and discussed in the literature (Oddling et al. 1999, Bonnet et al. 2001, Bour and Davy 1997 & 1998, Bour et al. 2002 and Davy et al. 2010). Therefore in order to better understand the fracture networks of the Jet Rock, cumulative length distribution plots are derived with the available fracture data. The plots are created and analysed using Microsoft Excel 2010 and fracture statistics. A cumulative length distribution (N (l, L)) is nothing more than a plot which defines the number of fractures which are smaller than the largest fracture measured in the system. This largest fracture is then defined as 1. However this method has some major sampling biases which can greatly alter the results as discussed by Bonnet et al. 2001. These sampling biases are resolution of the data set and system size. The resolution bias can greatly influence the number of smaller fractures counted in the system. Examples of such a resolution bias are: the resolution of the acquired orthophotos, boulders, seawater and seaweed (which influences both the resolution and the effective system size of the acquired orthophotos). The system size sampling bias cannot only greatly influence the number of larger fractures counted in the system, but it can also greatly

reduce the length of the largest fracture. Since you cannot measure outside your previously determined domain size. Therefore the maximum fracture length which can be acquired using this method is dependent on the effective system size of the chosen domain. However taking these biases into account, a cumulative length plot can still help in understanding a derived fracture network. The results are accurately described for domains (Observation area) 1 and 5. The rest of the acquired result are shown in Table 3 and the acquired graphs can be found in appendix 4.

Domain 1 shows a fracture network which is both influenced by orthogonal fractures and branching effects. This resulted in the dense fracture network, which was described earlier in this report. The data plots are illustrated in Figure 9 (a & b), which show both a log scale plot and a log scale, normal scale plot. Using the data set (blue dots) you can now try to empirically derive a law which can describe the observed fracture geometry. The data set shows that the data behaves according to an exponential law having the following formula:

$$\boldsymbol{N(l, L) = A\, e^{-(c)l}} \quad \textbf{(11),}$$

where A is a constant with a value of 1434.1 and c is the exponential component which has a value of 1.378. Figure 9b) indicates that this exponential law only holds for fractures where l < 1.37m and that for fractures bigger than 3.0m the exponential law start to deviate from the data set.

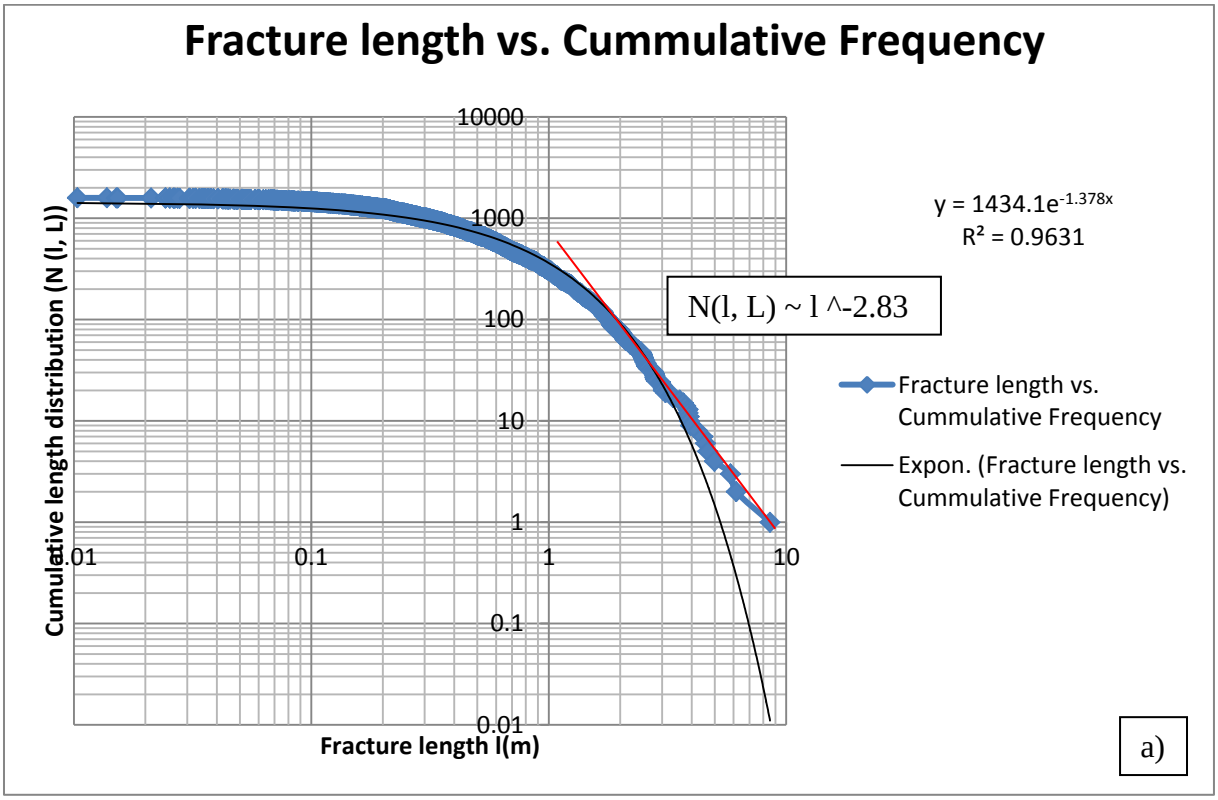

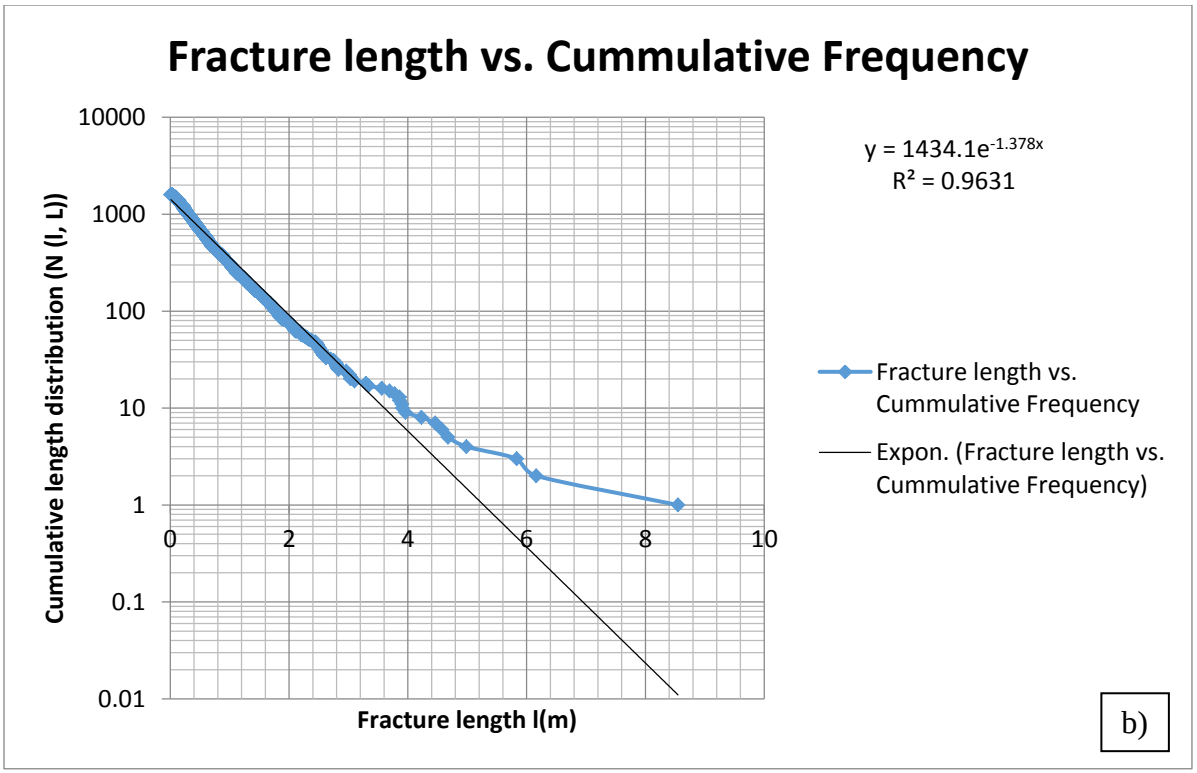

Figure 9 a) Showing the cumulative length distribution of observation domain 1 on a log scale plot and two best fitting laws which try to simulate the observed data set. b) Showing the same data set but no the x-axis is now on a normal scale.

The data now starts to behave more according to the power law (red line) which follows the following formula:

$$N(l, L) \sim l^{-a} \quad (12)$$

Where a is the power law relation, relating l to N (l, L) and having a value of 2.836. Overall the results of observation domain 1 indicate that the fractures behave according to two empirically derived laws which depend on the fracture length itself.

Observation domain 5 holds a fracture network positioned within the Bed 32 Shale formation. As described earlier in the report the fracture network shows a ladder like pattern (Rawnsley et al. 1992) and shows a high quantity of orthogonal fractures and cross joints. The cumulative length distribution of observation domain 5 is illustrated in Figure 10 (a & b). This figure indicates that the cumulative length distribution behaves according to a power law, at least for fractures with a length greater than 1.3m. Fractures which are smaller, again behave according to an exponential law. However no clear law is defined. Therefore it is most likely, especially when looking at figure 10 a & b, that the distribution occurs according to the following power law:

$$N(l, L) \sim l^{-a}$$

With a power law exponent (a) with a magnitude of 1.67. Fractures which are smaller than 0.5m do deviate from this law however with the current data set this power law shows the best fitting results.

The cumulative length distribution results from observation domains 2, 3 and 4, together with results described above are summarized in table 3. The acquired graphs are plotted in appendix 4. The results either show a distribution which corresponds with the results from domain 1 or distributions are similar to results of domain 5. The results show that both domains 1 and 2 are more prone in following the exponential law. Both domains are also positioned in the concretion unit. The cumulative length distribution concerning the other domains are more likely to follow the power law. All the acquired results (appendix 4) show a large deviation from the power law regarding the smaller fractures (l < 1.0m). Larger fractures (l > 10.0m) are rare. Both these factors can partly be explained by the sampling biases explained earlier, which where the resolution of the photos and the actual size of the observation area. Bonnet et al. 2001 used these sampling biases in order to explain the deviations from the power law concerning other natural data sets.

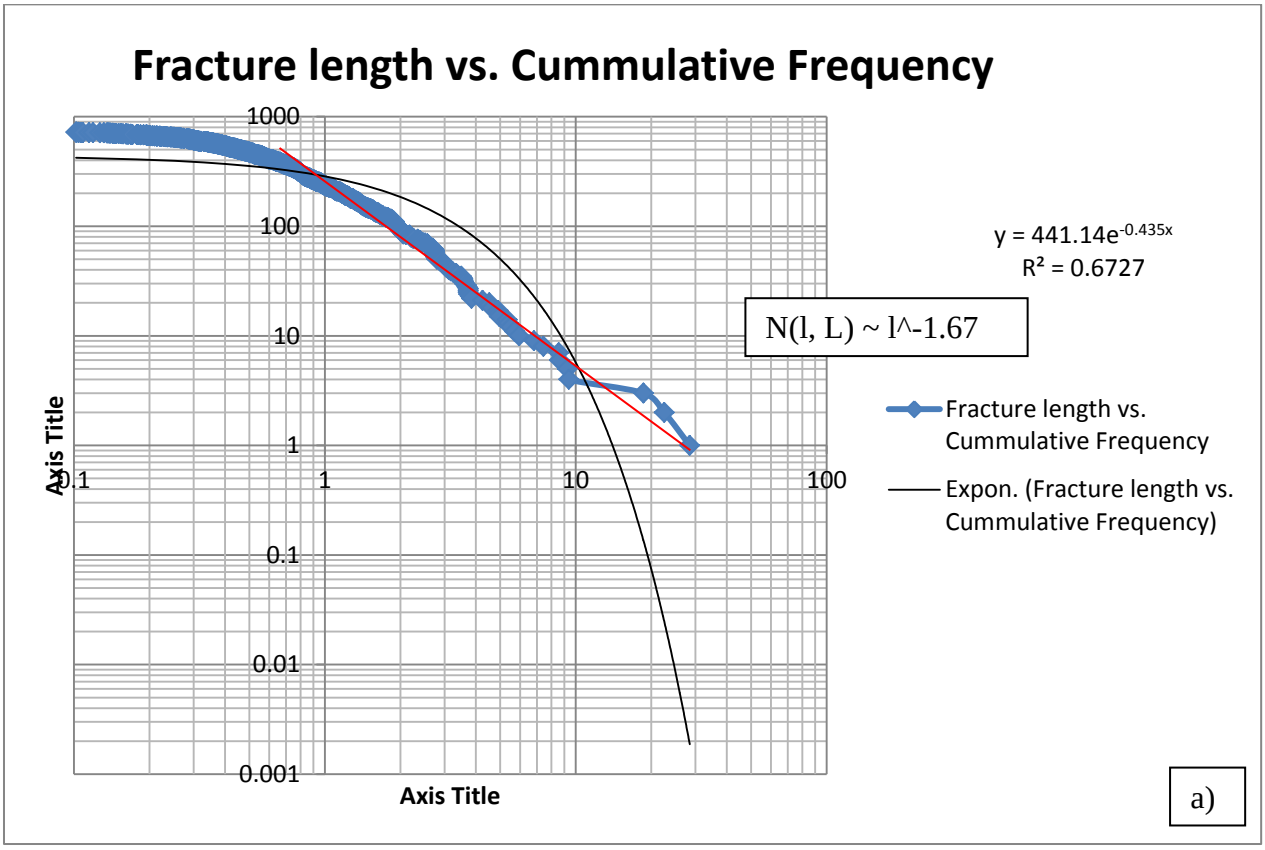

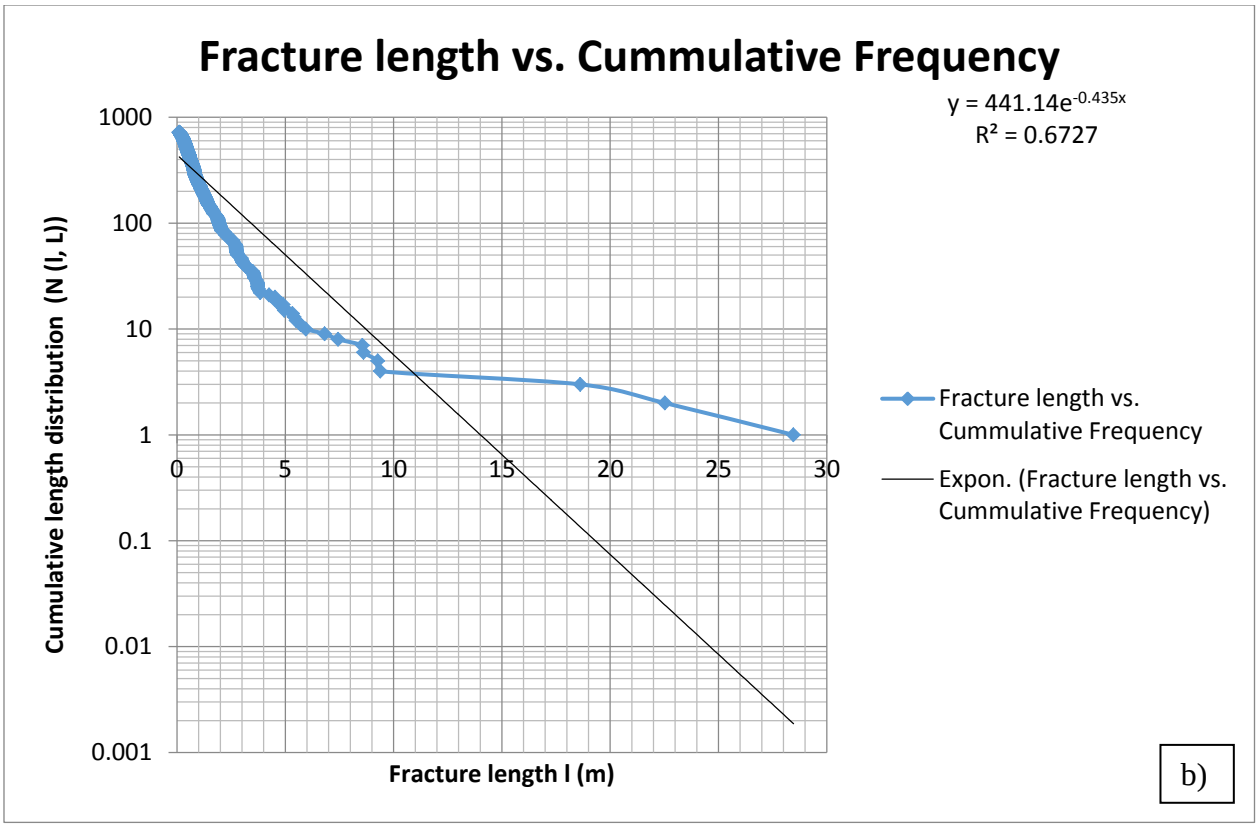

Figure 10 a) Showing the cumulative length distribution of domain 5 on a log scale plot and two best fitting laws which try to simulate the observed data set. b) Showing the same data set but no the x-axis is now on a normal scale. These figures show that the fractures of domain 5 behave according to a power law and that only for fractures with l < 1.30 m it starts to behave more like an exponential function.

Domain #	Member	Exponential Law	Power Law	A, a, c values
Domain 1	Concretion unit	l < 1.37m	l > 1.37m	A = 1434.1 a = 2.836 c = 1.378
Domain 2	Concretion unit	l < 3.0m	l > 3.0m	A = 683.14 a = 3.508 c = 0.996
Domain 3	Top Grey Shale fm	l < 0.80m	l > 0.80m	A = 264.22 a = 1.53 c = 0.662
Domain 4	Cannonball unit	l < 2.01m	l > 2.01m	A = 822.14 a = 2.109 c = 0.815
Domain 5	Bed 32 Shale unit	l < 1.30m	l > 1.30m	A = ? a = 1.67 c = ?

Table 3: Showing all the cumulative length distribution results from the different domains. The results show that the domains positioned in the concretion unit or more prone to follow

an exponential law regarding its length distribution. The other domains are more prone in following a power law, only the smallest fractures appear to follow an exponential law.

4.6. Fracture aperture vs. Fracture length

Fracture network permeability dependents on fracture aperture; hence the aperture of a fracture defines how much fluid can flow through the network. Therefore the above posted relationship is an important feature discussed in the literature. In this report, measurements on fracture aperture where done using those veins, that where visible as white stripes on the orthophoto. ArcMap was used to accurately measure the maximum vein width up to mm scale. However only the orthophotos of the fracture network present in observation domain 1 had a high enough quality to permit the acquisition of the small vein apertures. In total, 39 veins were measured having a variety of lengths and orientations. These measurements are now used to empirically derive a relationship between fracture aperture and fracture length. The measurements done on observation domain 1 are plotted in figure 11 This figure indicates that the fracture aperture vs. fracture length relationship behaves according to an empirically derived square root function with the following formula:

$$A = 5.35 \cdot 10^{-2} \cdot \sqrt{l} \quad \textbf{(13)}$$

Where A is the maximum fracture aperture (mm) and l is the fracture length (mm). This relation is derived statistically and has a reasonable R^2 value of 0.88.

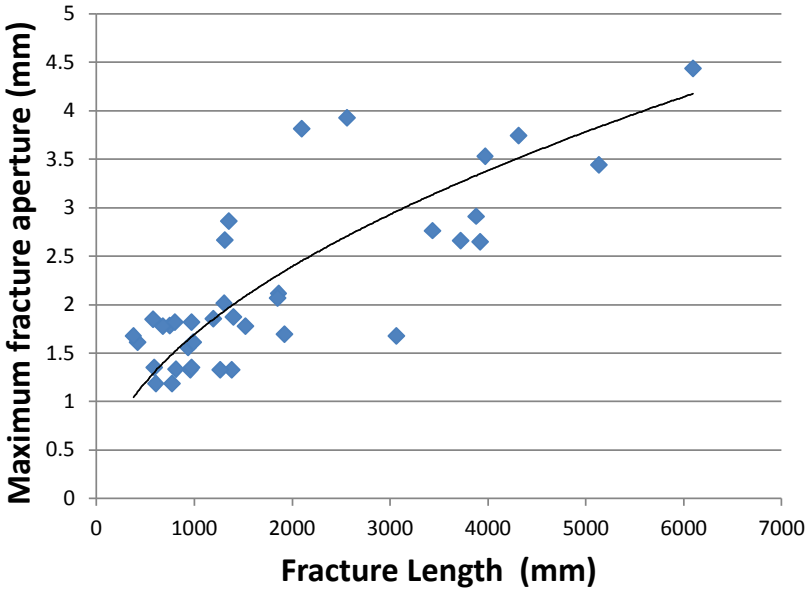

Figure 11: Showing the different vein aperture measurements done on the fracture network of observation domain 1 (blue points). The data indicate that the fracture aperture vs fracture length relation behaves according to a square root law. This square root law is illustrated by the black line.

4.7. Bulk rock composition of the different samples

In this part of the report the mineral composition of the different layers and samples is analyzed using SEM/EDX analysis and XRF analysis done by Joella Lie A Fat at TUDelft 2014. The results are analyzed per layer, starting at the bottom of the stratigraphic column. Hence the concretion bed.

The results are shown in Table 4 a & b, Figure 12 and in appendix 1.2. The SEM analysis Figures are scan lines taken perpendicular to the bedding at magnification = 1000x. At first glance, it is easy to recognize that there are some differences between results from the SEM analysis and the results from the XRF. This difference occurs because the results from the SEM are hand interpreted using ArcMap. Using this methods it is possible to detect organic carbon and average grain size but impossible to accurately determine the mineralogy of the matrix (all grains smaller than 2µm in diameter). Therefore minerals like quartz and calcite can be underappreciated using SEM images, because only the notable grains can be observed. Therefore a lot of quartz and some calcite is present within the matrix of the rock as can be seen by the higher percentages. The XRF data also indicates that different clay minerals are present within samples. These clay minerals most likely make up the bulk of the un-interpreted matrix from the SEM images. The chlorite and goethite (see Lie A Fat, 2014) is also un-interpreted using the SEM analysis and may therefore also be present within the matrix of the samples.

The SEM analysis Figure from the concretion unit (Sample 4) is shown in appendix 1.2.3 and in table 4. The Figure shows that relatively large quartz and calcite grains are often deposited in bands which coincide whit a drop in total matrix percentage and therefore a drop in clay minerals. The graph furthermore shows that the organic carbon is also deposited in layers as is indicated by the peeks in relative organic carbon percentage. Some organic carbon is also present within the matrix. Relatively Large sheet silicate minerals are often deposited together with the bands of quartz and calcite. Pyrite minerals often occur together with calcite and quartz minerals, however it is also widely distributed throughout the matrix. Therefore no real peaks along the bedding in total percentage of pyrite are observed.

The SEM analysis sample 1 (Bed 32 shale unit) is split up into two parts (see figure 12 and appendix 1.2.2). We will start with describing the results from the bottom part of sample 1 which is shown in appendix 1.2.2. Quartz and calcite minerals seem to be much more widely distributed, and therefore seems much less layered, when being compared to the results from the concretion unit (Sample 4). However some aggregates of relatively large grains are still present, which is indicated by an increase in increase in total quartz percentage and a drop in matrix percentage. Pyrite grains often occur together with larger quartz and calcite grains and this is also seen by the peak in total pyrite percentages. Pyrite grains/framboids are distributed throughout the matrix. Organic matter is present in large rectangular areas which are parallel to the bedding, and the organic matter is less layered then in sample 4. However the total organic carbon content does increase when going towards the top of the sample, indicating that the TOC percentage differs throughout the Bed 32 shale layer. This can also be seen in figure 12, which is the upper part of sample 1. This figure shows more or less the same geometry as the lower part of sample 1. However it shows much more organic carbon, which is most frequent in the middle of the scan line. Again indicating that organic carbon deposition is not uniform throughout sample 1. Overall sample 1 shows a relatively high TOC percentage ranging between 11.98% and 20.98%.

Sample 7 is part of the cannonball dogger layer (see appendix 1.2.4). This sample shows relatively high total matrix percentages. Some larger grains of calcite and quartz are also observed and often occur together. Pyrite is often seen within large calcite or quartz grains. The scan line also indicates that larger grains are more frequent at the bottom of the scan line. Total organic carbon content is relatively low within this sample and it is present within the matrix. The results also indicate that quartz and some other minerals are possibly present in the matrix.

Overall the results indicate that the mineral composition apart from the total organic carbon does not show large changes. The XRF data shows that the relative clay content is higher within the Bed 32 shale layer, which also shows the highest TOC value. The average grains size also appears to vary, being larger within sample 4 and 7. However the smaller grains within the matrix remain un-interpreted. Therefore this difference in average grain size only appeals to the larger, interpreted grains.

Sample #	Unit	Matrix (%)	Quartz (%)	SheetSilicates (%)	Calcite (%)	Pyrite (%)	TOC (%)	Avg Grainsize (mm^2)
Sample 7	Cannonball unit	81.17%	7.98%	4.03%	1.85%	1.14%	3.81%	**Qtz:** 0.0089639 **Calcite:** 0.0111239 **SS:** 0.0086981
Sample 1	Bed 32	57.90%	7.54%	9.30%	1.39%	2.00%	20.98%	**Qtz:** 0.0070355 **Calcite:** 0.0049861 **SS:** 0.0094427
Sample 1	Bed 32	59.48%	11.88%	7.84%	2.99%	4.44%	11.98%	**Qtz:** 0.0071691 **Calcite:** 0.0043323 **SS:** 0.0060302
Sample 4	Concretion unit	73.82%	12.14%	3.08%	1.98%	2.58%	6.61%	**Qtz:** 0.0103877 **Calcite:** 0.0088455 **SS:** 0.0098124

a)

XRF Data

Sample	Bed	Illite	Koalinite	Montmorillonite	Quartz	Calcite	Pyrite	Goethite	Chlorite	Other
29	Cannon ball	24.12	31.17	5.99	17.7	2.70	4.77	5.03	7.08	1.48
3	Bed 32	25.67	29.92	10.75	15.1	1.63	3.91	5.40	6.22	1.44
22	Bed 32	25.49	30.14	10.83	15.1	3.80	3.04	4.26	5.97	1.43
45	Concretion	25.84	28.10	9.94	17.8	1.16	4.58	5.01	6.19	1.40

b)

Table 4 a) showing the data obtained from the SEM/EDX analysis the different layers analyzed show large differences in TOC. Where Bed 32 shale layer contains up to 20.98% TOC, locally. b) Showing XRF data obtained by Lie A Fat at the TUDelft in 2014. The two data sets combined provide a relative good representation of the bulk rock composition of the different layers.

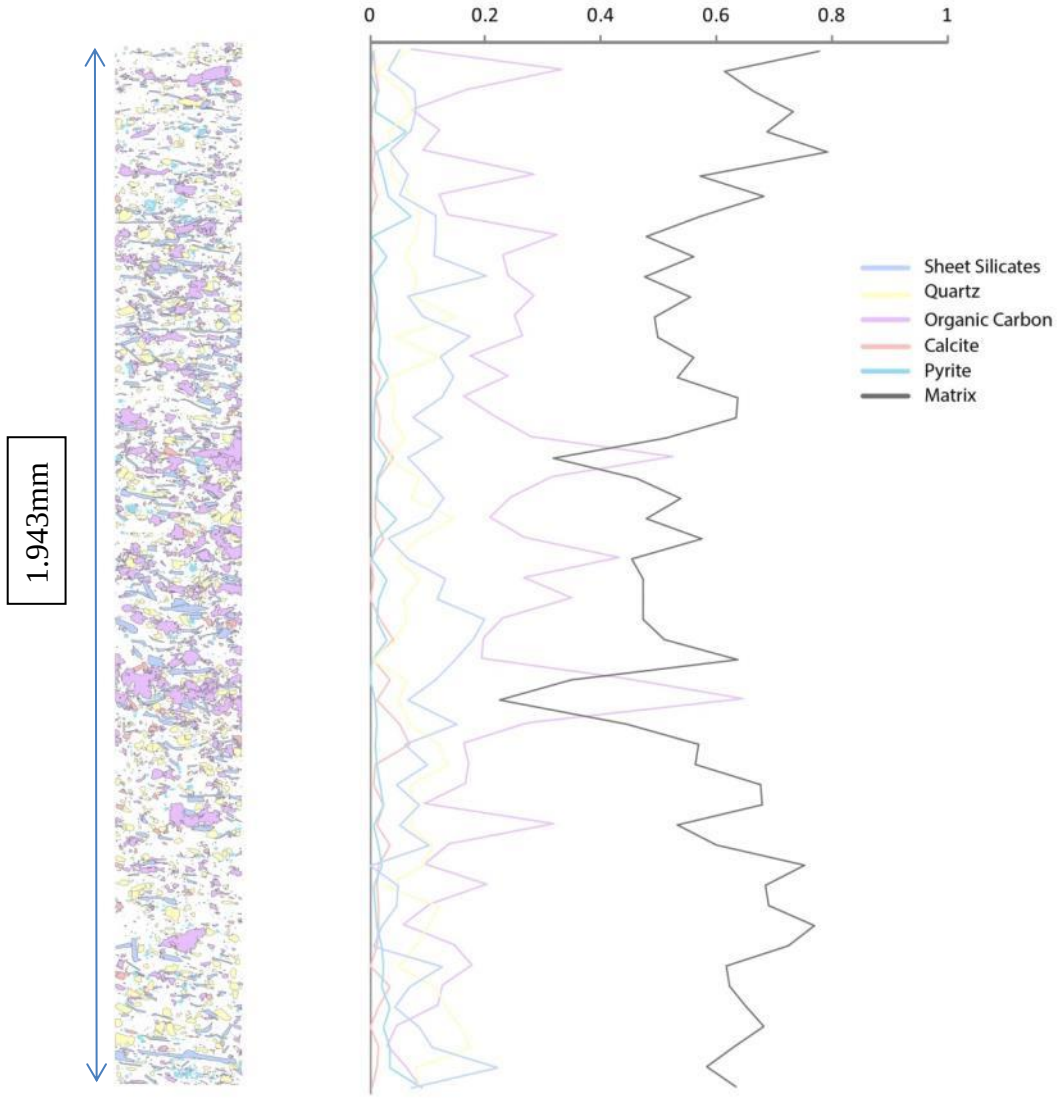

Figure 12: Shows the scan line and the results from the SEM analysis done on the upper part of sample 1. The different type of grains are either interpreted by hand or using grey scale filtering. The white background of the scan line is un-interpreted and is considered to be matrix. The graph on the right shows the relative percentages of the different interpreted minerals and matrix.

4.8. Geomechanics of shales and sample characteristics

The results of the density, porosity and the unconfined pressure test are shown in this paragraph. First the measurements from the Ultrapycnometer and measurements done by hand (using a caliper) are shown in table 5. These measurements are then used as constants in the unconfined pressure test. The results of the unconfined pressure tests are described per sample, starting with sample 4.

The methods described in section 3.9 are used in order to determine the sample matrix density (ρ_m), matrix volume (Vm), total sample Volume (Vt) and the averaged connected porosity of the sample (φ). The results are calculated using excel and are shown in table 5.

Sample #	Bed	Weight (g)	Height (mm)	Diameter (mm)	Bulkvolume (cm^3)	Bulk density (g/cm^3)	Matrixvolume (cm^3)	Matrix density (g/cm^3)	Sample porosity (%)
9	Cannon ball	87.34	43.40	32.17	35.27	2.48	34.12	2.5596	3.26
1	Bed 32 shale	73.13	40.46	30.60	29.76	2.45	28.76	2.5429	3.35
4	Concretion unit	49.13	23.00	33.92	20.79	2.36	20.15	2.4388	3.08

Table 5: Showing the different sample parameters which were measured in order to determine the sample porosity. These parameters are also used in the geomechanical calculations described below. The results are shown in stratigraphic order.

The geomechanics of the different shale samples, acquired from the different pavements present in Port Mulgrave were tested using a unconfined pressure tests. The samples were pushed together until fractured, hence the maximum stress was reached. The graphs shown below illustrate the resulting stress/strain curves (both horizontal and vertical) and means used to acquire the Yield strength and the particular stress range needed in order to derive the average E and v. These ranges are when both the horizontal strain/stress curve and the vertical strain/stress curve can be represented by a straight line. These ranges are 25 to 35 MPa for sample 4, 20 to 27.5 MPa for sample 1 and 12.5 to 20 MPa for sample 9. The Young's modulus is calculated and averaged in between these stress ranges using formula (6) described in section 3.9. Poisson's ratio is also calculated and averaged in between its corresponding stress ranges using formula (7) from section 3.9. The calculated Young's modulus and Poisson's ratio values are shown in table 6. The green line illustrates the Yield stress of the sample, since the resulting stress strain curve (blue line) start to deviate away from the ideal stress/strain curve. After the yield stress is reached, opening mode microfractures start to develop resulting in more strain, both in horizontal as in vertical direction.
The results from the unconfined pressure tests can also be used to derive the brittleness index (B.I.) of the different samples. This index was expressed as a fraction (Jin et al. 2014 & T. Ravenstein 2014) and could therefore be calculated using the following formulas:

$$E_{brittle} = (E - E_{min})/(E_{max} - E_{min}) \qquad (14)$$

$$v_{brittle} = (v - v_{max}) - (v_{min} - v_{max}) \qquad (15)$$

$$B.I. = (E_{brittle} + v_{brittle})/2 \qquad (16)$$

A B.I. higher than approximately 0.4 indicates a prospective rock for hydraulic fracturing (Rickman et al. 2008 & T. Ravenstein 2014). The results from these calculations are shown in table 6. In essence the rock appears to be prospective in terms of hydraulic fracturing since the Poisson's ratio is relatively low and the rock is therefore prone to fail under stress. The results are calculated using the upper and lower limits of E and V which correspond to the entire data set. With the current geomechanical results it is impossible to calculate the fracture toughness K_{ic} and the Fraccability Index (F.I.) since no lab data of the fractures (fracture aperture vs fracture L) is yet derived.

Figure 13 a, b & c) Showing the results unconfined pressure test results from sample 4, 1 and 9 respectively. The horizontal strain vs stress curves are indicated in red. The vertical strain/stress curve is indicated in blue. The ideal stress/strain curve is indicated by the linear black line. The Yield stress is chosen to be the point where the blue line starts to deviate away from the ideal line and is indicated by the green line.

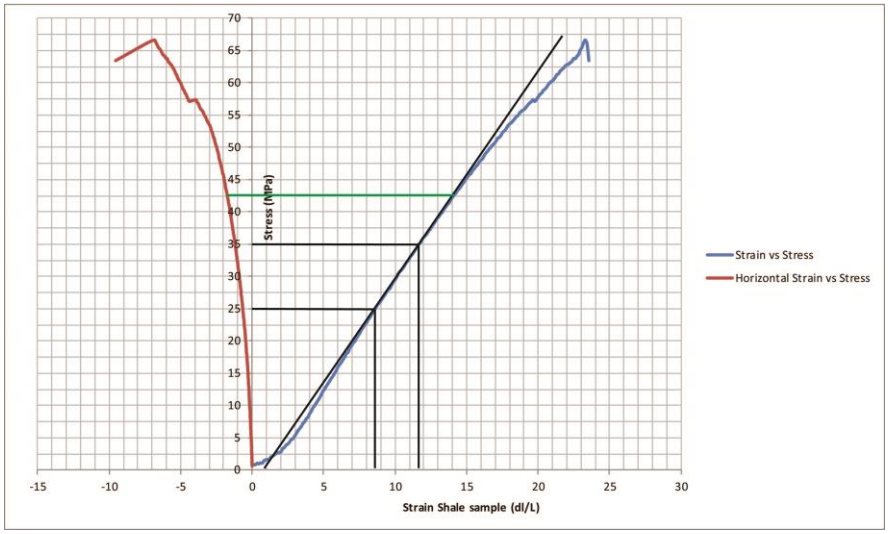

a)

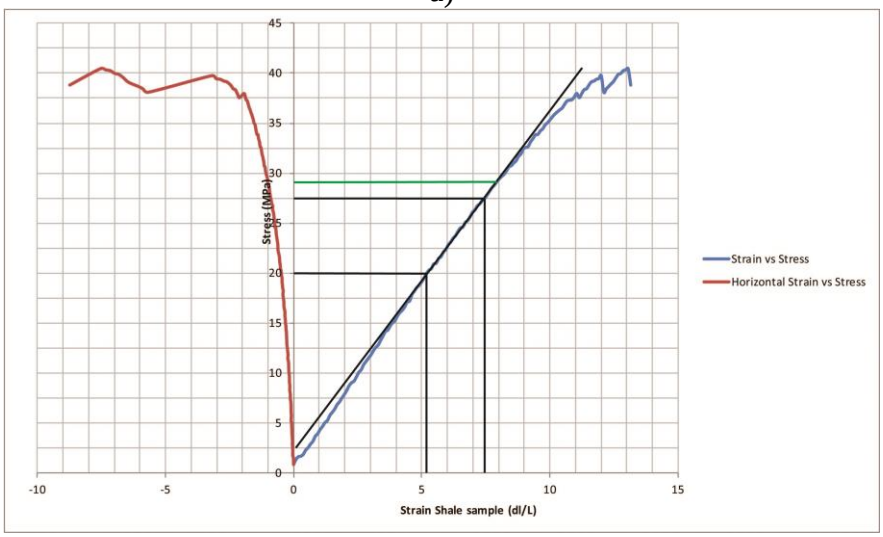

b)

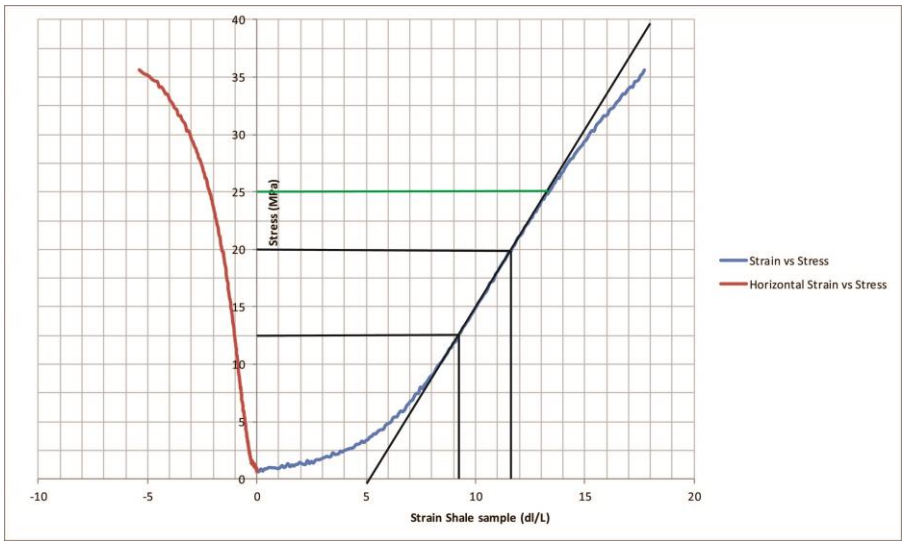

c)

Sample #	Bed	σ_{max} (max stress) (MPa)	Yield stress (C Yield)	Young's modulus (E) (GPa)	Poisson's ratio (v)	E brittle	v brittle	B.I.
9	Cannon ball	38.0	25.0	1.556	0.123	0.147	0.681	0.414
1	Bed 32 shale	40.5	28.5	3.759	0.106	0.068	0.924	0.496
4	Concretion unit	66.0	42.5	2.957	0.090	0.264	0.792	0.528

Table 6) Showing the calculations and results derived the unconfined pressure test.

Overall the geomechanical results indicate that all the samples accommodate strain by fracturing. However these first order results also show that samples 1 and 4 are more prone to fracture than sample 9, having higher Young's moduli and a lower Poisson's ratio. This indicates more brittle behavior of the rock.

5. Interpretation and discussion

In this part of the report the acquired datasets, formulas and figures will be combined and interpreted. These interpretations will then be discussed and compared using the available literature. However, before the data can be correctly interpreted and compared to subsurface data sets, a list of assumptions needs to be taken into account. Therefore this list is presented first and will be referred to during the discussion of the results.

5.1. List of important remarks

Because of its importance the following list needs to be taken into account before we can accurately interpreted and discuss the data present in the results sections:

- Are the fractures created at depth? If yes, what prove can be found in the data
- How can the major sampling biases be taken into account?
- Can the lab data be used in order to interpreted the geometries and structures observed in the field?
- What role plays the varying resolution of the datasets on the results?
- Are some smaller fractures created due to structural unloading or enhanced to due weathering processes?
- Are joints which are present at the surface present in the subsurface?

5.2. The geometry and formation of the fracture network

The fracture network data sets shows an accurate resolution down to the cm scale. However when zooming out to the reservoir scale, some larger fracture zones are also observed. In the results section (4.1.) an orthophoto set was shown which was made using birds eye view drone imagery. Using this photo set these larger fracture zones were interpreted. These zones had a length scale ranging between 10.0 – 70.0m. These zones may therefore play an important role in the permeability of the fracture network at a reservoir scale. Field measurements from vein data and statistical predictions presented in section 4.6. and in the literature suggest that these fractures could have relatively large apertures at depth. Therefore these zones could provide N-S striking pathways for hydrocarbon or hydrothermal fluid migration. These larger zones are also non stratabound which was observed in the field. Therefore these zones may enhance the migration of fluids perpendicular to the bedding, however new field studies are needed to fully prove this point. Spacing of these zones differ per pavement and is therefore not constant. The average spacing is approximately 15m, as can be seen in Figure 4.

In between these fracture zones, parallel striking fractures are also observed. These fractures are called the L1 fracture set. The spacing of these parallel N-S striking fractures differs per layer as was already described in sections 4.1. and 4.2. The L1 fractures are much more closely spaced in domains 1, 2 and 5. Possible causes for the observed differences are layer thickness (Bai et al. 2002), matrix strength, the presence of concretions or the bulk rock strength. These fractures have a length scale ranging between 1.0 to 10.0m. In between the parallel N-S striking fractures, E-W striking orthogonal cross joints are observed. These fractures are called the L2 fracture set. Concerning observation domains 3 and 5 show that these orthogonal L2 fractures are first dominantly observed for fractures which have $l < 1.6$m (see rose diagrams in section 4.2). The representing rose diagrams from the other observation domains (1, 2 and 4) indicate that the orthogonal joints are smaller, becoming dominant for lengths smaller than 0.4m. This perfectly correlates with the average spacing of the N-S striking fractures, since the orthogonal L2 fractures are positioned in between two parallel N-S striking fractures. In between the L2 fractures a new set of smaller roughly N-S striking orthogonal fractures was observed, these fractures are called L3 fractures. This fracture set is more dominant in domains 3 and 5. In all fracture networks the L2 orthogonal fractures often cut off N-S striking L1, L2 fractures which on itself will cut of other orthogonal fractures. The result of these three different fracture sets is an orthogonal or nesting fracture network. However finding relative timing constrains concerning the development of the different fracture sets is hard. However Bai & Pollard 2000 and Bai et al. 2002 stated that orthogonal fracture systems could develop while experiencing one regional stress regime. These authors state that due formation of parallel striking fractures local stress deviations could develop, resulting in the creation of smaller orthogonal fractures. Bai et al. 2002 stated that a critical ratio could be reached depending on stress ratio's and a ratio between fracture spacing and layer thickness. Computer models from the TUDelft 2014 also showed that local stress perturbations could occur in between closely spaced fractures. Apart from abutting constrains other relative timing indicators like curving parallel or curving perpendicular relations indicate that fractures developed simultaneously. Since fracture planes had to act as open free planes in order for these geometries to develop (Fossen 2008, Twiss & Moorse 2006). Figure 14 illustrates a conceptual model which shows how deviations in local stress can result in the development of the observed orthogonal fracture networks.

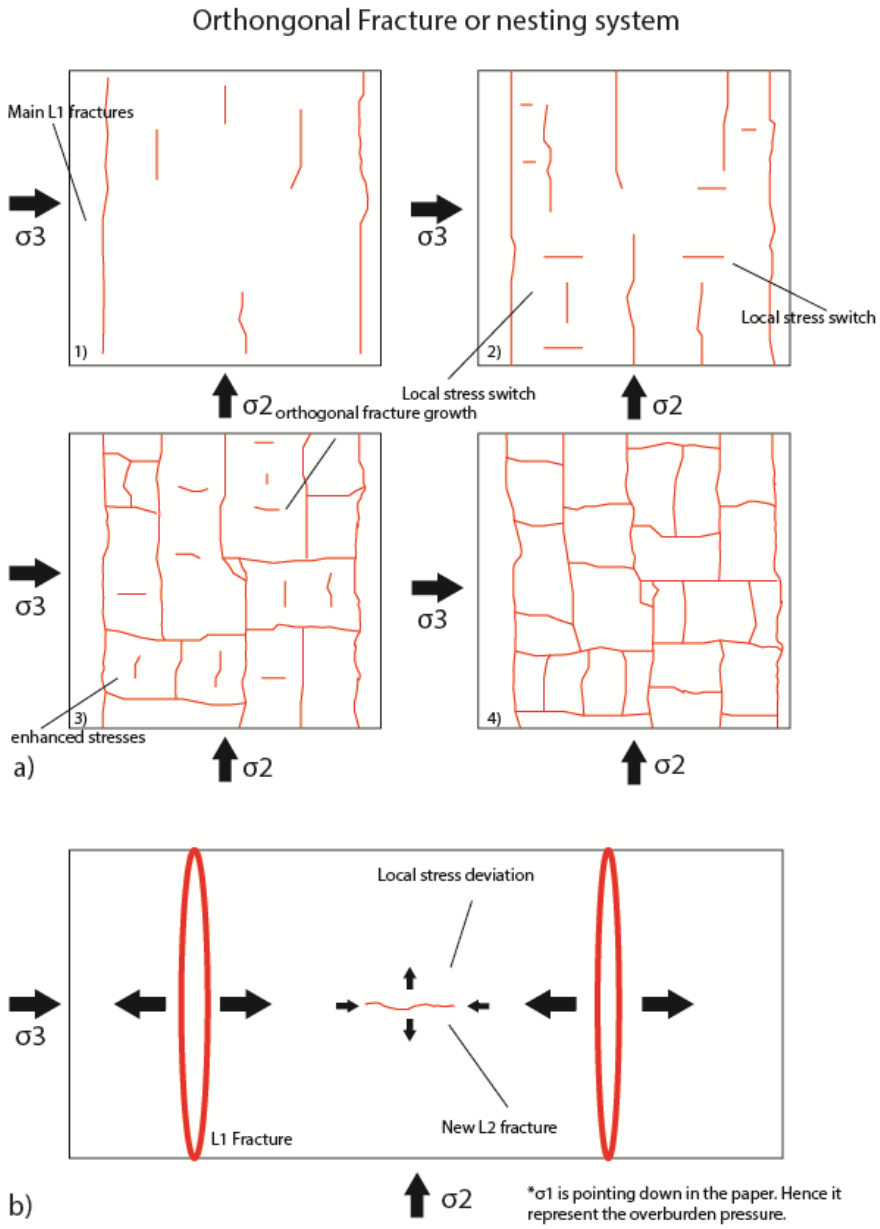

Figure 14 a) Showing a conceptual model which illustrates the development of a nesting or orthogonal fracture network over time (going from 1 → 2 → 3 → 4) under one regional stress regime. The regional stress field is indicated by the arrows, which represents the horizontal stress components σ2 and σ3. In all figures σ1 is pointing down into the paper, representing the overburden pressure. All the fractures drawn are steep dipping into the paper, therefore only the strike of the fracture is drawn. b) Shows how the opening of two closely spaced L1 fractures can result in an local stress switch in the center of the fractures, due to local compression in between those L1 fractures. Hence forming a L2 orthogonal fracture which opens perpendicular to the L1 fractures.

In the cannonball dogger and the concretion unit (observation areas 1,2 and 4) the fracture network also shows a branching geometry. In this network fractures appear the constantly changing direction and then die out against another fracture or for example a concretion. Fractures also appear to split up into two or more fracture, hence the fracture is branching out. Therefore the resulting geometry does not show a pure orthogonal fracture network with N-S striking fractures and smaller E-W striking fractures, but showing smaller fractures

propagating in multiple directions. This was also already shown in section 4.2. Apart from some distortion due these branching effects, the orthogonal network is still the dominant geometry.

Another observation how these three networks differ from the other two fracture networks is how closely spaced the parallel striking L1 fractures are. In this report this spacing is indicated in 2D by the P21 value which is presented in section 4.3. As was illustrated in Figure 14, closely spaced fractures may create local stress perturbation and form orthogonal fractures. This is called the critical spacing ($S_{critical}$) (Bai and Pollard 2000). The critical spacing is however highly dependent on the layer thickness (Bai and Pollard 2000, Bai et al. 2002). These authors state that the critical spacing is defined by the following ratio: S/T_f. The critical ratio for orthogonal fracture to develop is around 1.7 (Bai et al. 2002). Therefore according to this theory a thinner layer can have more closely spaced fractures before this critical ratio is reached. The stratigraphic column shown in section 2.2. indicates that the layer thickness varies, showing that both the Concretion member and the Cannonball dogger are relatively thin layers. Therefore this theory on layer thickness can explain the more closely spaced L1 fractures and shorter (l = +- 0.4m) L2 orthogonal fractures. The Bed 32 Shale and the Top Grey Shale are relatively thicker layers (see section 2.3.). The spacing of the L1 fractures within these layers is therefore much larger, also having coinciding longer L2 orthogonal fractures. Therefore it is possible that this critical spacing theory can account for differences in spacing of the fractures. These L1 spacing differences also indicate that the majority of the L1 fractures are bed confined and that only the larger fracture zones cross cut the different layers observed.

However critical spacing theory cannot account for the branching structures which are also observed. There are three possible causes for these branching effects; the concretions present within the layers, the differences in matrix and/or bulk rock strength and differences in bulk rock composition. Unconfined pressure tests done in the lab (section 4.8.) indicate that there are some differences in the geomechanical characteristics of each layer. Let's first compare the two layers which contain concretions; these two layers show differences in both Young's modulus and Poisson's ratio (Concretion unit: E = 2.957 GPa, v = 0.090, B.I. = 0.528, Cannonball dogger: E = 1.556 GPa, v = 0.123, B.I. = 0.414). These differences indicate that the concretion unit is much more prone to brittle behavior and will therefore produce fractures more easily than the Cannonball dogger layer. This can explain differences in spacing and fracture intensity between the two layers, where the Concretion unit is much more intensely fractured. However the dataset from the Cannonball dogger layer does have some resolution issues due to the presence of sea water. This could also reduce the P21 value of the acquired data set. The fact remains that the acquired fracture networks both contain these branching effects. Unconfined pressure tests done on a sample from the Bed 32 shale (non-concretions unit) result in the following data (E = 3.759 GPa, v = 0.106, B.I. = 0.496). This acquired data also indicate prone to brittle behavior, however no branching effects are observed. Therefore it seems more logical that either the concretions or the bulk rock mineralogy may create these structures. Concretions may become local strong points within a layer, altering its rheology locally. This is also seen in the field with fractures propagating around concretions or abutting against them. However some fractures also appear to just cut through concretions. Another explanation could be differences in bulk rock mineralogy, which shows some differences especially in TOC. However it remains unclear whether these small mineralogical differences could account for the branching effects.

Overall using the acquired data and the interpretations stated above some first order conclusions and relations can be stated: The observed fracture networks all show the same type of orthogonal fracturing, indicating that this network developed under one regional stress regime. The fracture intensity/fracture spacing is largely dominated by the rock strength, layers thickness and presence of concretions. The observed branching effects are most likely caused by the presence of concretions. Moreover using these relations a first order 3D fracture network geometry can be derived and is shown in Figure 15.

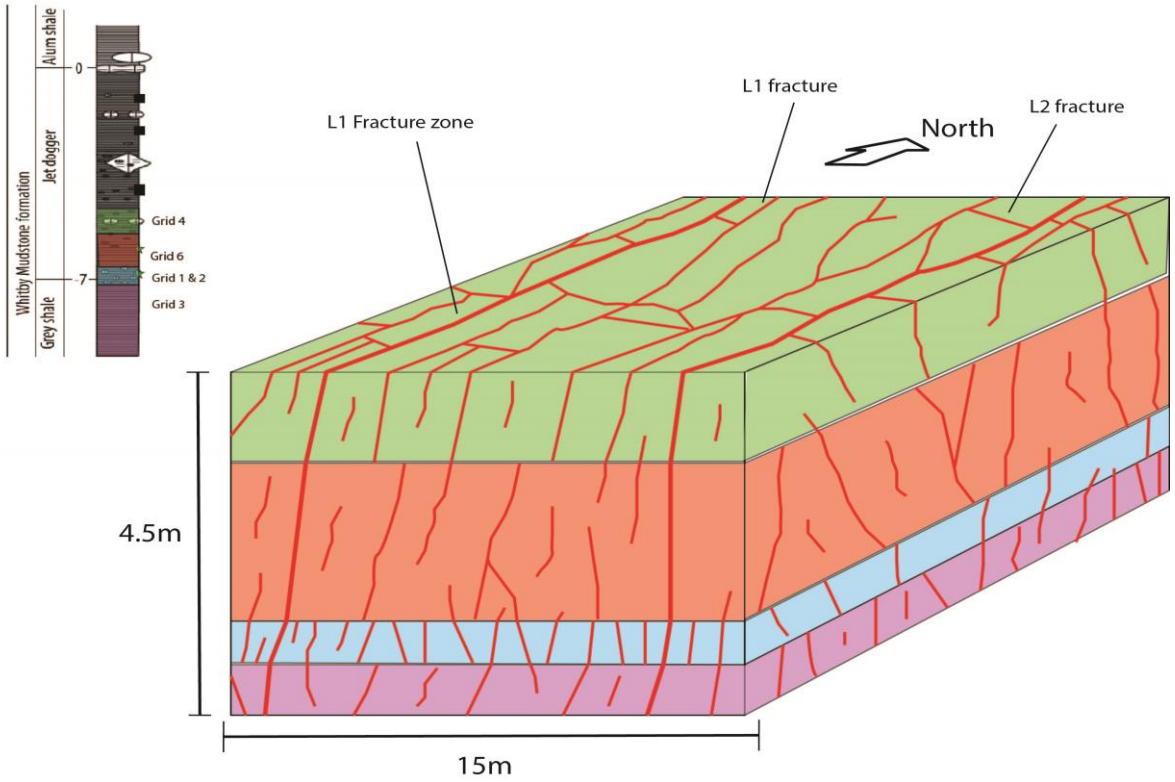

Figure 15: Showing a conceptual 3D fracture network model. This model shows how two large L1 fracture zones cross cut all layering. The model also shows that the majority of the L1, L2 and L3 fractures are bed confined. Fracture intensity also differs per layer which is also shown in the model. This model is based on the digitalized networks, field observation and the interpretations stated in section 5.2.

The model and the digitalized fracture networks from section 4.2. also indicate that the fracture network geometry is very anisotropic with N-S striking fractures being much more frequent, often having lengths longer than 1.0m. The length and dominance of the L2 fractures differs per layer. However these fractures only show dominant behavior at the smallest length scales. Therefore the fracture network permeability appears to be much higher in the N-S direction than in the E-W direction.

5.3. Fracture network statistics and rock characteristics

In this section of the report the different statistical formulas and results are interpreted and discussed. Several different results will be compared with each other and their corresponding rock characteristics. The possible meaning of the acquired result will also be discussed. All the data that is discussed in this section is shown in table 7.

5.3.1. Cumulative length distributions

All the fracture networks show a length distribution which is a combination of an exponential law (smaller fractures) and the power law (fracture length > +-1.0m). The smallest fracture set shows a good fit to an exponential law, however the exponential law does tend to under represent the largest fractures in the system. The power law function tend to over represent the smaller fractures in a system. The exponential law of each data set just represents a best fit law calculated by excel therefore the exact meaning of the different constants is dependent on the data set and are therefore hard to define. The power law exponent does contain valuable information. This can be shown by a computational model done by Bonnet et al. 2001 which is shown in Figure 15.

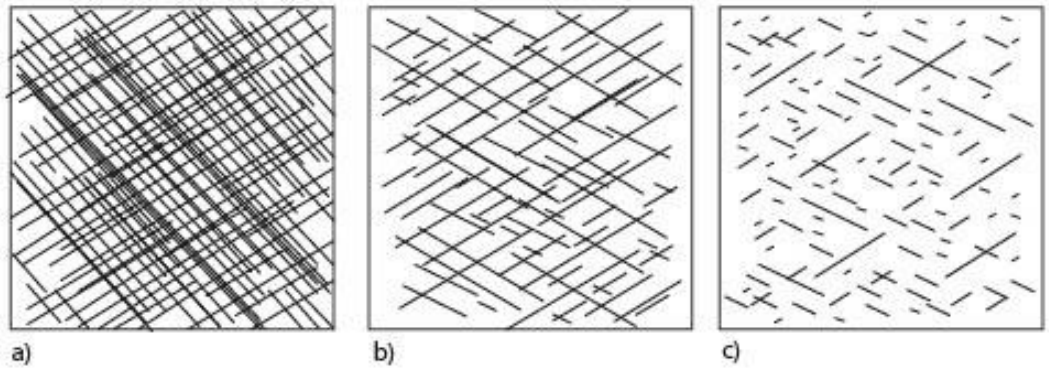

Figure 15: This figure shows computed fracture networks having the same fractal dimension (D = 2) and number of fractures. However the power law exponent (a) differs for each model. a) a = 1.5, b) a = 2.5 c) a = 3.5. Figure after Bonnet et al. 2001.

This model indicates that the power law exponents reflects the number of relatively long fractures present in the system. The data sets acquired from the field also indicate this relation (Table 7). For example the fracture network from the grey shale member shows a high quantity of relatively long fractures, this is also reflected by a power law exponent of 1.53. The same holds for the fracture network from the Bed 32 shale which has a power law exponent of 1.67. The intensely fractured concretion unit contains a relatively high number of small fractures, since the concretions in this layer prevent long fracture propagation. This is represented by their relatively high exponent values (2.836 and 3.508) which also predicts relatively more small fractures. Therefore these acquired values can help predict the length distribution of a fracture network. However the sampling biases stated earlier in the report need to be taken into account. Since the resolution, scale, geometry and degree of weathering was different for each observation domain. However differences in power law exponent can still hold valuable information.

Observation domain	**Bed/layer**	**Fractal Dimension (D)**	**P21 (1/m), REA (m)**	**Exponential law $N(l, L)= Ae^{-c*l}$**	**Power law $N(l, L)= l^{-a}$**	**Sample Porosity (%)**	**Sample B.I.**
4	Cannonball	1.6784	3.00, 5.25	A = 822.14 c = 0.815	a = 2.109	3.26	0.414
5	Bed 32	1.6382	3.25, 5.50	A = - c = -	a = 1.67	3.35	0.496
1	Concretion	1.7495	6.05, 3.25	A = 1434.1 c = 1.378	a = 2.836	3.08	0.528

2	Concretion	1.7112	5.75, 4.00	A = 683.14 c = 0.996	a = 3.508	3.08	0.528
3	Grey Shale	1.6094	4.00, 4.00	A = 264.22 c = 0.662	a = 1.53	-	-

Table 7: Showing a summary of all the acquired statistical rock mechanical data from the results section.

5.3.2. Fracture intensity (P21) and the Fractal dimension (D)

In this section the P21 values, the fractal dimension (D) and representative elementary area (REA) are compared and discussed. These three values show a lot of similarities for all investigated observation areas. But first lest compare the results from table 7. Table 7 shows that the P21 values for the concretion unit are relatively high (5.75 [1/m], 6.05 [1/m]), and that fracture networks in the other layers show lower values. Hence the concretion layer is by far the most intensely fractured. This was also already observed in section 5.2. The REA values indicate the same geometry, again being smaller for the fracture networks in the concretion unit. Therefore these results indicate that the more intensely fractured a layer is, the lower its REA value becomes. Hence the smaller the sampling area has to be in order to capture all the properties of the fracture network. However it should be noted that observation areas 1 and 5 show some resolution issues/biases which could alter (lower P21 value, raise REA value) the acquired results. In the fractal dimension analysis this resolution biases is somewhat excluded. This is done by only choosing parts of the observation domains which showed very good exposure. The results indicate that the concretion unit has the highest fractal dimension. This indicates that this network is more prone to fill all the available space. Which was already observed by high P21 values and closely spaced L1 fractures. The fractal dimension acquired from the Cannonball dogger also shows a relatively high value (1.6784). This relatively high value may be caused by the fact that the low resolution areas which are present in this domain, where excluded from the analysis. The results from the Bed 32 shale layer and the top of the Grey shale show relatively low values, indicating that these networks are less space filling and therefore less intensely fractured. This was already observed by the geometry of the fracture network.

5.3.3. The fracture length vs. fracture aperture relation

The fracture length vs. fracture aperture relation was based on vein length vs vein width data acquired from the produced orthophotos. Due to resolution biases this was only possible on observation domain 1. Therefore it was impossible to apply this relation to the other layers and fracture networks. However large veins were observed in the field, therefore more data can be acquired from the field. This data can then be used to produce a more refined law which applies to the entire Jet Rock Member. However this relatively small data set does show that there is a relation between the length (long axis) and the aperture of such a fracture set. This information is very valuable for fracture network permeability models, since the aperture of a fracture will greatly influence its permeability. Still it should be noted that the acquired law is based on long axis (length) and not the short axis (height) of the fracture, since pavement of the layer was used.

5.4. Application of the data

In order to produce hydrocarbons from tight reservoirs, hydraulic stimulation is needed. Therefore an accurate understanding of the subsurface is preferable, in terms of its BRC, natural fractures and geomechanical characteristics. All the data presented in this report regarding fracture network geometry, fracture network statistics, sample geomechanics, bulk rock chemistry and the data acquired from the field, help in providing a detailed

understanding of the Jet Rock. The Jet Rock acts as an outcrop analogue for several tight reservoirs in the Dutch subsurface. However one can raise the questions: What is the application of all the provided data? Can you use outcrop data in order to make predictions for behavior subsurface rocks? Of course these questions are valid and they should be taken into account. However outcrop analogues are used all the time since subsurface data is limited (Imber et al. 2014). Still, the list of assumptions shown in section 5.1 is very important and should not be forgotten. Outcrop data on fracture networks for instance may leave a misleading impression when being compared to subsurface reservoirs, since exhumation and weathering processes may enhance the number of fractures (Gale et al. 2014). Surface weathering may also result in mineral fill which is not representative to the subsurface and can therefore lead to a misinterpreted data set (Gale et al. 2014). However, apart from these exhumation and weathering problems, natural fractures are common in the subsurface and should be taken into account (Gale et al. 2007).

The samples taken from the field showed that the matrix porosity was very low ($\varphi < 4.0\%$). The matrix permeability was also very low, showing micro-darcy values (Houben et al 2014). SEM analysis done on the same samples however, indicated relatively high TOC values of up to 20% in some samples, indicating a very prospective rock. Imber et al. 2014 also indicated that these rocks produced hydrocarbons in the past, due to the presence of bedding parallel fractures. However these high TOC values are only limited to the Jet Rock (Imber et al. 2014, Powell et al. 2010). The geomechanical data acquired from the samples indicated that all rocks studies are prone to fracture upon stress. Therefore these rocks should be considered to prospective in terms of its fraccability.

The presence of natural fracture networks in the subsurface can either be positive or negative for hydraulic stimulation of tight reservoirs. Hydraulic fractures may abut against a natural fractures. In this case the hydraulic fluid injected into the reservoir may leak away into the open(ed) natural fracture system, preventing new hydraulic fracture growth and propagation (Younes et al. 2011, Gale et al. 2014). However subsurface fractures may also act as planes of weakness and may therefore reopened when being induced to hydraulic stimulation, which may greatly enhance production. Engelder et al. 2009 showed that a joint set similar to the joint set of this study greatly enhanced the production from upper Devonian gas Shales present within the Appalachian Basin. Therefore an accurate understanding of subsurface fracture is needed in order to optimize production from subsurface reservoirs (Gale et al. 2014). The data acquired from the field indicates that the fracture networks tend to be highly anisotropic in terms of its geometry, fracture length and possible fracture aperture. The data also indicates that fracture geometry, fracture intensity and fractal dimension also greatly differs per layer, hence per meter scale. Relative timing relations, the presence of calcite veins and work done by Imber et al. 2014 also indicates that these fracture where most likely formed at depth. Therefore information on such fracture networks can be very valuable. Since in order to optimize production from tight reservoirs, information on the interplay between hydraulic produced fractures and a relative magnitude of the natural fractures is needed (Younes et al. 2011).

Overall it can be concluded that in order to produce hydrocarbon from a tight reservoir an accurate understanding of the subsurface is needed. Outcrop analogues can provide detailed information in terms of BRC, Geomehanical characteristics and natural fracture network characteristics of such reservoirs. However considering the assumption made in this report subsurface data (well bores) is needed in order to better calibrate the results presented in this report.

6. Conclusions

The results, sampling methods and interpretation done during this study are summarized in this section.

- During this study the fracture networks within the Jet Rock Member of the Whitby Mudstone Formation (WMF) was analyzed in great detail. This formation acts as an outcrop analogue for Posidonia Shale Formation (PSF). Data acquisition was done using birds eye pavement imagery, sampling and field measurements.
- The samples acquired from the field indicate that the average porosity is very low ($\varphi <$ 4.0%). Matrix permeability also appears to be very low showing values ranging between 10^{-17} and $10^{-19}m^2$ (Houben et al 2014). However the samples do show relatively high TOC values (up to 20%). Therefore Jet Rock Member could act as an outcrop analogue for shale gas prospects.
- Due to the low porosities and permeability's, fraccing would be needed in order to produce hydrocarbon out of these kind of reservoirs. Therefore an accurate understanding of the rock and its natural fracture network is needed, since natural fractures can greatly alter propagation and geometry of the hydraulic fracture network which is created by hydraulic stimulation.
- The natural fracture networks analyzed during this study show an orthogonal or nesting system. The largest structures observed are large N-S striking fracture zones. These zones are non-strata bound and are therefore found in all pavements analyzed. In between these zones, parallel striking L1 fractures with E-W striking L2 orthogonal in between are observed. The length of these L2 fractures and therefore the spacing of the L1 fractures differs per layers, as was indicated by the rose diagrams from section 4.2.
- Relative timing relations observed in the field and using the digitalized fracture networks indicate that fractures were probably formed during one regional stress regime. L2 orthogonal fractures are most likely formed due a local stress switch in between two closely spaces L1 fractures.
- Statistical analysis, P21 values, REA values and the fractal dimensions indicate that the fracture intensity and spacing greatly differs per layer. Cumulative length distribution analysis indicate that some networks contain a relative higher number of longer fractures as was indicated by the different power law exponent values. Possible explanations for these observations are; the differences in layer thickness, the presence of concretions or the overall rock strength. All these parameters can alter the fracture spacing, fracture intensity and the cumulative length distribution of the analyzed fracture network. These observed differences also indicate that a lot of the observed fractures are probably strata bound.
- Brittleness index (B.I.) values indicate that the analyzed layers are prospective in terms of rock fraccability, since the B.I. has values higher than 0.4. However data acquired from the Cannonball dogger shows less prospective B.I. results.
- The data presented in this report provides an accurate understanding of the Jet Rock Member from the WMF in terms of its fracture network, BRC, geomechanical characteristics and also indicates that these parameters differ per layer. However data is taken from an outcrop analogue, therefore the data and samples could have been altered by exhumation and weathering processes. This indicates that in order to fully calibrate the presented results, subsurface data from the PSF/WMF is needed.

7. Acknowledgements

I would like to thank dr. M.E. Houben and dr. N.J. Hardebol for reviewing my work and creating analysis programs in order to acquire the results. I would like thank Prof. dr. M. Drury for reviewing my work and supporting me throughout the research. I would like to thank dr. A. Barnhoorn and the Technical staff from the Geosciences department of the TUDelft for helping me with the Geomechanical tests. I would like to thank the technical staff from the department of Earth Sciences of the UU for preparing the Thin sections used in this report. I would like to thank my fellow Msc student Robin Dik for helping me with my fieldwork.

8. References

A likely universal model of fracture scaling and its consequence for crustal hydromechanics . (2010). *Journal of Geophysical Research Vol. 115, B10411*.

Aydin, A. (2014). Failure modes of shales and their implications for natural and man-made fracture assemblages. *AAPG Bulletin, V98, No. 11*, 2391-2409.

Bai, T., & Pollard, D. (2000). Closely spaced fractures in layered rocks: initiation mechanism and progation kinematics. *Journal of Structural Geology, 22*, 1409-1425.

Bai, T., Maerten, L., Gross, M., & Aydin, A. (2002). Orthogonal cross joints: do they imply stress rotation? *Journal of Structural Geology, 24*, 77-88.

Bonnet, E., Bour, O., Odling, N., Davy, P., Main, I., Cowie, P., et al. (2001). Scaling of fracture systems in geological media. *Reviews of Geophysics, 29, 3*, 347-383.

Bour , O., & Davy, P. (1998). On the connectivity of three-dimensional fault networks . *Water Resources Research Vol 32, No. 10*, 2611-2622.

Bour, O., & Davy, P. (1997). Connectivity of random fault networks following a power law fault length distribution. *Water Resources Research, Vol 33, No 7* , 1567-1583.

Bour, O., Davy, P., & Darcel, C. (2002). A statistical scaling model for fracture network geometry, with validation on multiscale mapping of joint network (Hornelen Basin, Norway). *Journal of Geophysical Research, Vol 107, No. B6 2113*.

Energie Beheer Nederland (EBN). (2014). Focus on Dutch Oil and Gas. *EBN*.

Engelder, T., Lash, G., & Uzcatehui, R. (2009). Joint sets that enhance production from Middle and Upper Devonian gas shales of the Appalachian Basin. *AAPG Bulletin, V. 93, No. 7*, 857-889.

Fossen , H. (2008). Structural Geology. *Cambridge University Press*.

Gale, J., Laubach, S., Olson, J., Eichhubl, P., & Fall, A. (2014). Natural fractures in shale: A review and new observations. *AAPG Bulletin, V98, No. 11*, 2165-2216.

Gale, J., Reed, R., & Holder, J. (2007). Natural fractures in the Barnett Shale and their importance for hydraulic fracture treatmens. *AAPG Bulletin, V91, No. 4*, 603-622.

Ghadeer, S., & Macquaker, J. (2012). The role of event beds in the preservation of organic carbon in fine-grained sediments: Analyses of the sedimentological processes operating during deposition of the Whitby Mudstone Formation (Toarcian, Lower Jurassic) preserved in northeast England . *Marine and Petroleum Geology*, 309-320.

Hardebol, N., & Bertotti, G. (2013). DigiFract: A software and data model implementation for flexible acquisition and processing of fracture data from outcrops. *Computers & Geosciences 54*, 326-336.

Houben, M., Barnhoorn, A., Drury, M., Peach, C., & Spiers, C. (2014). Microstructural Investigation of the Whitby Mudstone (UK) As an Analog for Posidonia Shale. *76 th EAGE Conference and Exhibition* .

Imber, J., Armstrong, H., Clancy, S., Daniels, S., Herringshaw, L., McCaffrey, K., et al. (2014). Natural Fractures in a UK Shale Reservoir Analogue, Cleveland Basin, Northeast England. *AAPG Bulletin V98, No. 11*, 1-27.

Jin, X., Shah, S., Roegiers, J., & Zhang, B. (2014). Fracability Evaluation in Shale Reservoirs - An Intergrated Petrophysics and Geomechanics Approach. *SPE Paper, SPE Hydraulic Fracturing Technology Confernce* .

Kemp, S., Merriman, J., & Bouch, J. (2010). Clay mineral reaction-progress - The maturity and burial history of the Lias Group of England and Wales. *Britisch Geological Survey*.

Klimezak, C., Schultz, R., Parashar, R., & Reeves, D. (2010). Cubic law with aperture-length correlation: implications for network scale fluid flow. *Hydrogeology Journal*.

Lie-A-Fat, J. (2014). Microstructural, Petrophysical and Anisotropy Analysis of a Posidonia Shale Analogue. *Msc Thesis TUDelft* , 0-59.

Mauldon , M., & Dershowitz, W. (2000). A Multi-Dimensional System of Fracture Abundace Measures. *Geological Society of America Annual Meeting* .

Mempes, R., & Hillis, R. (1996). Determining apparent exhumation from Chalk outcrop samples, Cleveland Basin/East Midlands Shelf. *Geol. Mag. 133 (6)*, 751-762.

Odling, N., Gillespie, P., Bourgine, B., Castaing, C., Chiles, J., Christensen, N., et al. (1999). Variations in fracture system geometry and their implications for fluid flow in hydrocarbon reservoirs . *Petroleum Geoscienses* , 373-384.

Olson, J. (2003). Sublinear scaling of fracture aperture versus length: An exception or the rule? *Journal of geophysiscal research, vol. 108*, 2413.

Powell , J. (2010). Jurassic sedimentation in the Cleveland Basin: a review. *Proceedings of the Yorkshire Geological Society, v58*, 21-72.

Ravestein, T. (2014). Fraccability determination of a Posidonia Shale Formation analogue through geomechanical experiments and micro-CT fracture propagation analysis. *Msc Thesis TUDelft*, 0-52.

Rawnsley, K., Rives, T., & Petit, J. (1992). Joint development in peturbed stress fields near faults. *Journal of Structural Geology, Vol 14, No 8/9*, 939-951.

Rickman, R., Mullen, M., Petre, E., Grieser, B., & Kundert, D. (2008). A Practical Use of Shale Petrophysics for Stimulation Design Optimalization: All Shale Plays Are Not Clones of the Barnett Shale. *SPE Paper, SPE Annual Technical Conference and Exhibition*.

Ten Veen, J., Verreussel, R., Ventra, D., & Zijp, M. (2014). Sweet Spot Indentification and Smart Development - An Integrated Reservoir Characterization Study of a Posidonia Shale Outcrop Analogue. *76 th EAGE Conference & Exhibition* .

Trabucho-Alexandre, J., Dirkx, R., Veld, H., Klaver, G., & de Boer, P. (2012). Toarcian black shales in the Dutch Central Graben: Record of energetic, variable depositional conditions during an oceanic anoxic event. *Journal of Sedimentary Research*, 104-120.

Twiss, R., & Moores, E. (2006). Structural Geology. *Freeman*.

Vermilye, J., & Scholz, C. (1995). Relation between vein length and aperture . *Journal of Structural Geology, Vol 17, No 3*, 423-434.

Younes, A., Moore, H., Suurmeyer, N., Shmidt, P., & Sandstorm, M. (2011). Development of mechanically layered Haynesville-Bosier shale gas play. *Search and Discovery Article* .

Zijp, M. (2012). Schaliegas in Nederland. *TNO*.

Zijp, M. (2013). Shale Gas Formations in the Netherlands. *TNO*.

9. Appendixes

In this section of the report the list of appendix will be shown. This will be done in the following order:

- Appendix 1.1: EDX analysis done using SEM microscope (JEOL JCM 600).
- Appendix 1.2: BRC plots made using Matlab and Excel as was explained in section 4.7.
- Appendix 2: Sample preparation and the unconfined pressure tests.
- Appendix 3: Results from the boxcounting analysis done using Matlab.
- Appendix 4: Showing the cumulative length distribution plots for domains 2, 3 and 4.
- Appendix 5: Showing the workflow for fracture network interpretation and the produced orthophotos

Appendix 1.1: EDX Analysis

Point analysis sample 1

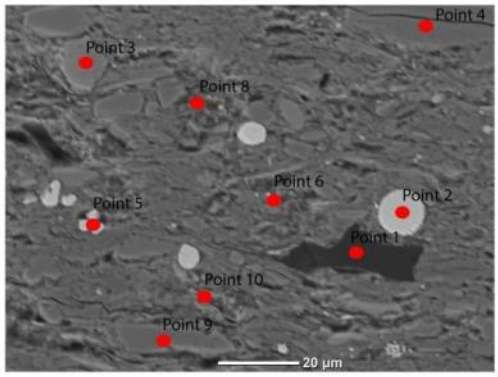

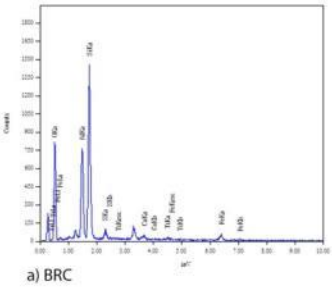

a) BRC

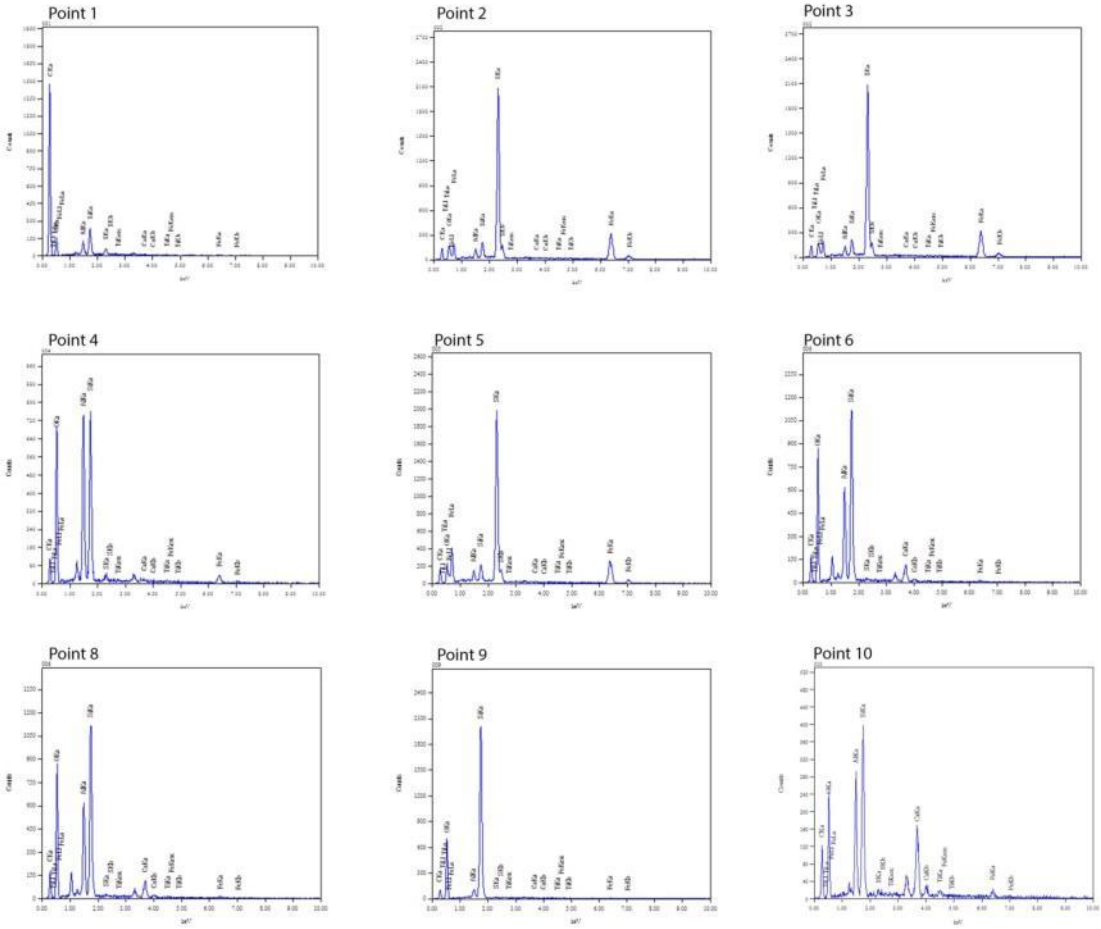

Sample 1, Photo 009

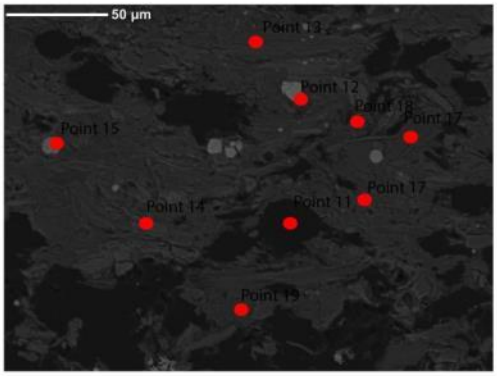

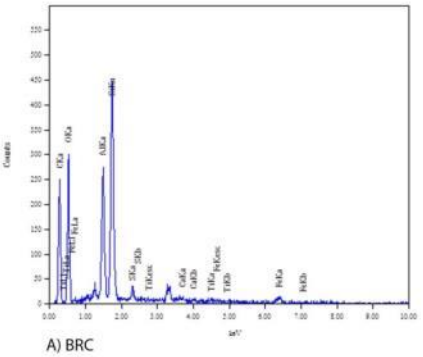

A) BRC

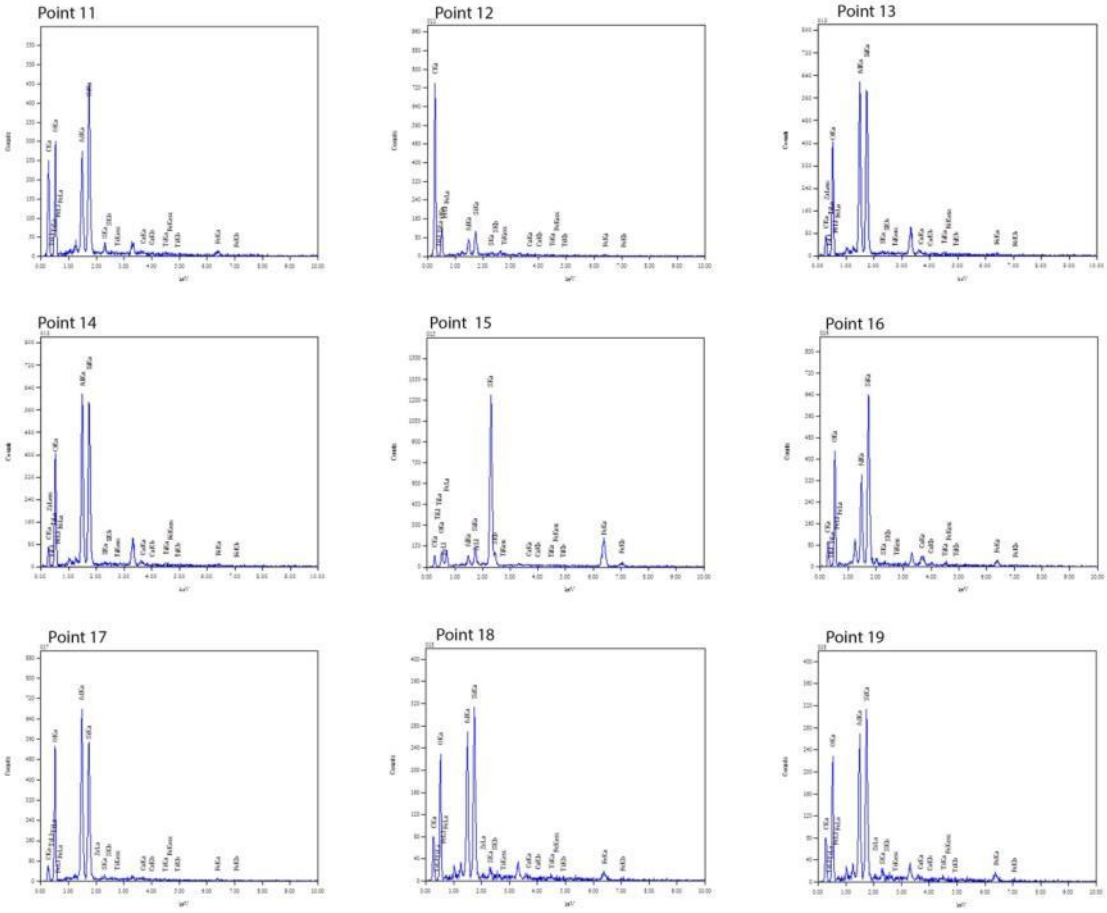

Sample 1, Photo 019

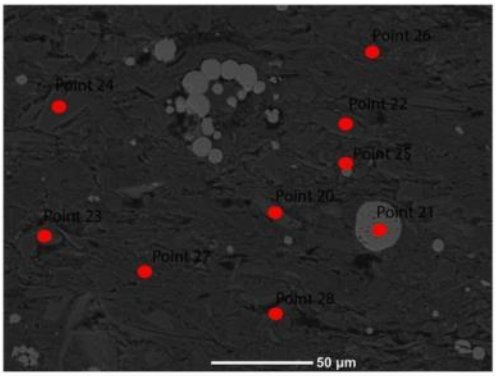

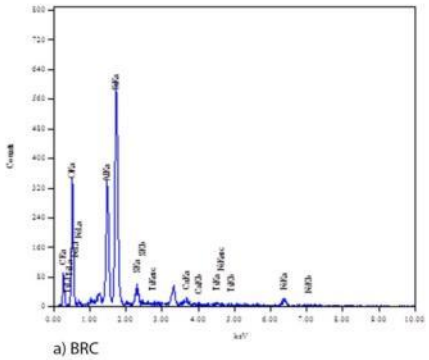

a) BRC

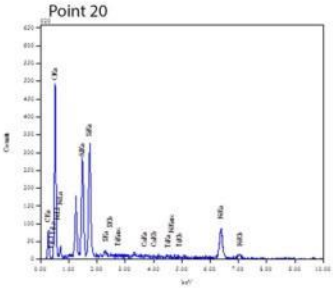

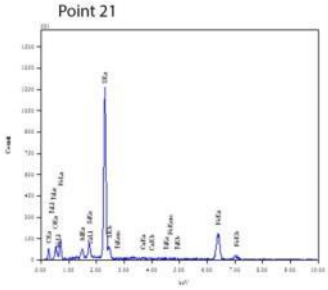

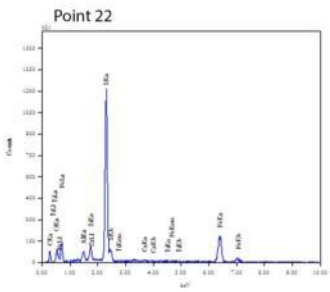

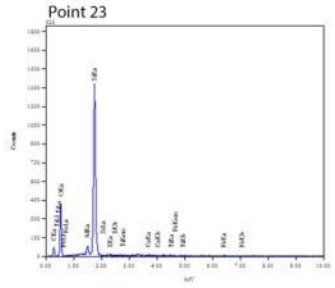

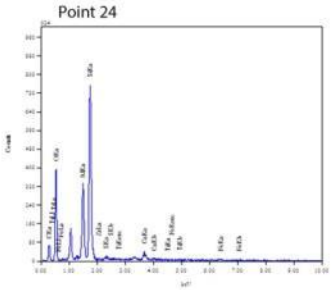

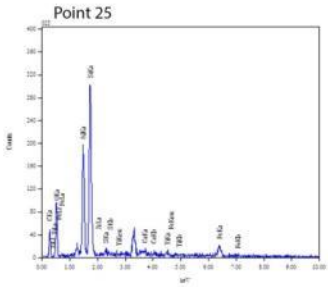

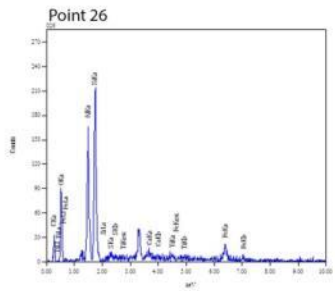

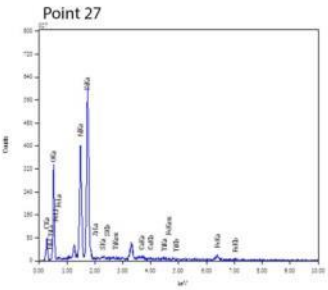

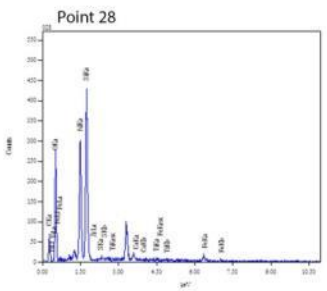

Sample 1, Photo 45

Point analysis sample 4

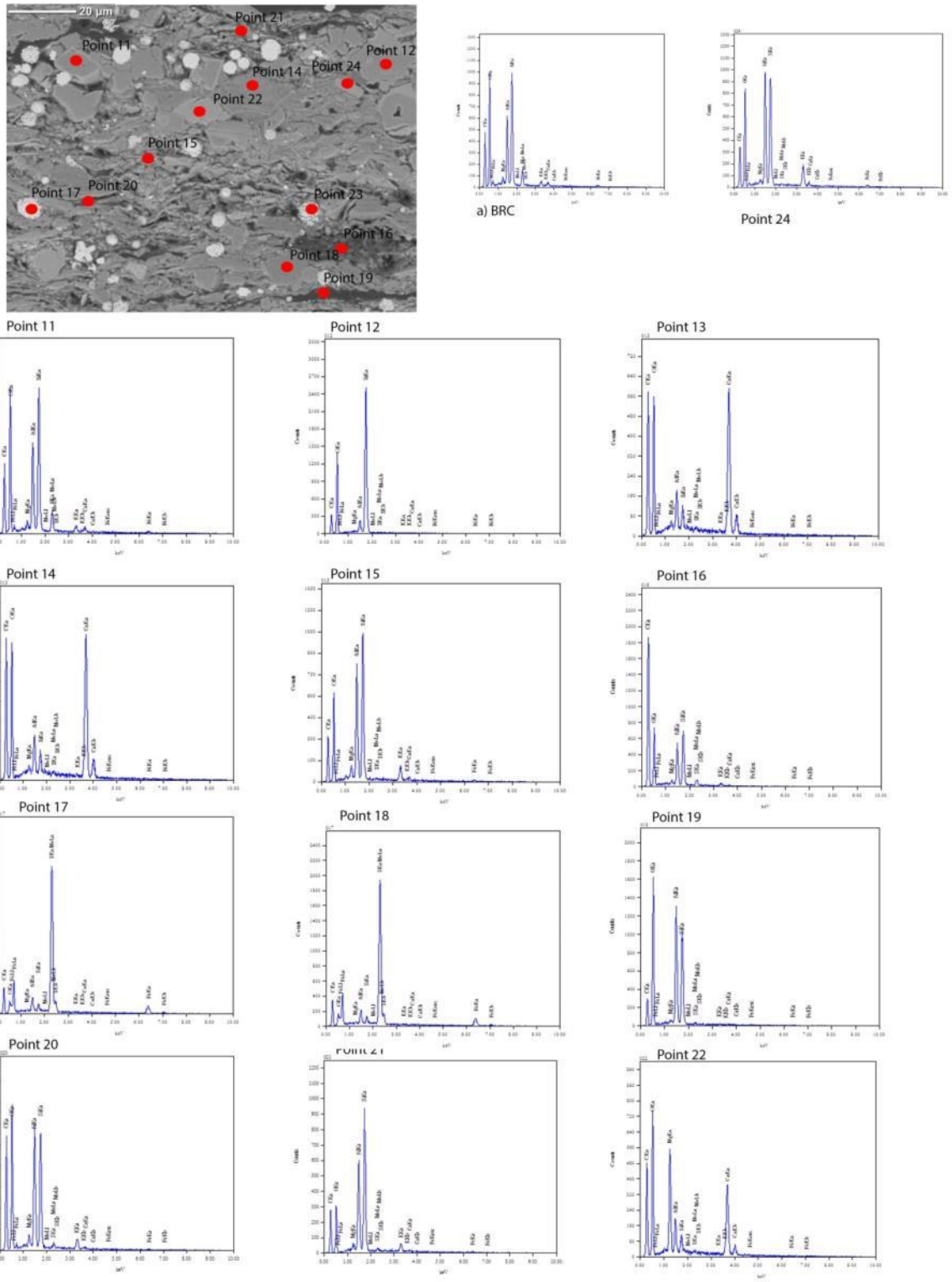

Sample 4, Photo 182

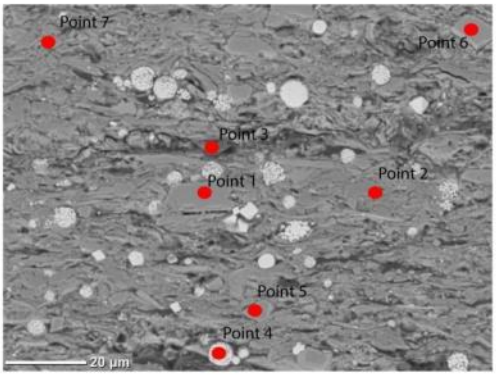

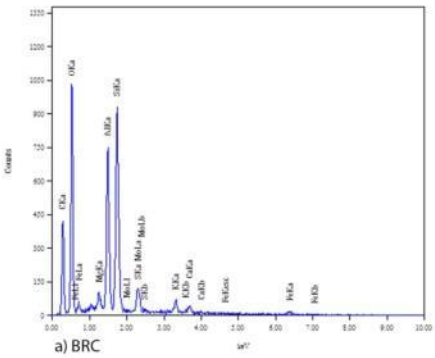

a) BRC

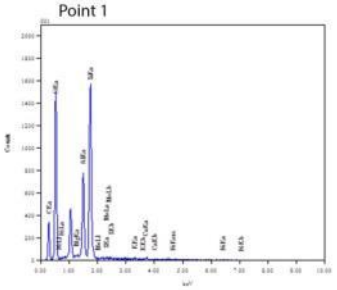

Point 1

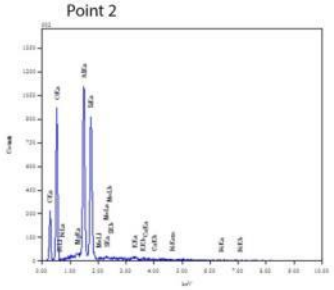

Point 2

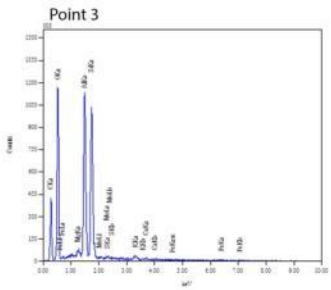

Point 3

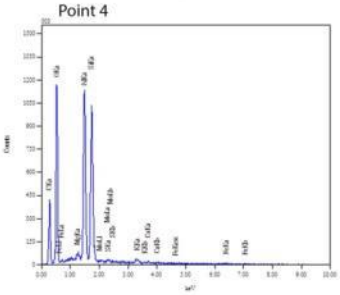

Point 4

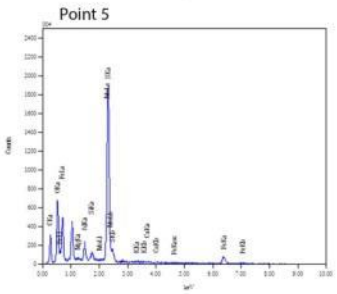

Point 5

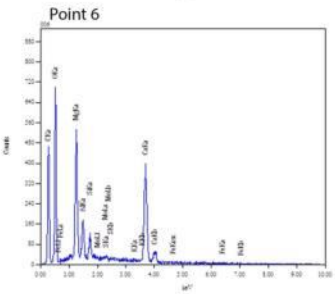

Point 6

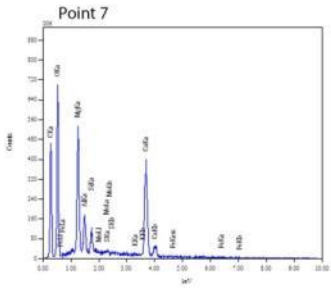

Point 7

Sample 4, Photo 192

Point analysis sample 7

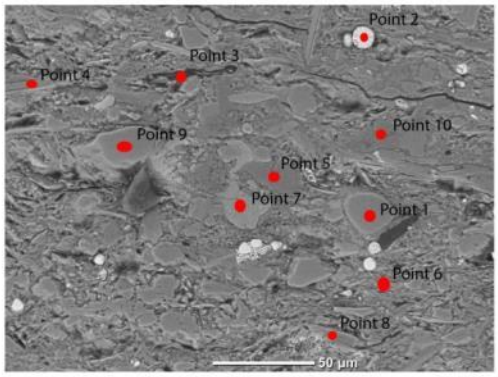

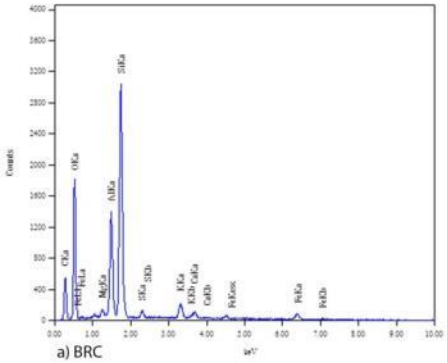

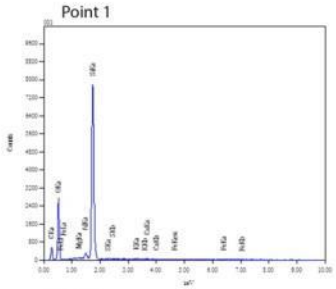

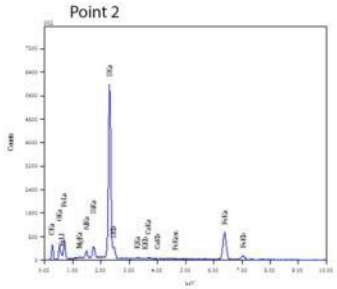

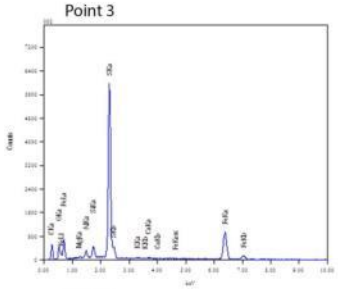

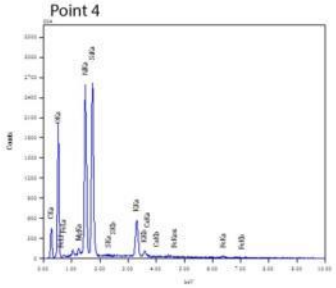

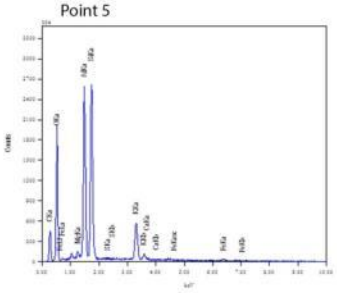

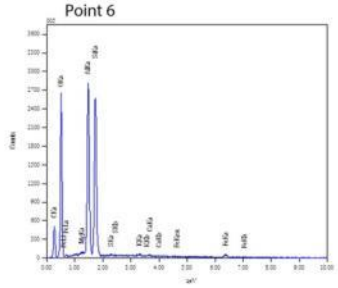

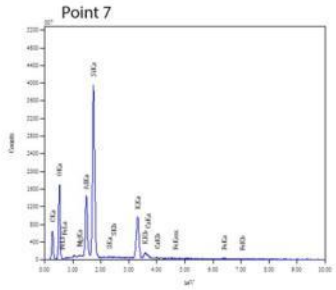

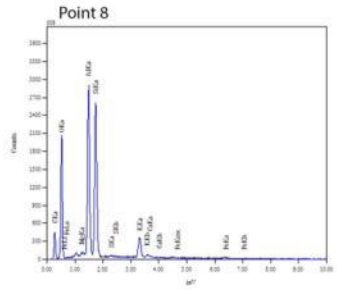

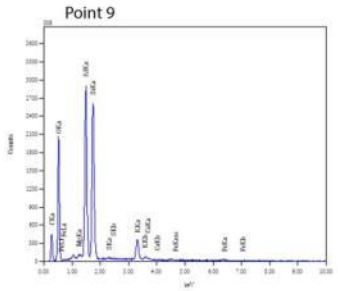

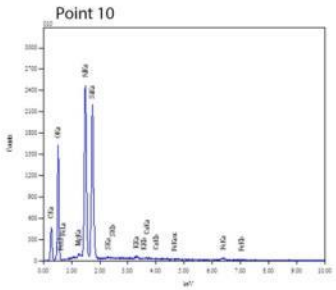

Sample 7, Photo 10

Element Map Sample 1

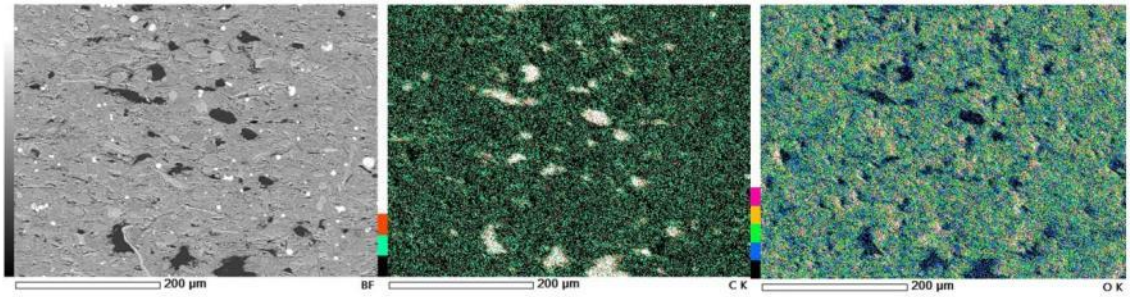

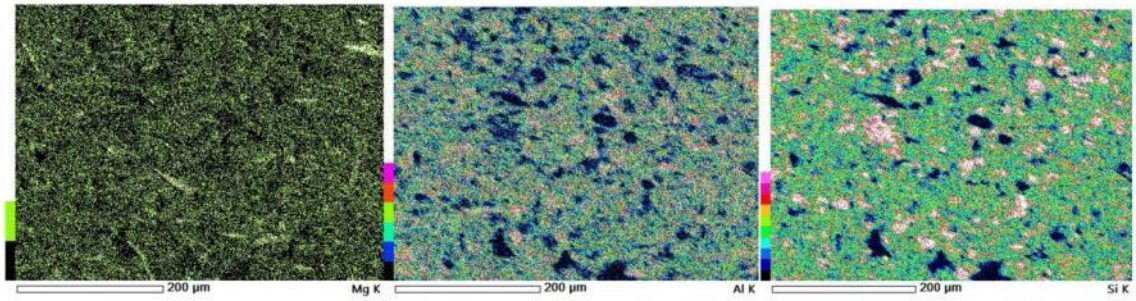

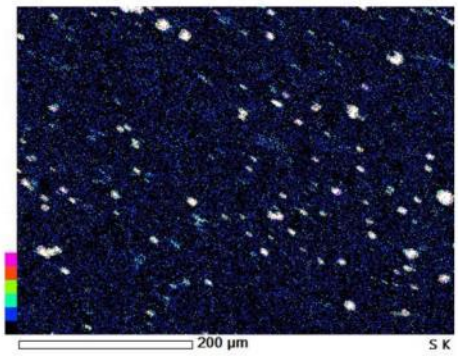

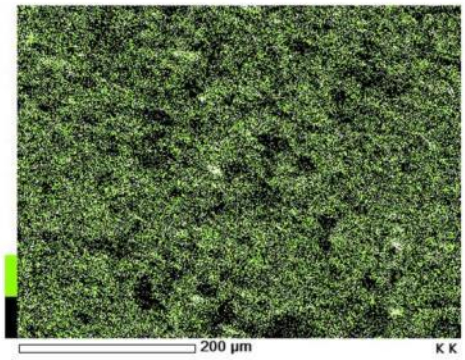

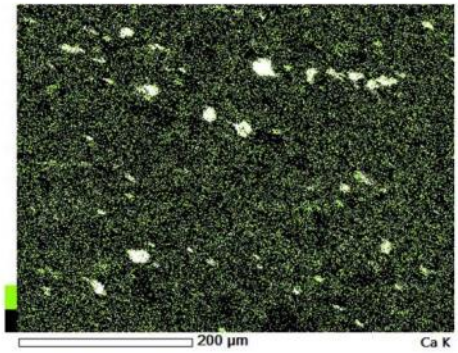

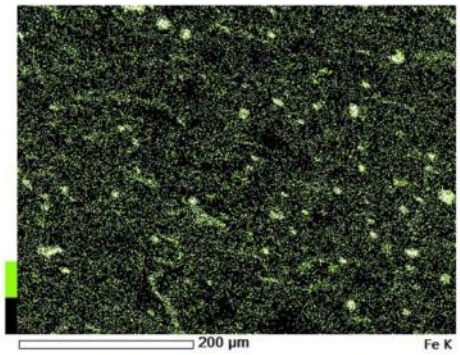

Element Map Sample 4

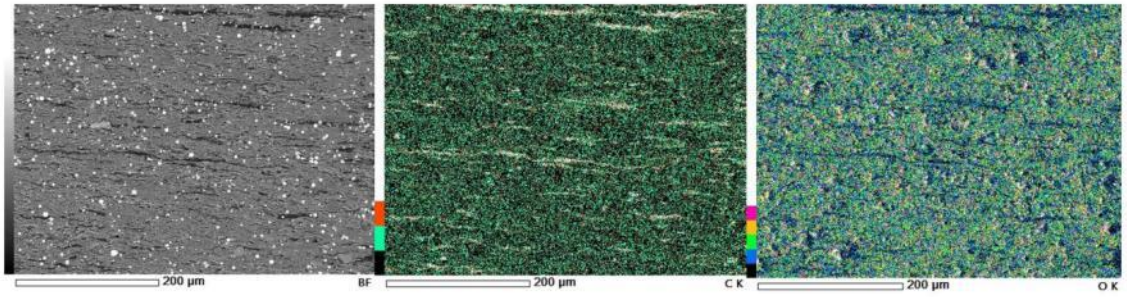

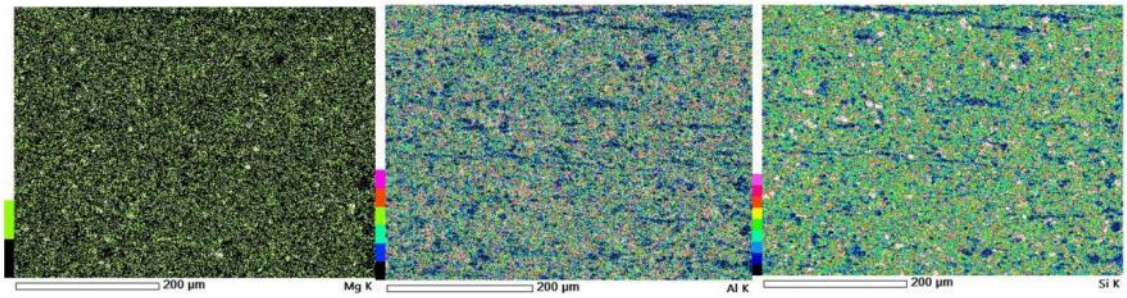

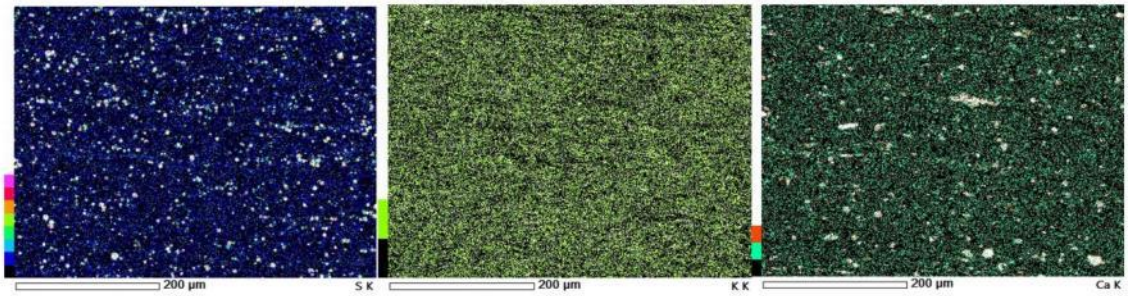

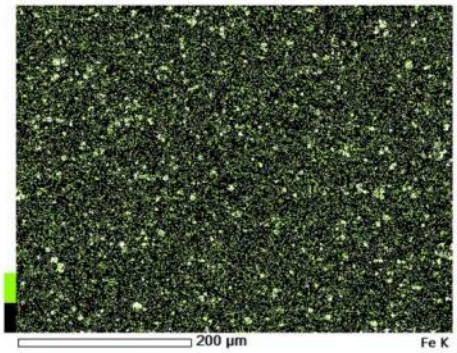

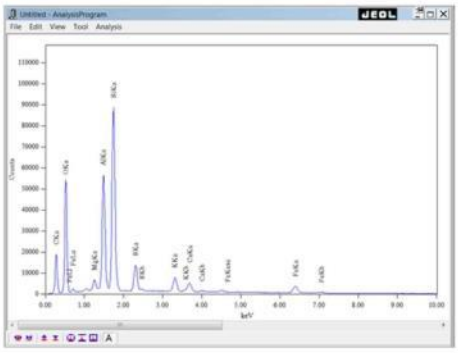

Element Map Sample 7

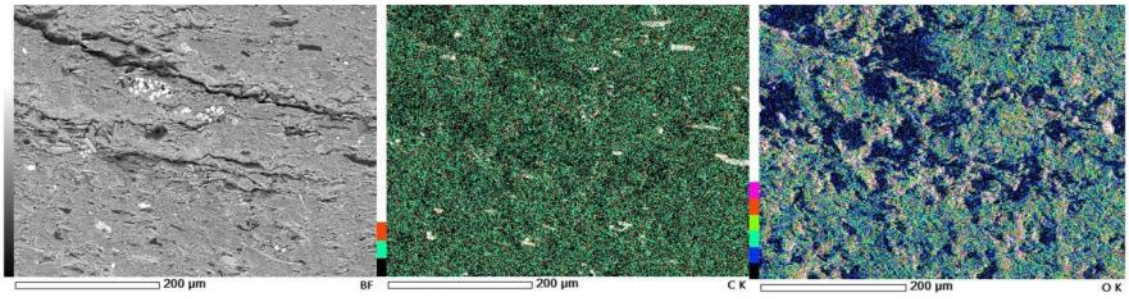

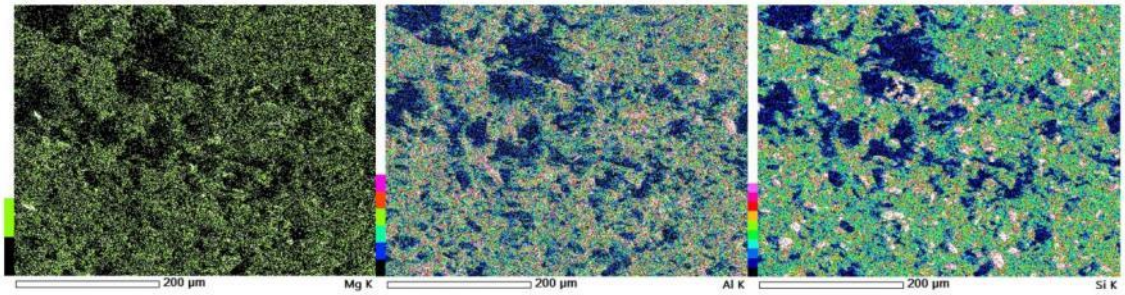

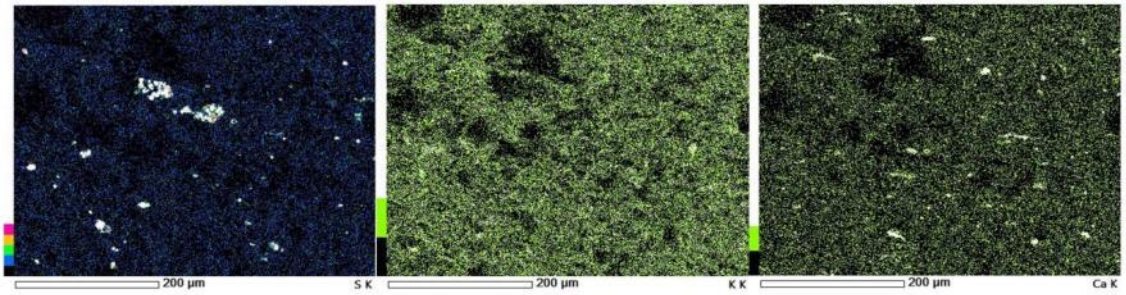

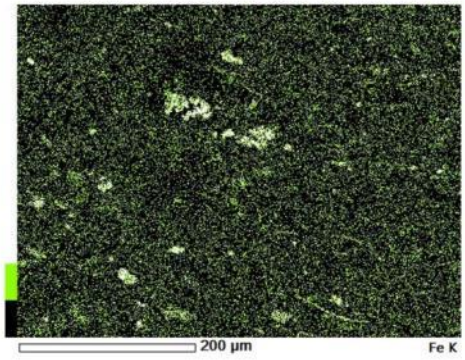

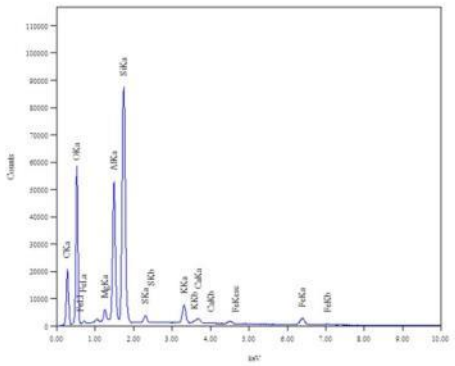

Appendix 1.2: BRC analysis

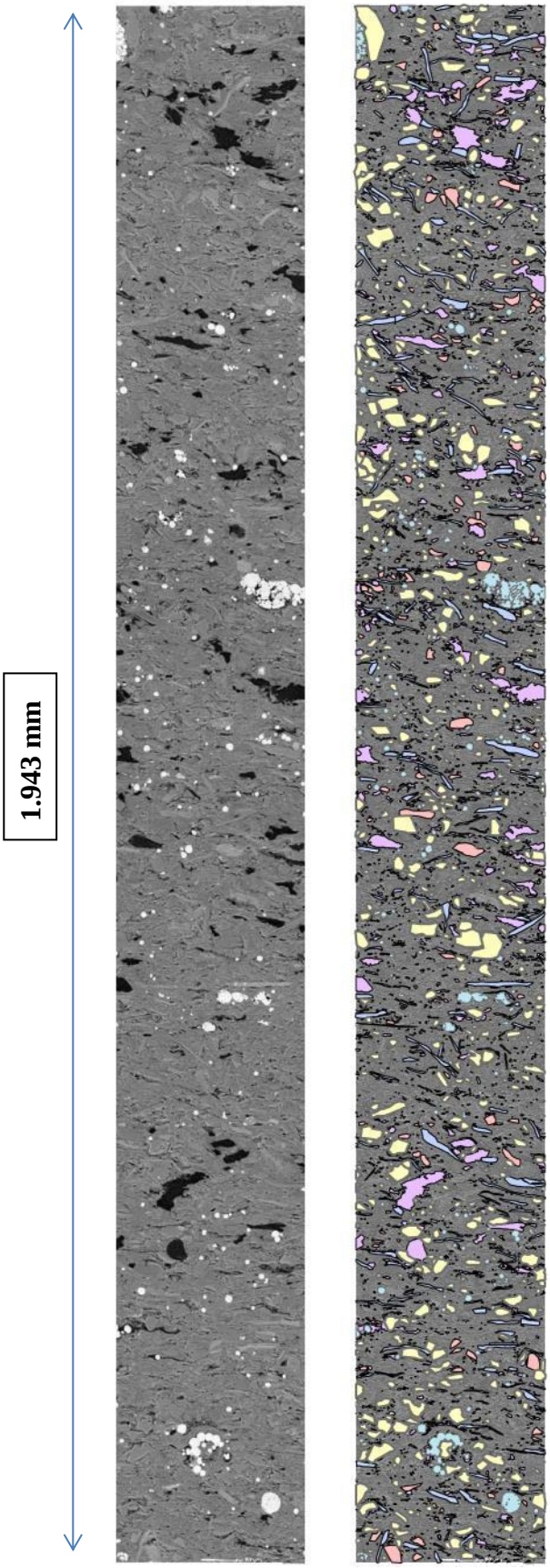

Appendix 1.2.1: Showing the scanline of sample 1-11. Scanline on the left shows and un interpreted scanline. Scanline on the right the same scanline after interpretation. This same method is used for all scanlines. Interpretations where made using ArcMap and using grey scale separation via ImageJ.

Appendix 1.2.2.: Interpreted Scanline of sample 1-11

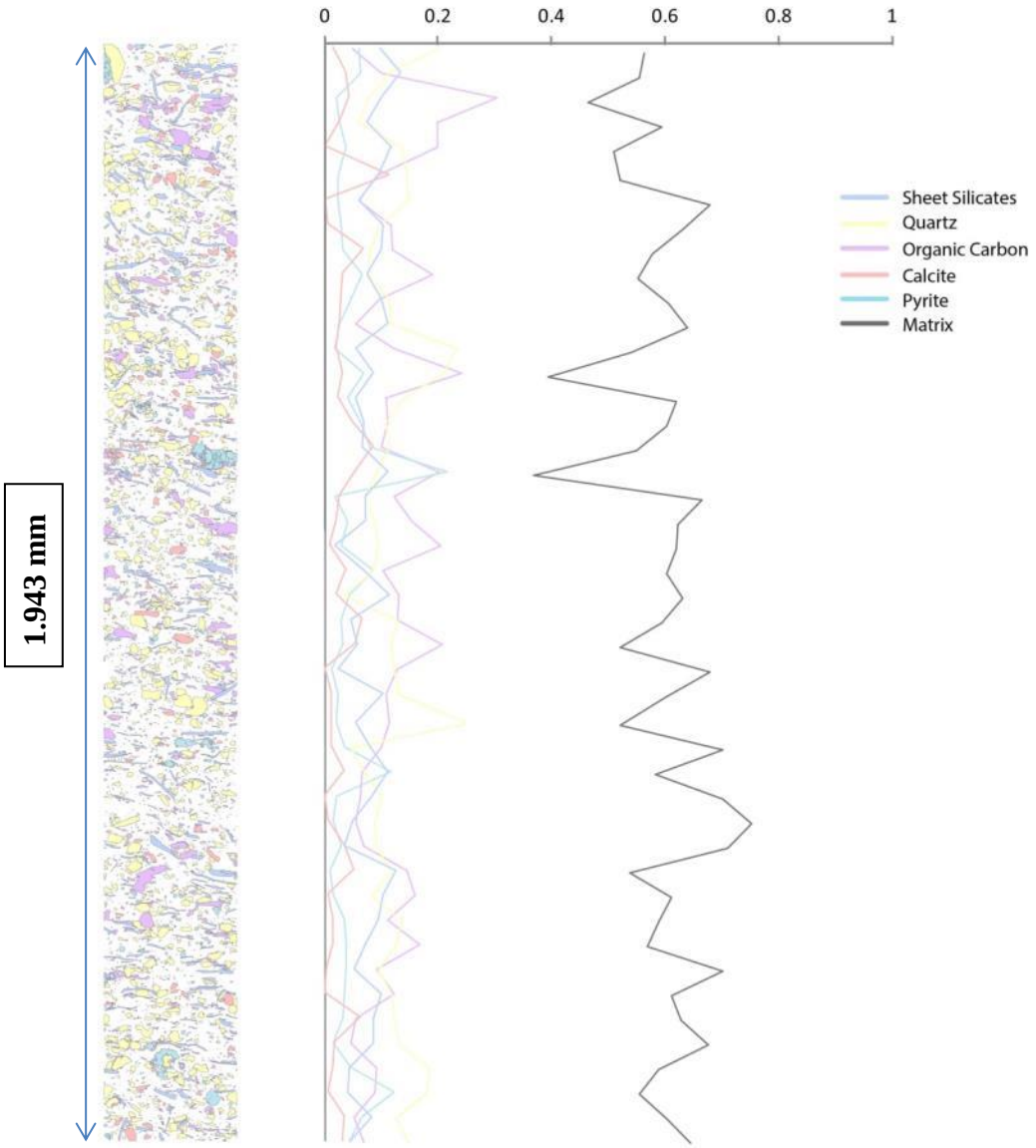

Appendix 1.2.3.: Interpreted scanline from sample 4

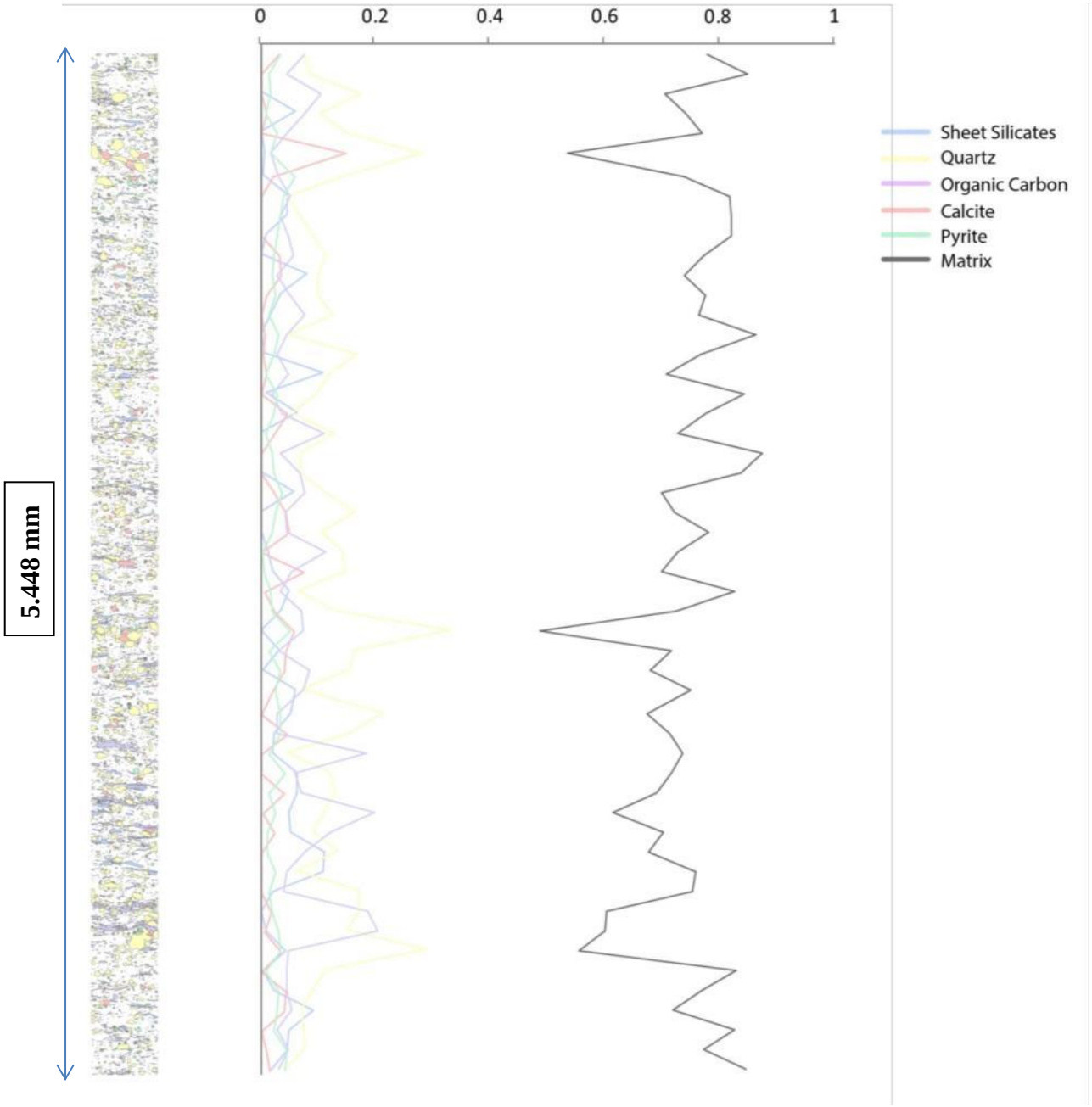

Appendix 1.2.4. Interpreted scanline from sample 7

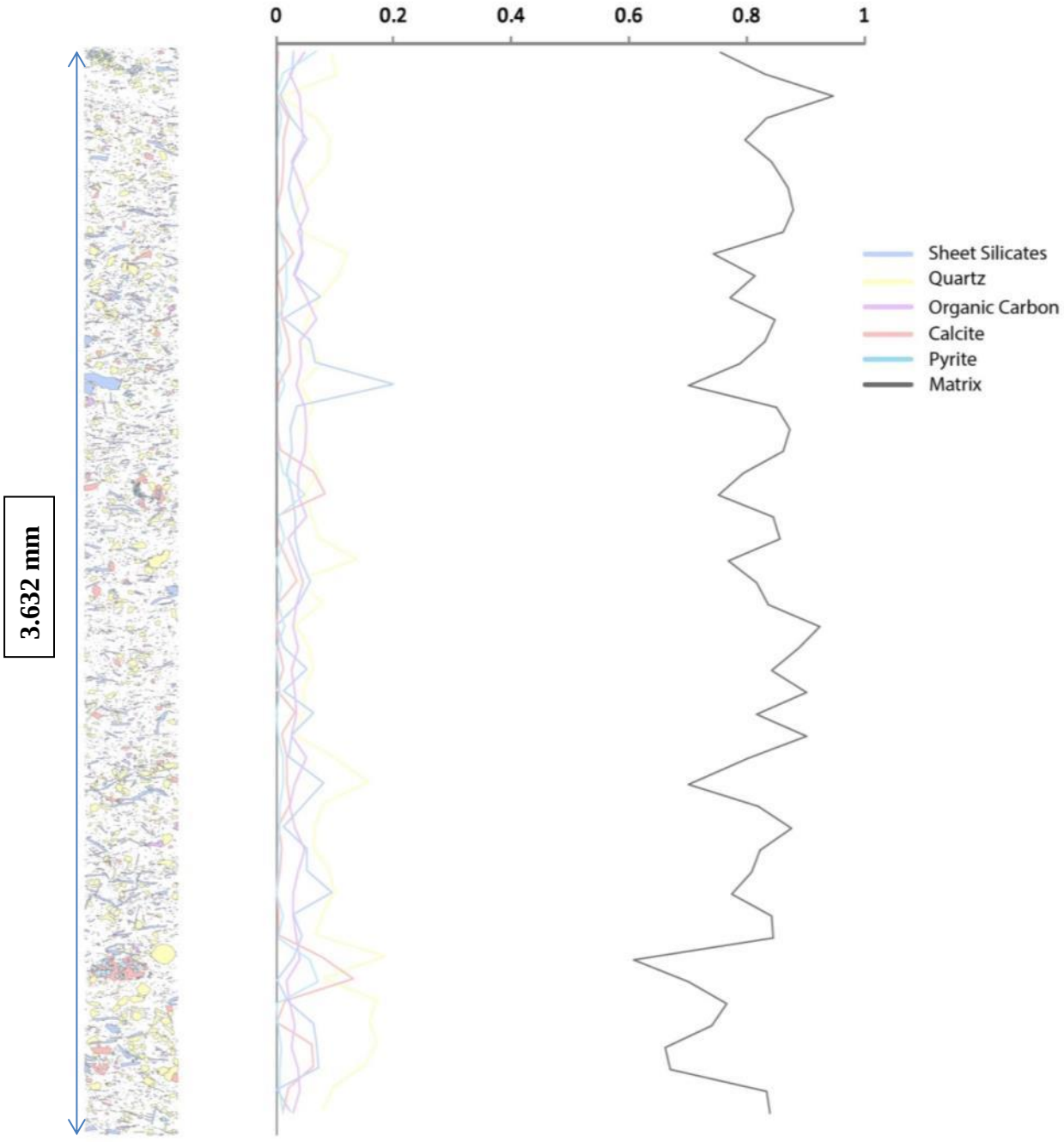

Appendix 2: Sample preparation and the Unconfined pressure apparatus

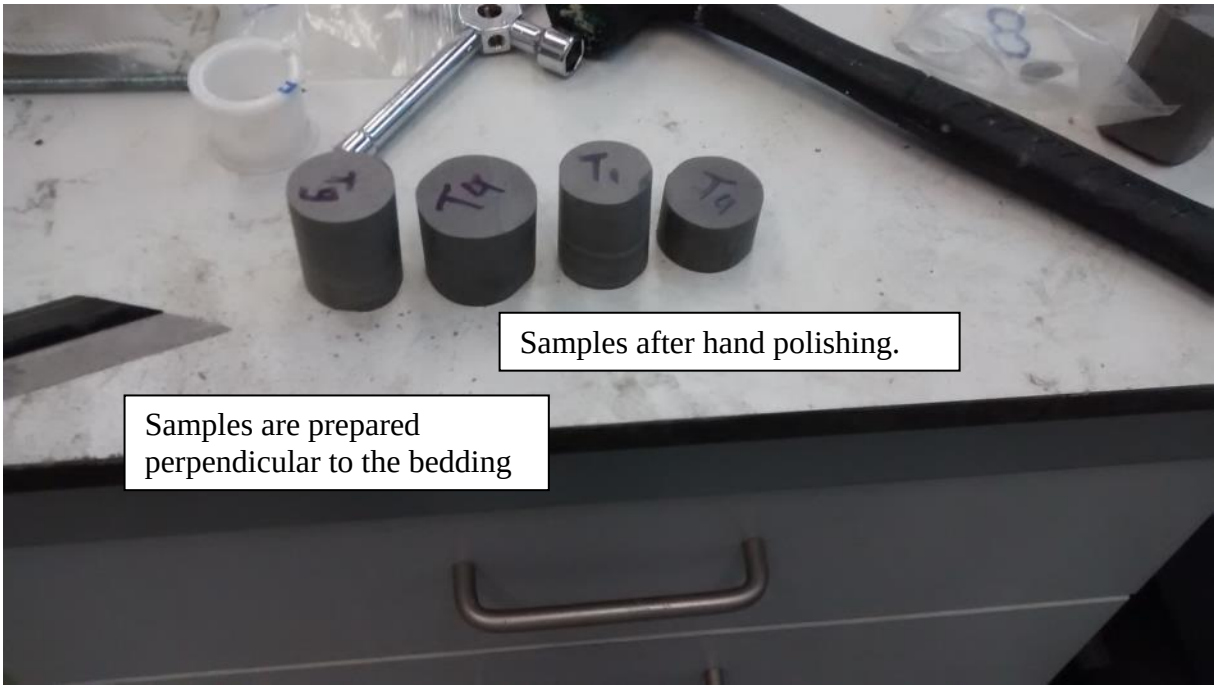

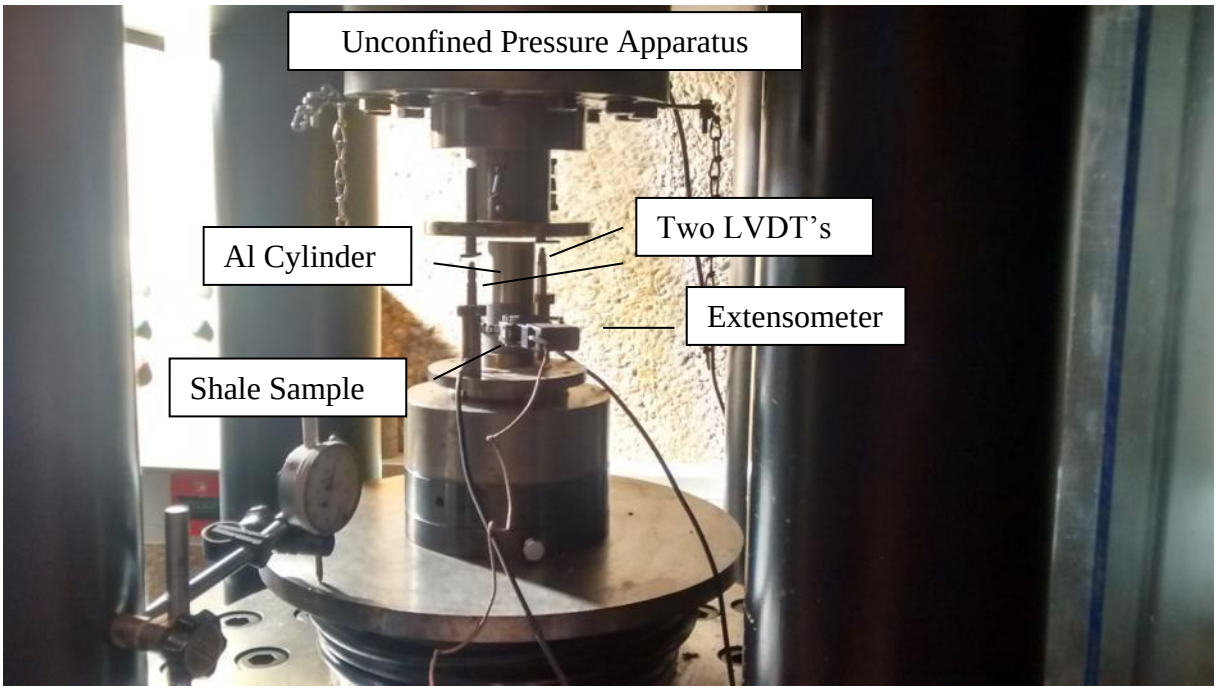

Appendix 3: Boxcounting Results

Observation domain 2

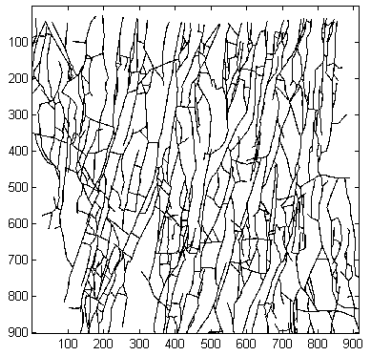

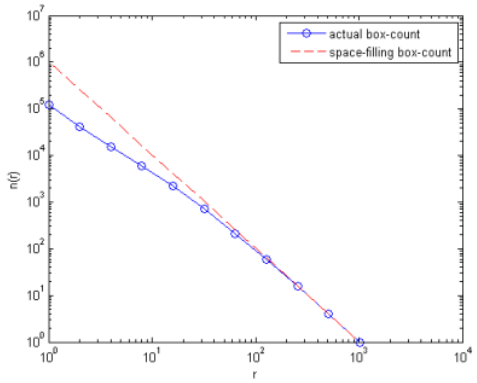

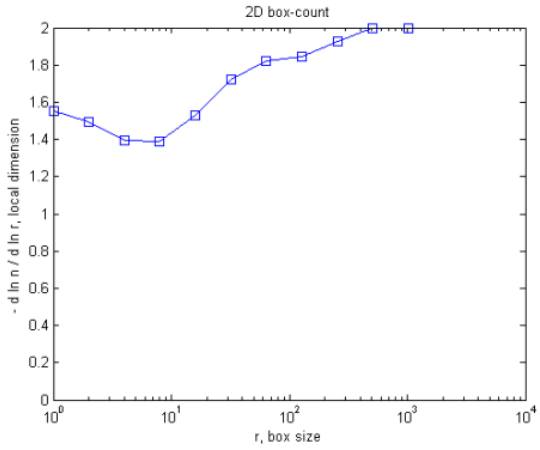

Showing the boxcounting results from observation domain 2. After integrating the slope curve, the average fractal dimension of this fracture network is: 1.7112.

Observation domain 3

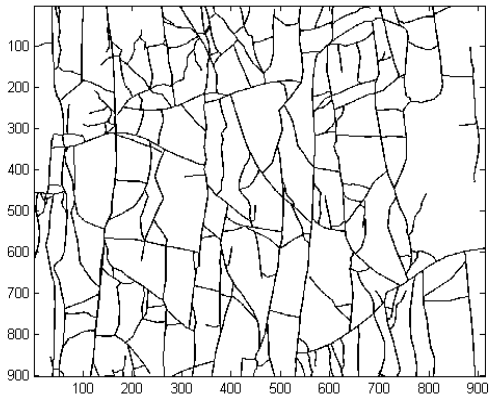

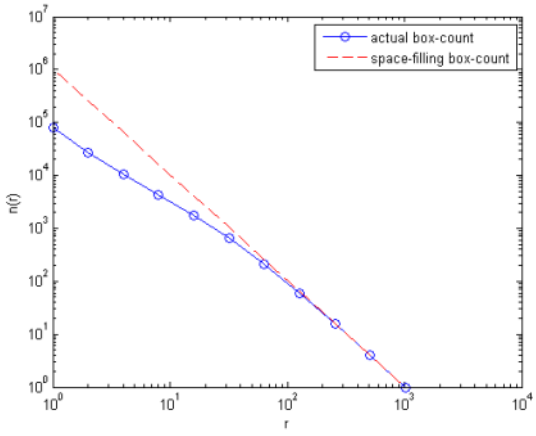

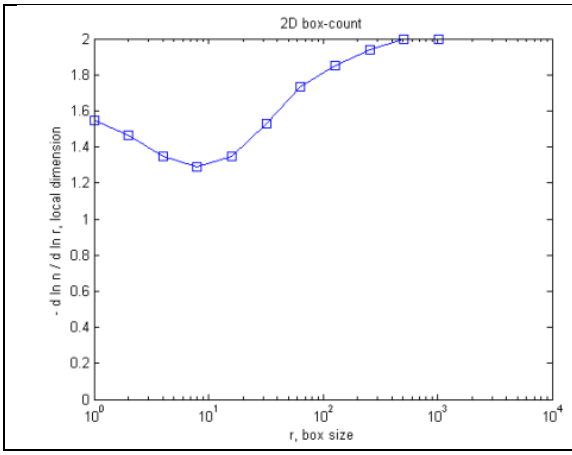	Showing the boxcounting results from observation domain 3. After integrating the slope curve, the average fractal dimension of this fracture network is: 1.6094.

Observation domain 4

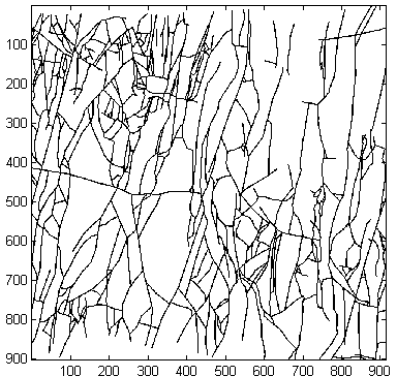	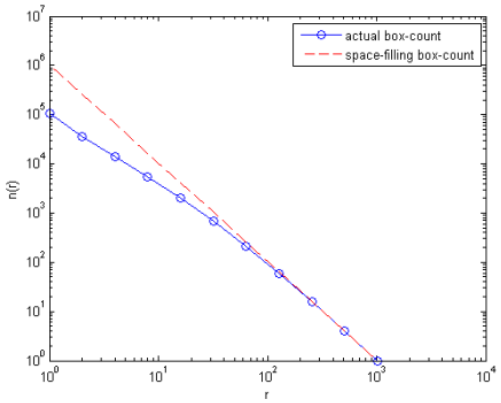
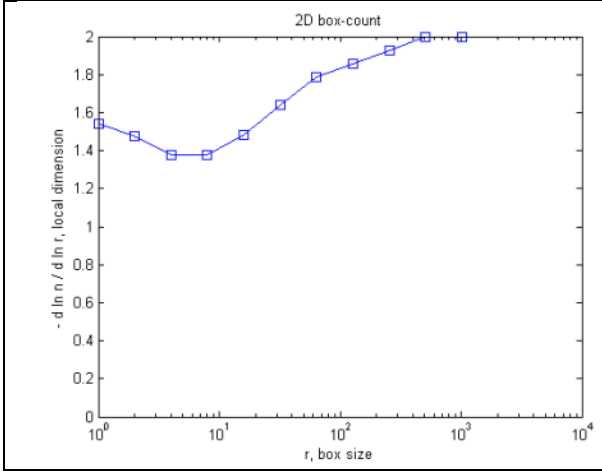	Showing the boxcounting results from observation domain 4. After integrating the slope curve, the average fractal dimension of this fracture network is: 1.6784.

Observation domain 5

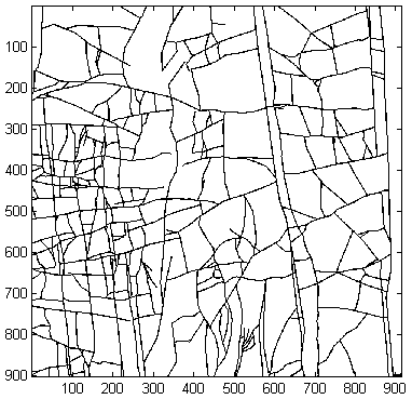

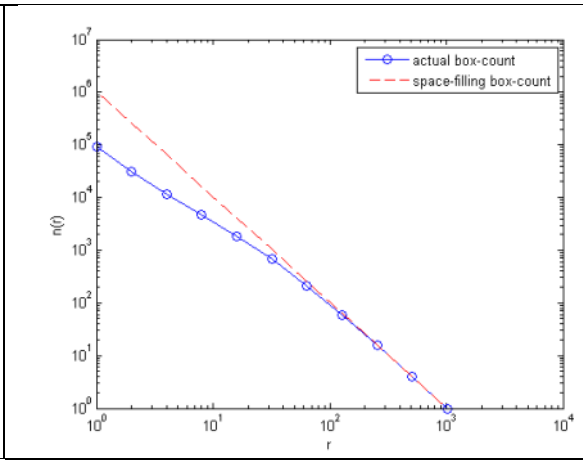

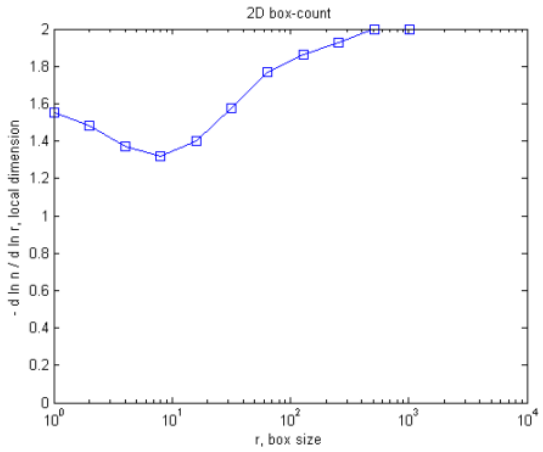

Showing the boxcounting results from observation domain 5. After integrating the slope curve, the average fractal dimension of this fracture network is: 1.6382.

Appendix 4: Cumulative Length Distribution Plots

Observation Domain 2

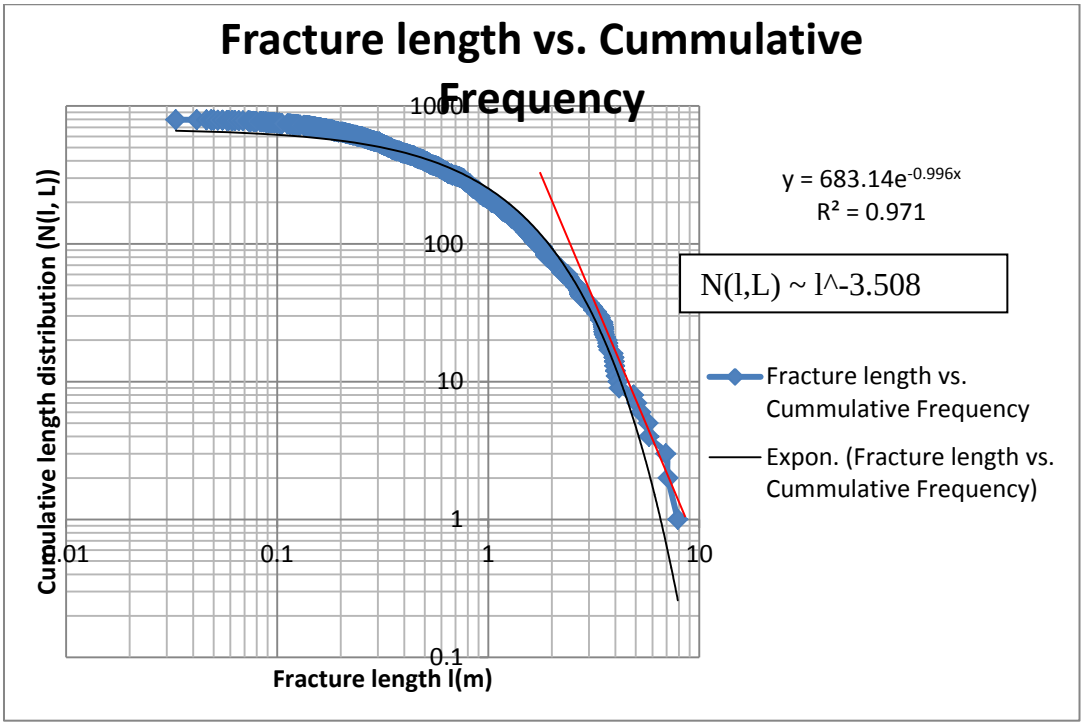

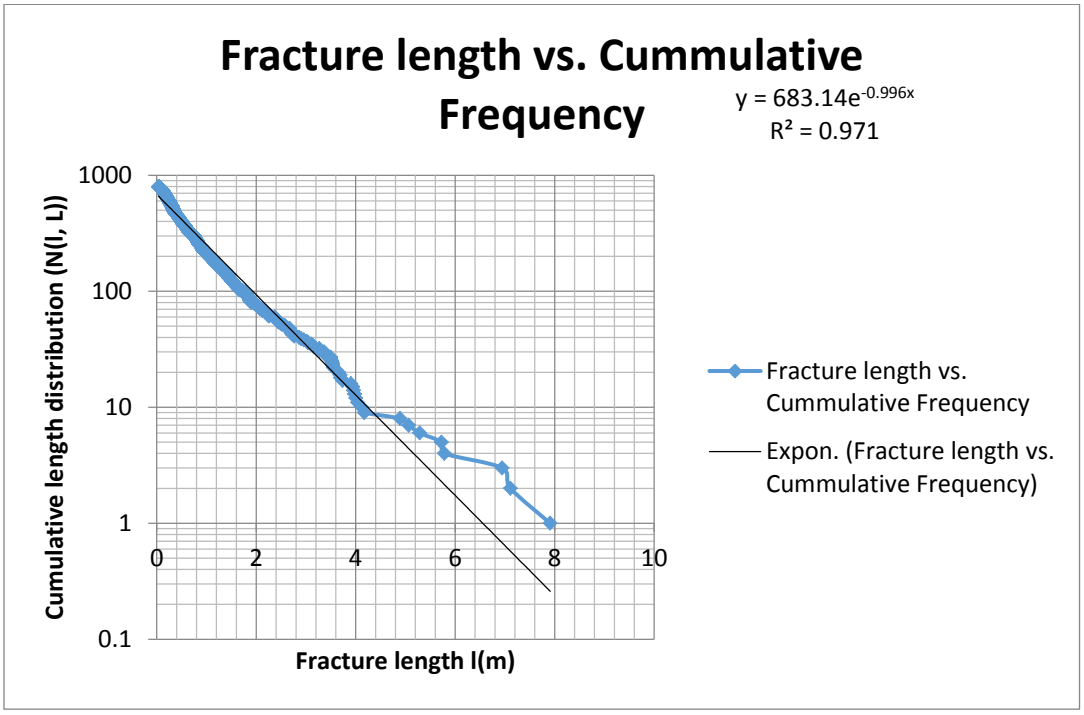

Appendix 4.1 a) Showing the cumulative length distribution of domain 2 on a log scale plot and two best fitting laws which try to simulate the observed data set. b) Showing the same data set but no the x-axis is now on a normal scale. These figures show that the fractures of grid 2 behave both in an exponential way and in a power law in terms of its cumulative length distribution.

Observation Area 3

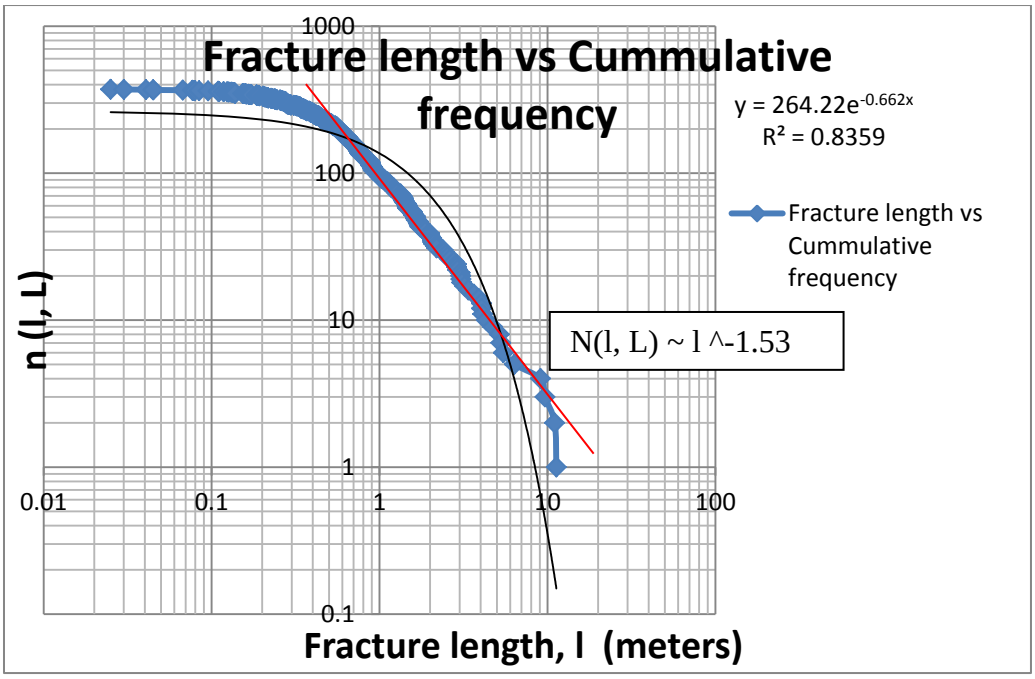

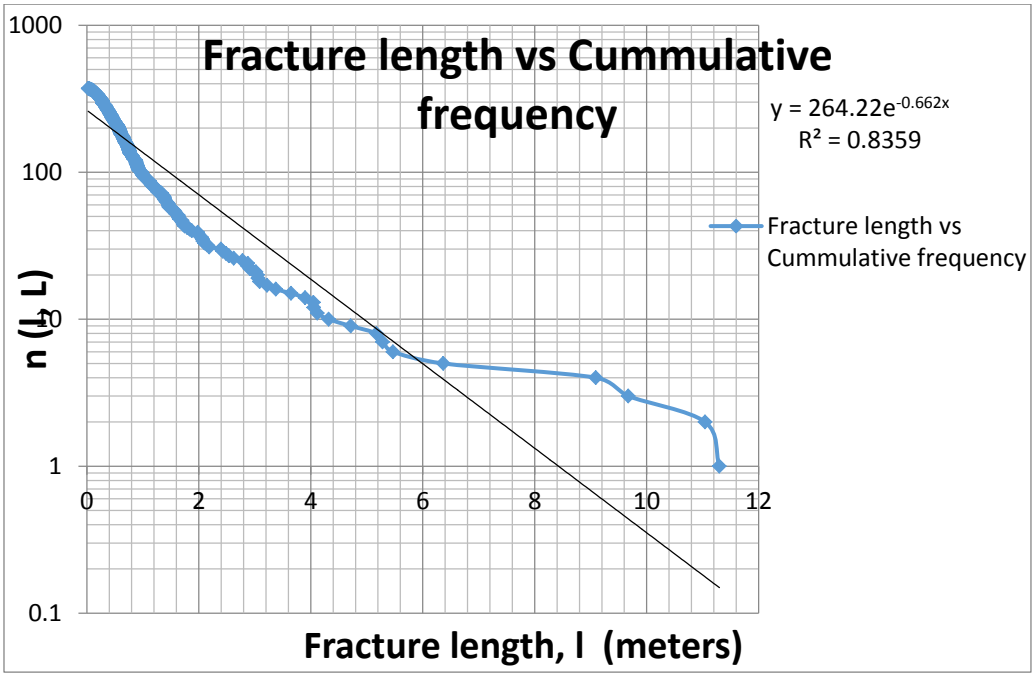

Appendix 4.2 a) Showing the cumulative length distribution of domain 3 on a log scale plot and two best fitting laws which try to simulate the observed data set. b) Showing the same data set but no the x-axis is now on a normal scale. These figures show that the fractures of domain 3 behave according to a power law and that only for fractures with l < 0.80m it starts to behave more like an exponential function

Observation domain 4

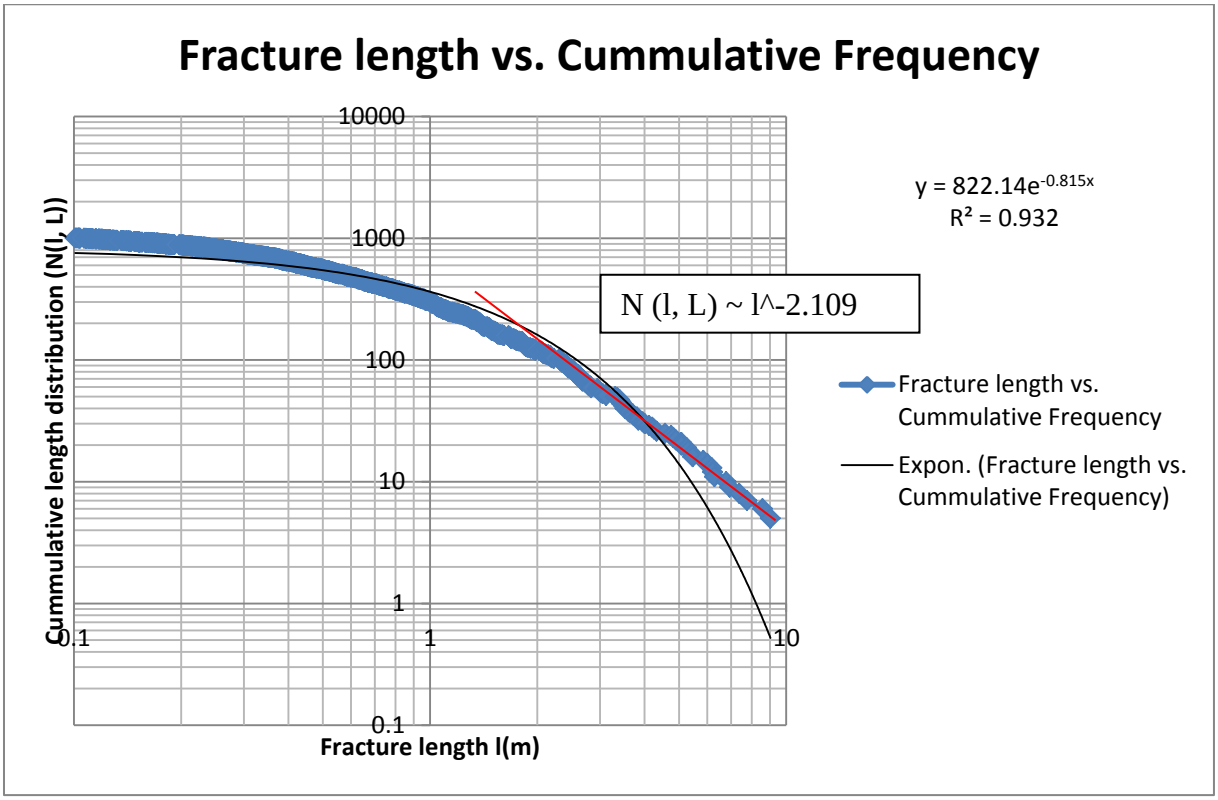

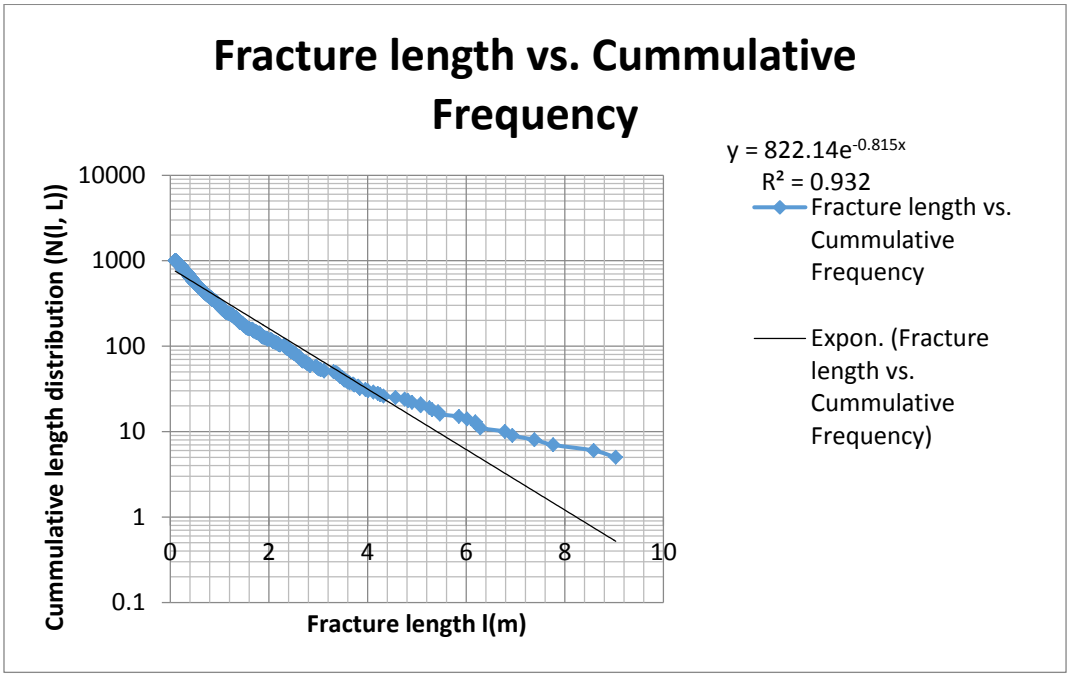

Appendix 4.3 a) Showing the cumulative length distribution of domain 4 on a log scale plot and two best fitting laws which try to simulate the observed data set. b) Showing the same data set but no the x-axis is now on a normal scale. These figures show that the fractures of

domain 4 behave according to a power law and that only for fractures with l < 2.0m it starts to behave more like an exponential function.

Appendix 5: The produced orthophotos and the workflow for fracture interpretation

Domain 1

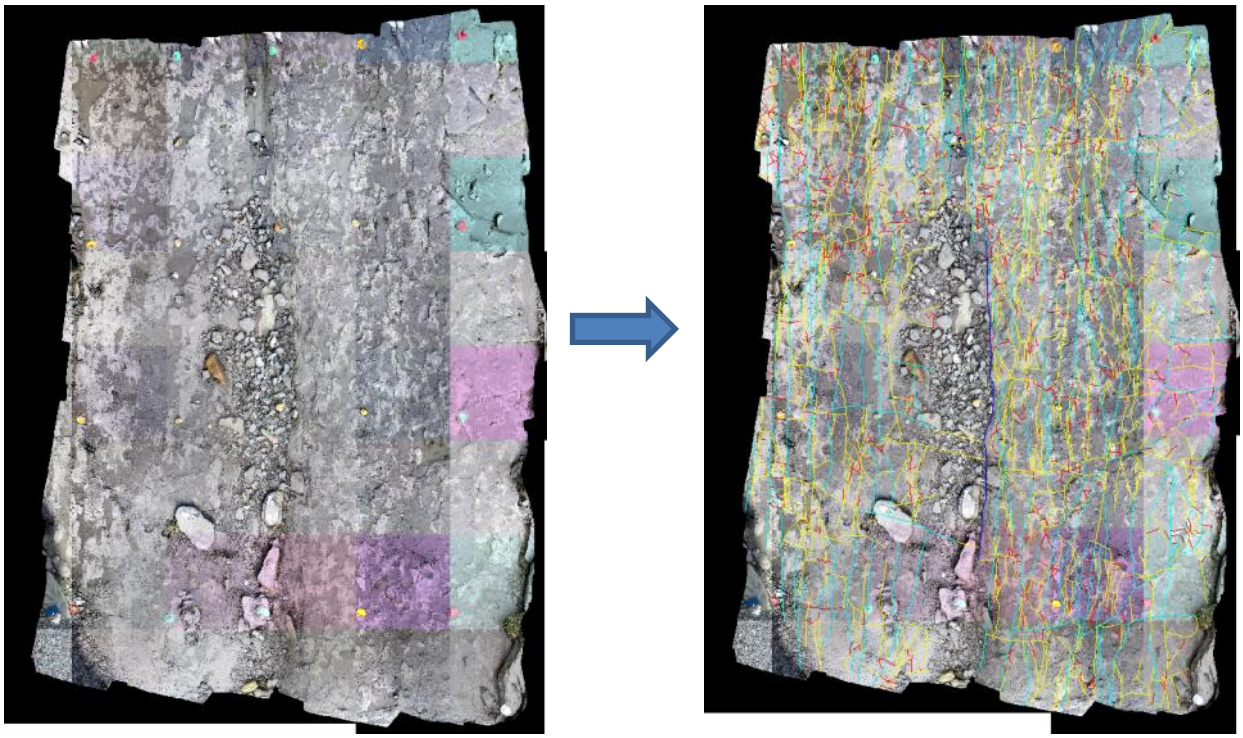

Domain 2

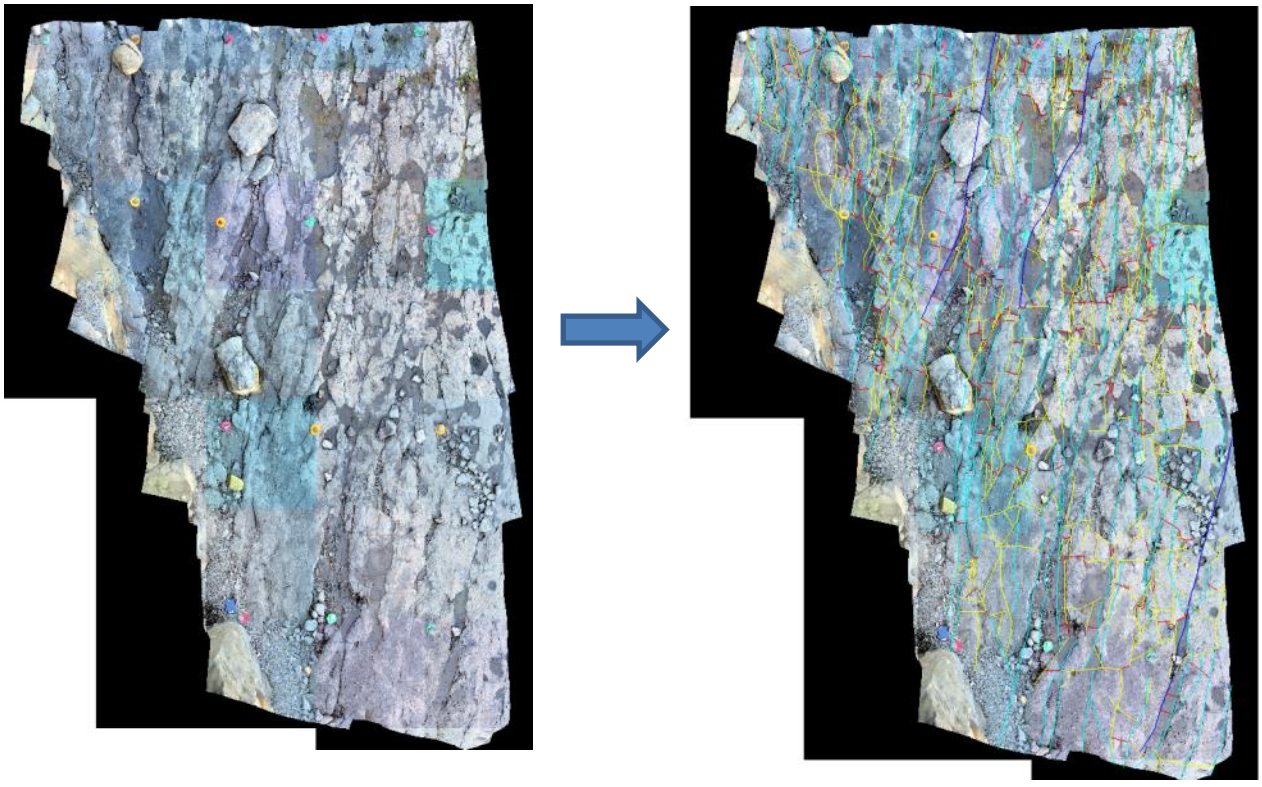

Domain 3

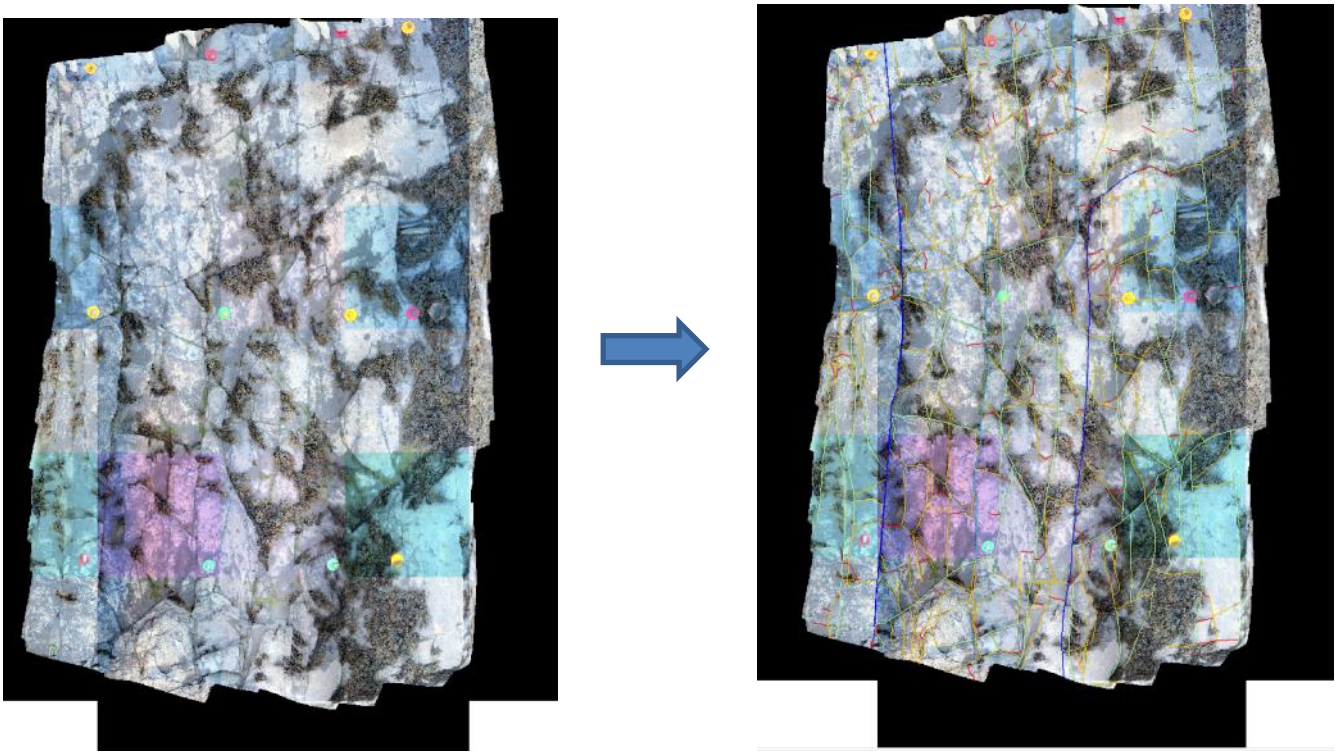

Domain 4

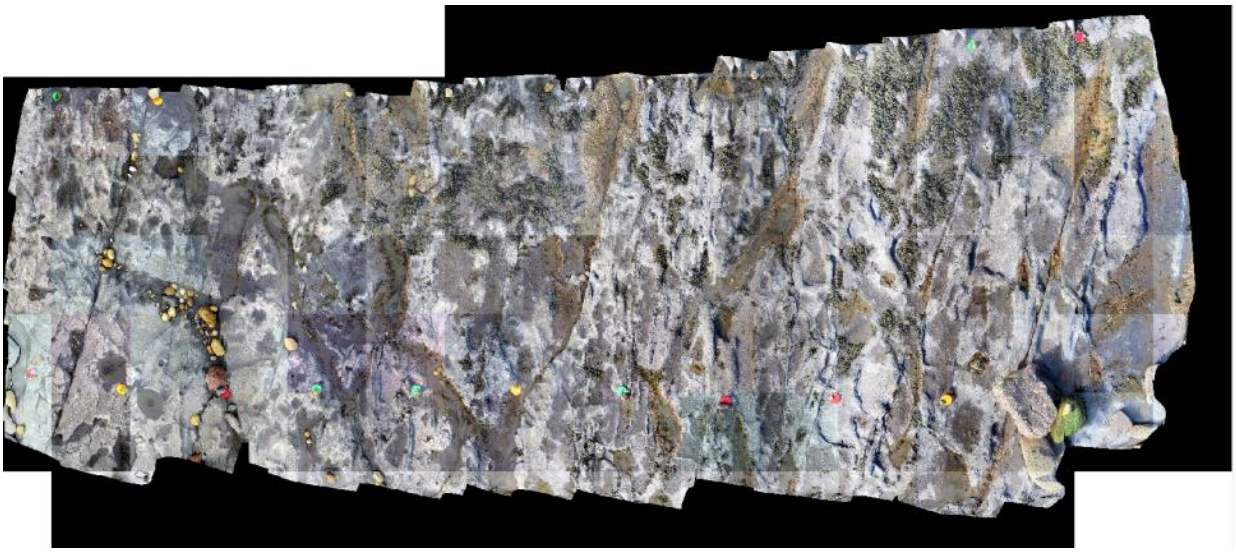

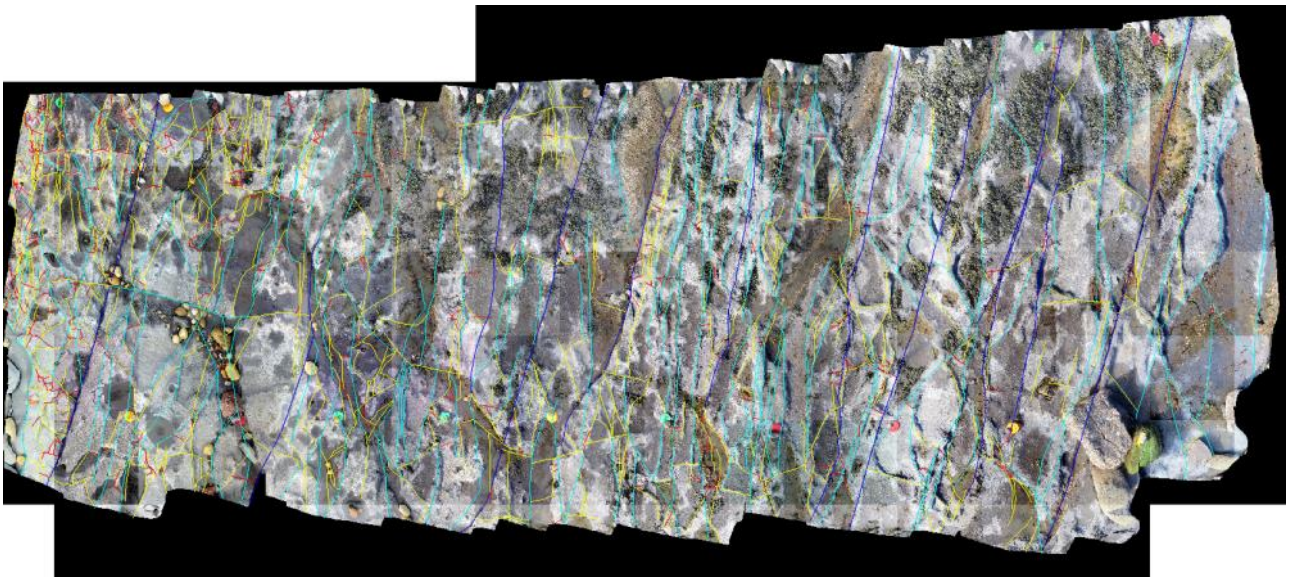

Domain 5

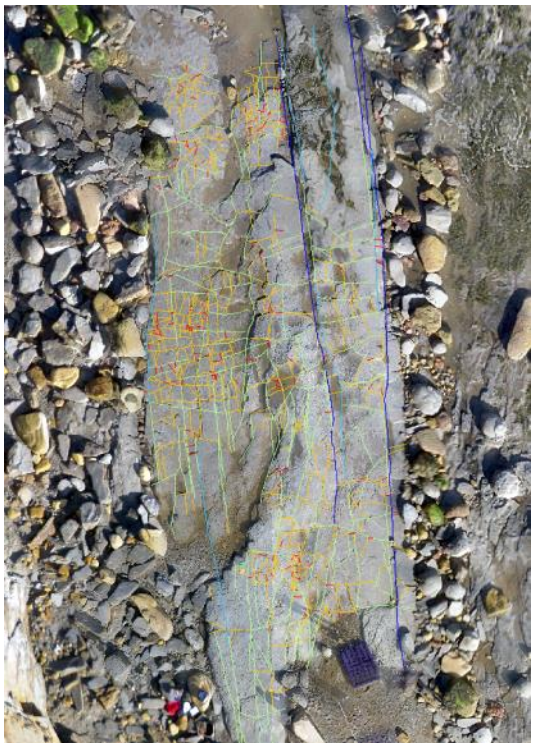

Notes